Università degli Studi di Napoli "FedericoII"

Dottorato di Ricerca in
Fisica Fondamentale ed Applicata

- 20° ciclo -

Atmospheric Aerosol Determination using Vertical Laser Tracks in the Pierre Auger Experiment

Laura Valore

Coordinatore:
Prof.Gennaro Miele

Anno Accademico 2006-2007

Contents

Introduction

Since their first discovery in 1912 by V. Hesse, the interest of the scientific community about cosmic rays and the consequent sistematic study of their properties led to many discoveries in astroparticle and subnuclear physics. Many experiments were built to detect and study their characteristics, and particles like the positron, the muon and the pion were discovered.

The cosmic rays spectrum spans over 11 decades in energy, ranging from 10^9 eV up to 10^{20} eV. Cosmic rays of energy above 10^{18} eV are usually referred as **Ultra High Energy Cosmic Rays** (UHECR), and constitute the more interesting and controversial part of the spectrum: one century after their discovery, physicists are still trying to give an answer to questions about the spectrum features, origin, acceleration mechanisms and mass composition of these particles. Moreover, in case of extragalactic primaries, a cutoff is expected in the spectrum in the energy region above 10^{19} eV, due to the interaction of particles with the *cosmic microwave background radiation* (CMBR); the cutoff is known as the GZK-limit. Its direct consequence is the impossibility for primary particles of such high energies to travel through distances above 100 Mpc. At these energies, light particles as protons are not expected to suffer significant deflections from galactic or extragalactic magnetic fields, hence the study of their arrival directions could lead directly to their sources.

The cosmic rays flux follows a $E^{-\gamma}$ power law, falling at a rate of about 3 orders of magnitude per energy decade; it rapidly decreases from 1 particle per m^2 per second at energies about 10^{11} eV, down to 1 particle per km^2 per century at energies above 10^{20} eV. Each energy region needs specific detection techniques, depending on the observed flux: "direct" techniques up to 10^{14} eV, based on the detection of the CR primaries before their interaction in atmosphere, using balloons or satellites; "indirect" techniques, based on the detection of the particle cascades (*Extesive Air Showers*) originating from the interaction of primary particles with the atmosphere. At

very high energies indirect techniques are mandatory, because the flux is so low that huge devices should be realized and launched in orbit to retrieve a statistically significant amount of data.

The Pierre Auger Experiment is a turn-over point in the study of UHECR: the hybrid nature of the observatory and the huge area covered by detectors is unprecedented. The use of two independent and complementary techniques (observation of the development in air of the shower, by the Fluorescence Detector (FD), and detection at ground of the secondary particles produced, by the Surface Detector (SD)) and the 3000 km^2 area covered by detectors allows to study UHECR with unprecedented precision and statistics. The Auger Experiment consists of two Observatories: one in the southern emisphere, near Malargüe, Argentina and the other in the northern emisphere, near Lamar, Colorado. The Auger South Observatory is almost complete: all the four fluorescence telescopes and $\sim 90\%$ of the surface array are fully operating (at september 30^{th} 2007). The completion of the apparate is planned for early 2008. The Auger North Observatory design is under study.

The amount of data collected by the Auger South Observatory is already greater than any other previous experiment on UHECR: a section of this thesis is dedicated to important recent results.

PhD Activity

The Auger group of Naples is involved in the analysis of FD events (showers and laser shots), in the atmospheric monitoring, in the study of the mass composition and in the study of neutrino induced showers.

My research activity is mainly focused on the measurement of the atmospheric transparency, needed for an accurate estimate of the energy of showers recorded by the Fluorescence Detector. The atmospheric conditions at the Pierre Auger Observatory are continuously monitored by means of several instruments that will be described in details. This work is one of the primary task within the Atmospheric Monitoring working group of the Auger Collaboration. The group is in charge to monitor atmospheric conditions (pressure, temperature, aerosol attenuation and characteristics, cloud coverage, etc.), to develop models to describe their variations, to implement algorithms to take into account the effect of such changes in simulation/reconstruction, and to fill and maintain databases accessed by these models during data analysis.

My work is aimed at measuring light attenuation as a function of time due

to aerosol, which is highly variable. For this purpose, I developed a procedure based on the analysis of vertical laser tracks produced every 15 minutes by the Central Laser Facility, a test beam located at ∼30 km from FD telescopes, which fires vertical laser shots during FD acquisition. As a pulse of laser light travels through the atmosphere, the molecular and aerosol components in the atmosphere scatter light out of the beam; the atmosphere scatters nearly equal amounts of light towards each FD building; this scattered light produces tracks recorded by the FDs. CLF laser light is attenuated in its travel towards FDs exactly in the same way the fluorescence light emitted by a shower; hence, the analysis of the amount of CLF light that reaches FD buildings can be used to infer the aerosol attenuation.

The procedure basically identifies the aerosol attenuation by means of the comparison of the CLF light collected by the FD with a set of simulations in different parametrized atmospheric conditions: for this reason, the procedure is named *"Laser Simulation Method"*.

The results produced by the analysis of 3.7 years of data are presented. A difference in the average aerosol concentration over separated periods (i.e. "CLF epochs") is observed. This difference can hardly be explained as due to seasonal variations and is most probably a hint of some systematics. My results have been compared to those obtained by another analysis based on CLF data, developed by Utah group of the Auger experiment. The correlation between results is good, but a systematic shift is observed between the same epochs just mentioned, again suggesting the presence of hidden systematics. The understanding of the origin of the discrepancy required a careful work that lasted over one year. In this phase, the algorithm for the energy reconstruction of laser events was developed. The study of CLF laser energy as a function of time put in evidence a discrepancy in the reconstructed energy with respect to the nominal value. The same discrepancy is observed analyzing an independent portable laser device (*Roving Laser*). This led to a recalibration of the whole Fluorescence Detector. Some trend with time was recovered, while a general deficit still remains.

The conclusion is that the aerosol concentration estimated with the Laser Simulation method is at the moment affected by systematics that must be still understood. To measure the aerosol concentration with this procedure, a normalization is needed for each epoch. I normalized data by means of a reference extremely clear night in which the aerosol concentration can be set to zero (i.e. *"Rayleigh night"*): the ratio between reconstructed and nominal energy returns the normalization constant needed to fix the energy scale. The correction is applied to real profiles, and then the analysis is performed on january 2004 - september 2007 data from 2 out of 4 telescopes (Los Leones and Coihueco).

Final results are in excellent agreement with those obtained with the independent Utah group algorithm, and a good correlation in observed also with data obtained by the LIDAR group. Seasonal variations of the aerosol concentration over almost 4 years of data are observed; this is the most striking proof of the reliabilty of the results. This observation suggests that a monthly parametrization of average aerosol attenuation can be produced. Such parametrization can be useful for periods when no attenuation measurement are available.

The aerosol database of the Auger Experiment is presently filled with the results obtained by Utah group. Since february 2007 my analysis provides the only available results: the aerosol database will be soon integrated with these values; moreover, the leaks in the database due to failures in the Utah analysis, will be completed with our results.

This thesis is organized as follows:

Chapter 1: General description of the properties of cosmic rays;

Chapter 2: Description of the Pierre Auger Experiment;

Chapter 3: Atmospheric tranparency and devices for the atmospheric monitoring in the Auger Experiment;

Chapter 4: Description of the Laser Simulation method;

Chapter 5: Determination of the aerosol concentration at the Pierre Auger Observatory and comparison with other independent analyses.

Chapter 1

The Physics of Cosmic Rays

1.1 History of cosmic rays

Cosmic rays history begins with their discovery in 1912 by the austrian physicist Victor Hess, and since then have been an inexhaustible source of discoveries in astroparticle and subnuclear physics. Particles as the pion, the muon and the positron have been discovered in consequence of cosmic rays studies.

At the beginning of the XX° century, physicists were concentrated on radioactivity studies, and the instruments for radioactovity detection, the electroscopes, were based on radioactivity property to ionize air molecules. When an electrosope is electrically charged, its golden leaves repel each other and stand apart. Radiation can ionize some of the air in the electroscope and allow the charge to leak away, causing the leaves to come back together.

Physicists noticed that the electric charge on golden leaves slowly leaks away, even when no obvious nearby source of X-rays or radioactivity were nearby, as if a radiation were always present. People began to think to a radiation emitted by the Earth; in 1910 Teodor Wulf took his electroscope on the edge of the Eiffel Tower to measure the radiation, and observed a decrease of the radiation with respect to the sea level, but not as much as he expected. Victor Hess [1] was the first to produce decisive results from balloon flights in which he ascended along with his electroscopes. Hess noted that the intensity of the ionizing radiation first decreased as the balloon went up, but above 1000 m the radiation started to increas, becoming from 3 to 5 times greater at heights above 5000 m. Hess concluded that the radiation observed was of extraterrestrial origin, and that its intensity decreased with the interaction in atmosphere, finally reaching the sea level.

One of the major skepticals about Hess' conclusion was Robert Millikan,

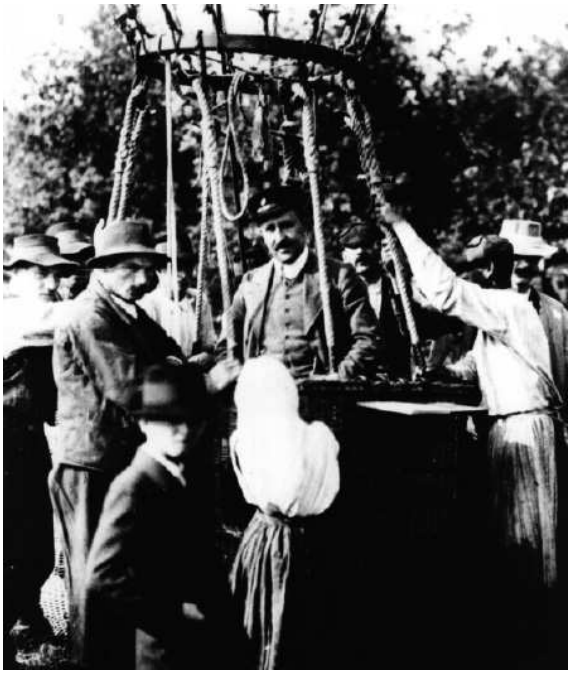

Figure 1.1: Victor Hess in one of his balloon flights.

whose experiments confirmed instead the extraterrestrial origin of the radiation: he finally came to agree to the not terrestrial origin of the radiation, he hypotized cosmic rays to be constituted by high energy γ rays and introduced the name *Cosmic Rays*.

In 1928, Geiger built the counter that brings his name: the instrument reveals the passage of charged particles, because of the ionization of the inner gas and the consequent production of a cascade of electrons activating an acoustic signal. Bothe and Kolhoster vertically disposed two Geiger counters connected to electroscopes. They discovered a great number of coincidences, that could be explained either by two electrons produced by a single cosmic ray, simultaneously passing through both counters, or by a single charged particle transpassing both counters. To test the second hypotesis, they disposed a golden block 4 cm high between the counters, discovering that 75% of the rays traversed also the block. So, the charged particles activating the counters were as penetrating as the radiation itself. They concluded that cosmic rays were high energy charged particles, and not γ rays as previously hypotized.

Bruno Rossi had a great intuition: he disposed Geiger counters not vertically, but on the same plane to form a triangle, so that one single ray could not transpass all 3 detectors. He developed also a coincidence circuit to select only the events simultaneously hitting the 3 counters. The great number of coincidences showed for the first time the existence of a shower of secondary particles.

In 1938 Pierre Auger [2], following Rossi studies, demonstrated that cosmic rays, entering the atmosphere and interacting with air molecules, produce a shower of secondary particles that reaches the sea level: he introduced the name *"Atmospheric Exstensive Air Shower"*, or EAS.

The reasearch activity on cosmic rays in years 30s and 40s led to the discovery of many new particles, whose existence had been so far only predicted by theory: it is the case of the positron and of the pion. Others, like the muon or strange particles like the kaon, hyperon, etc. where neither predicted. It is then evident the influence that cosmic ray discovery had on the particle physics development.

1.2 The Energy Spectrum

The cosmic rays spectrum covers a wide range, extending on 11 orders of magnitude, from 10^9 eV to 10^{20} eV. The cosmic rays flux follows a $E^{-\gamma}$ power law:

$$\frac{dN}{dE} \sim E^{-\gamma} \tag{1.1}$$

falling at a rate of about 3 orders of magnitude per energy decade, as shown in figure 1.2. It rapidly decreases from 1 particle per m^2 per second at energies about 10^{11} eV, to 1 particle per km^2 per year at energies of 10^{18} eV, down to 1 particle per km^2 per century at energies above 10^{20} eV.

At low energies, the spectral index γ is $\sim$ 2.6 - 2.7. Around 3×10^{15} eV a first steepening is observed, the so-called *knee*, where $\gamma \sim 3$; then a second steepening shows up at $\sim 5\times10^{17}$ eV, named *second knee*, where the spectral index $\gamma \sim 3.3$, as reported in [3]. At energies between 10^{18} and 10^{19} eV, the so called *ankle* appears with a flattening of the spectrum, with a spectral index $\gamma \sim 2.7$ [4].

In the conventional theory of cosmic rays, the bulk of the CR up to the *knee* is believed to originate within the Milky Way Galaxy by shock

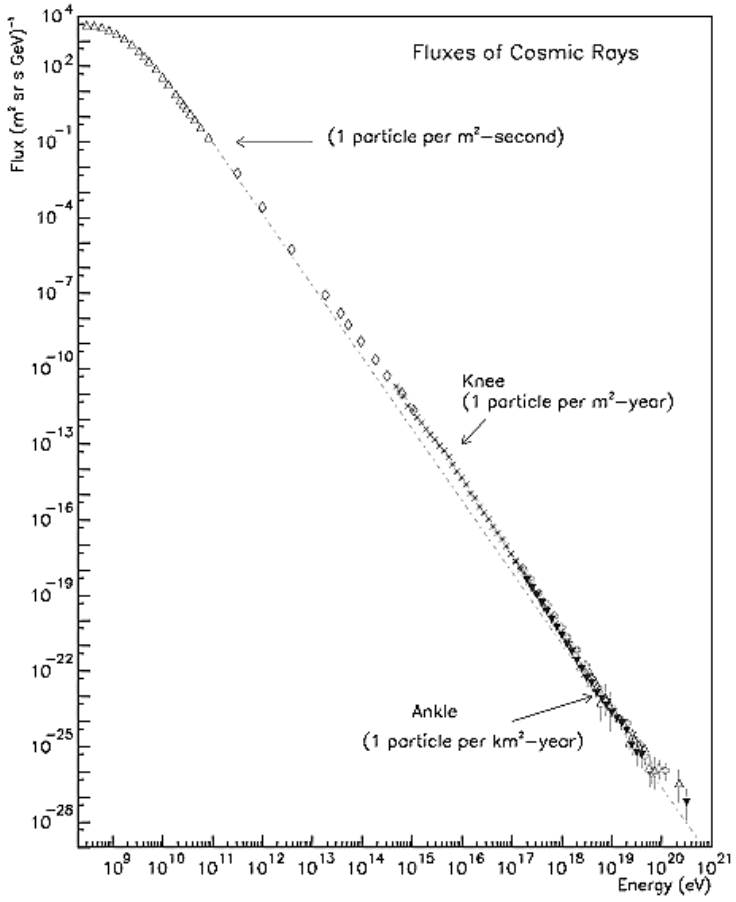

Figure 1.2: Cosmic rays energy spectrum. Some values of the integral flux are shown. The dashed line represents E^{-3} power law.

acceleration in supernovae remnants (SNR). There are some experimental evidences that the CR composition changes from a light one (mostly protons) around the *knee* towards one mainly composed by iron and even heavier nuclei at $E \simeq 4 \times 10^{17} eV$, the *second knee* [5], in association with the further spectrum steepening. This is expected in a scenario where primary particle acceleration and propagation is due to magnetic fields, whose effects depend on the magnetic rigidity $R = Z/A$, the ratio of charge to rest mass, as long as energy losses and interaction effects are small.

The flatter spectrum above the *ankle* is often interpreted as due to a new population of CRs with extragalactic origin that begins to dominate the more steeply falling Galactic population, no more confined by Galactic magnetic field at those energies, generating this feature just above the

galactic/extragalactic intersection energy.

An alternative scenario has been proposed by Berezinksy [10]:

1. the extragalactic component is completely proton dominated;
2. the transition from the galactic to the extragalactic component occurrs at lower energies (around the second knee);
3. the ankle is explained as a signature of the so-called (e^+e^-) pair production dip originating from the interaction of the extragalactic protons with the cosmic microwave background radiation (see next section).

Above the ankle, in the highest energy region, the possibility for the end of the spectrum is one of the most challenging point of study of cosmic rays.

1.3 The GZK Limit

In 1965 Penzias and Wilson discovered the existence of the Cosmic Microwave Background Radiation (*CMBR*) [7], Big Bang remnants constituted by photons at 2.7° K permeating the whole Universe. The following year (1966) Greisen [8] and independently Zatsepin e Kuz'min [9] showed that the interaction of cosmic ray primaries with CMBR photons would have led to a *cutoff* in the cosmic ray spectrum at the highest energies. The cutoff in the spectrum became known as the *GZK-limit*, from the names of the three physicists. The interaction of primary protons and heavier nuclei with the CMB radiation determines a rapid degradation of their energy, originating the cut in the spectrum.

The main reactions occurring between protons p and CMBR photons $\gamma_{2.7K}$ are photopion production and e^+e^- pair production:

$$p + \gamma_{2.7K} \rightarrow \begin{cases} \pi^0 + p \\ \pi^+ + n \\ p + e^+ + e^- \end{cases}$$

In the laboratory frame, the center of mass energy is:

$$s = \sqrt{m_p^2 + 2E_p E_{\gamma_{2.7K}}(1 - \beta cos\theta)} \tag{1.2}$$

Where β is the proton speed (c=1) and θ is the angle between proton and photon directions.

The threshold energy for a proton to produce a pion via photopion production on CMB photons in the laboratory rest frame is:

$$E_{thr} = \frac{m_\pi}{4E_{\gamma_{2.7K}}} \cdot (2m_p + m_\pi) \simeq 6.8 \times 10^{19} (\frac{E_{\gamma_{2.7K}}}{10^{-3}})^{-1} eV \tag{1.3}$$

in the photon rest frame. The cross section for this process strongly increases at the Δ resonance, which decays into pion channels $\pi^+ n$, $\pi^0 p$. With increasing energy, heavier baryon resonances occur and the proton might reappear only after successive decays of resonances.

The mean free path L for a proton can be estimated as:

$$L = (\sigma\rho)^{-1} \sim 8Mpc$$

with a CMB photon energy density $\sim 400\gamma/cm^3$ and cross section of the process at the threshold energy $\sigma_{p\gamma} \sim 10^{-28} cm^2$. The energy loss per interaction (inelasticity) is about 20%, thus the attenuation lenght of the process is about some tenths of Mpc; hence the sources of the highest energy cosmic rays should lie within a sphere of this size.

The e^+e^- production threshold energy in the laboratory rest frame is:

$$E_{th} = \frac{m_e(m_p + m_e)}{E_{\gamma_{2.7K}}} \sim 4.8 \times 10^{14} (\frac{E_{\gamma_{2.7K}}}{eV})^{-1} eV \sim 4.8 \times 10^{17} eV \tag{1.4}$$

Hence it starts at lower energies, but is much less significant than photopion production as its inelasticity is $\sim 0.1\%$. The mean free path is $\sim 1Mpc$, with a cross section of the order of $10^{-25} cm^2$.

The mean interaction lenghts of the two processes are plotted as dashed lines in fig. 1.3. Dividing by the average inelasticity of the collision $k(E)$, the energy-loss distances for the two processes is obtained (solid curves in fig.1.3):

$$\frac{E}{dE/dx} = \frac{x_{p\gamma}(E)}{k(E)} \tag{1.5}$$

Fig. 1.4 shows the proton energy degradation as a function of the mean flight distance. Independently of the initial energy of the proton, the mean energy values approach 10^{20} eV after a distance of ~ 100 Mpc.

$$\frac{E}{dE/dx} = \frac{x_{p\gamma}(E)}{k(E)} \tag{1.6}$$

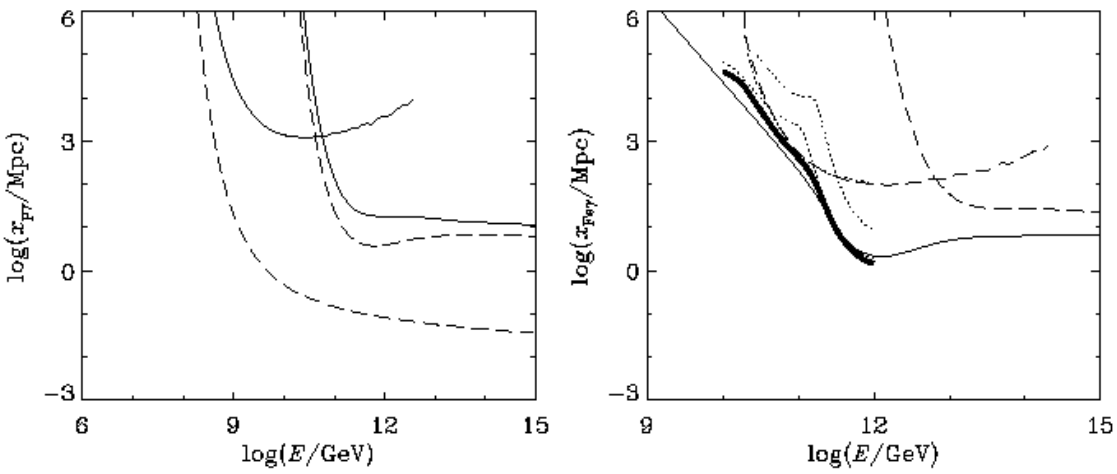

Figure 1.3: (a) Mean interaction length (dashed lines) and energy-loss distance (solid lines), $E/(dE/dx)$, for pair production and pion photoproduction in the cosmic microwave background radiation ($CMBR$) (lower and higher energy curves respectively) [11]. (b) Energy-loss distance of Fe-nuclei in the $CMBR$ for pair production (leftmost dashed line) and pion photoproduction (rightmost dashed line). Photodisintegration distances are given for loss of one nucleon (lower dotted curve), two nucleons (upper dotted curve) as well as the total loss distance (thick curve) estimated by Stecker and Salamon [12]. The thin full curve shows an estimate over a larger range of energy [13] of the total loss distance based on photodisintegration cross section of Karakula and Tkaczyk [14].

In the case of nuclei, relevant mechanisms for the energy loss are are pair production and photodisintegration, both on IR and on CMBR:

$$A + \gamma_{2.7K} \rightarrow \begin{cases} (A-1) + N \\ (A-2) + 2N \\ A + e^+ + e^- \end{cases}$$

Since the energy is shared between nucleons, the threshold energy for these processes increases; the inelasticity is lower by a factor 1/A, while the cross section increases with Z^2. Hence, the attenuation lenght will be smaller for heavier nuclei, but it will occurr at higher energies.

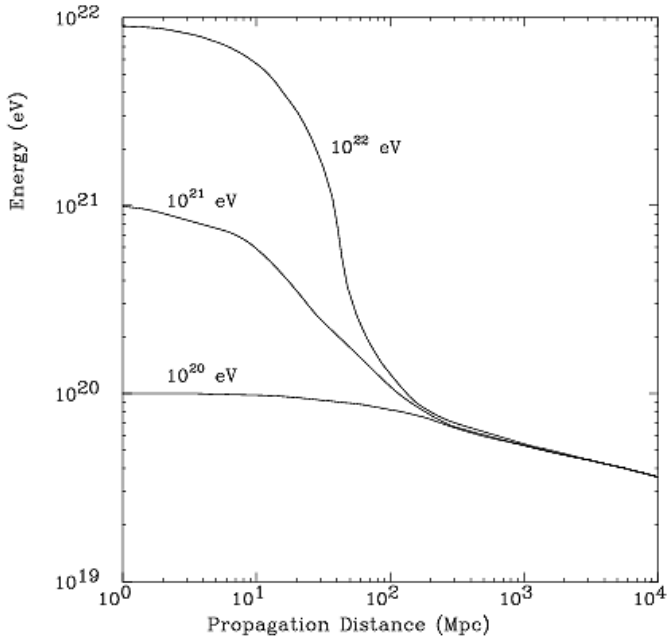

Figure 1.4:

Neutrons, even at the higher energies, decay into protons after a free fly of only $\sim 1\ Mpc$, so they could be ruled out.

In the case of high energy $\gamma-$rays, the dominant absorption process is pair production through collisions with the radiation fields permeating the Universe. On the other hand, electrons and positrons could produce new $\gamma-$rays via inverse Compton scattering. The new γ can initiate a fresh cycle of pair production and inverse Compton scattering interactions, yielding an electromagnetic cascade. The development of electromagnetic cascades depends sensitively on the strength of the extragalactic magnetic field B, which is rather uncertain.

The threshold for the pair production process is of the order of m_e^2/ϵ, where ϵ is the energy of the radiation field involved. Above $10^{20}\ eV$, the most relevant interactions are those with radio background, which is almost unknown. Therefore, the GZK radius of the photon strongly depends on the strength of extragalactic magnetic fields. In principle, distant sources with a redshift $z > 0.03$ can contribute to the observed cosmic rays above $5 \times 10^{19} eV$ if the extragalactic magnetic field does not exceed $10^{-12}\ G$ [16].

Neutrinos do not suffer any energy degradation during their travel through the Universe, unless for energies above 10^{23} eV [17]. As noted by Weiler [18, 19], neutrinos can travel over cosmological distances with negligible energy loss and could produce Z bosons on resonance through annihilation on the relic neutrino background, within a GZK distance from Earth. In that case, highly boosted decay products could be observed as super$-GZK$ (above $GZK-$limit) primaries and they would point directly back to the source. This model of course requires very luminous sources of extremely high energy neutrinos through-out the Universe.

Finally, the GZK theory predicts, in case of a uniform sources distribution, that around 4×10^{19} eV about 50% of the particles should come from a maximum distance of ~ 100 Mpc, while at E $= 10^{20}$ eV the distance should reduce to 20 Mpc. Since 1960, a few events of energy above this limit have been detected.

Since the direct consequence of the GZK limit is the impossibility for primaries of such energies to travel through distances above ~ 100 Mpc, and since at these energies primaries should not significantly suffer deflections due to galactic/extragalactic magnetic fields, these should point directly to their sources, allowing their individuation; Section 1.9.4 is dedicated to recent anisotropy results from the Auger Experiment.

1.4 Sources and Acceleration mechanisms

In the lower part of the energy spectrum, charged particles, the main component of the CR radiation, interact with the galactic magnetic field during their propagation, loosing directionality informations and making difficult the individuation of sources. However, at the highest energies CR should not suffer significant deflections from magnetic fields, hence particles should propagate in balistic-like way pointing directly at their sources.

Several arguments involving energy, composition and secondary $\gamma-$ray production suggest that the bulk of CR (between 10^9 up to 10^{15} eV) is confined to the galaxy and is probably accelerated in supernova remnants ($SNRs$). The acceleration is assumed to take place at the shock front associated to the supersonic motions of the expanding shell and the particles are energized through acceleration a la Fermi [20].

Beyond these energies, between the knee and the ankle the situation becomes less clear: a model was recently proposed in [21], in which particles self-generate an amplified magnetic field in the vicinity of the source. More-

over, at some energy around $10^{18}\ eV$, all observed CR are expected to be of extragalactic origin, because they cannot be confined in the Galaxy long enough to be accelerated to such energies.

These hypothesis are based on the value of the Larmor radius of a particle, with charge Ze, traveling in a medium with an estimated value of the magnetic field B

$$r_L \sim 110 \frac{E_{20}}{ZB_{\mu G}} kpc \tag{1.7}$$

where $B_{\mu G}$ is the magnetic field in units of μG and $E_{20} = 10^{20}\ eV$. Then, increasing with the energy, a proton has an higher probability to escape from the galaxy region.

The maximum energy attainable in diffusive shock acceleration depends on the size and on the magnetic field strenght of the object where the acceleration takes place. Large sizes and strong fields are required to accelerate particles up to $10^{20}\ eV$, since particles with a Larmor radius exceeding the size of the astrophysical objects are able to escape from the acceleration region. This condition is summarized in the following expression [22]:

$$E_{max} \approx 2\beta c Z e B r_L \tag{1.8}$$

for the maximum energy acquired by a particle traveling in a medium with magnetic field B, where βc is the characteristic velocity of magnetic scattering centers. This is known as "Hillas criterion". The "Hillas criterion" allows to classify different sources, as summarized in the form of the popular "Hillas diagram" shown in fig. 1.5.

Figure 1.5 shows that few sites are able to generate particles with energy above $10^{20}\ eV$. The maximum energy is further limited by losses in the acceleration region, competing with the acceleration mechanism.

There are basically two kinds of acceleration mechanism for $UHECR$ (E $> 10^{18}$ eV):

1. bottom-up, in which cosmic rays are produced and accelerated in astrophysical environments;

2. top-down, in which exotic particles, from early universe, decay producing cosmic rays.

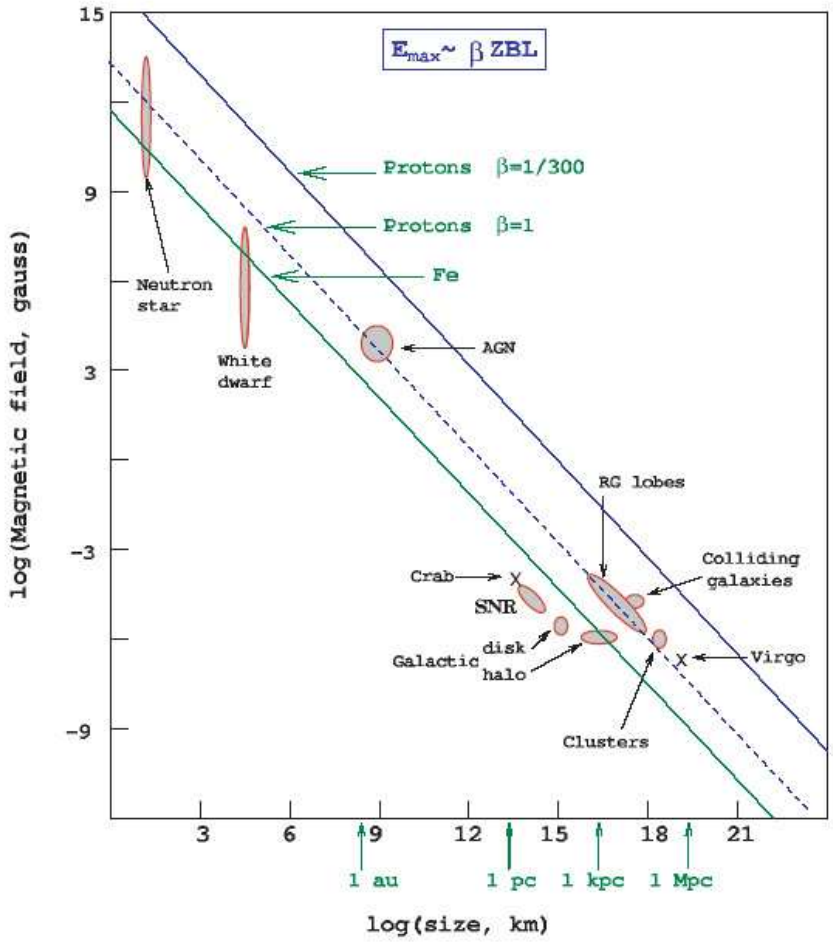

Figure 1.5: The Hillas diagram showing size and magnetic field strengths of possible astrophysical sites of particle acceleration. According to eq. 1.8, assuming the extreme value $\beta = 1$, objects below the diagonal lines (from top to bottom) cannot accelerate protons above 10^{21} eV, above 10^{20} eV and iron nuclei above 10^{20} eV.

Bottom-up

In the bottom-up models, mainly two mechanisms are suggested: direct acceleration by electric fields [22] or statistical acceleration (Fermi acceleration) by magnetized plasma.

In the direct acceleration mechanism, the electric field could be due to a rotating magnetic neutron star (pulsar) or an accretion disk threaded by magnetic fields, etc. The maximum achievable energy depends on the par-

ticular astrophysical environment. Direct acceleration mechanisms are not widely favored because it is usually not obvious how to obtain the characteristic observed power-law spectrum.

In statistical acceleration mechanisms, particles gain energy gradually by numerous encounters with moving magnetized plasma. These kinds of models were pioneered by Fermi [20] in 1949 and are able to produce the typical power-law spectrum. However, the acceleration is slow and it is hard to keep particles confined within the Fermi engine.

Top-down

Top-down scenarios avoid acceleration problem by assuming that charged and neutral primaries arise in the decay of supermassive elementary X particles. Sources of these exotic particles could be:

1. topological defects, from early Universe phase transitions associated with the spontaneous symmetry breaking [23, 24, 25, 26, 27, 28];

2. long-lived metastable super-heavy relic particles produced through vacuum fluctuation during the inflationary stage of the Universe [29, 30, 31, 32];

Topological defects (magnetic monopoles, cosmic strings, domain walls, etc.) are stable and can survive for ever with massive X particles ($\approx 10^{16} - 10^{19}\ GeV$) trapped inside them. Sometimes, they can be destroyed through collapse, annihilation etc., and their energy would be released in the form of massive quanta that typically decay into quarks and leptons. In a similar way, superheavy relics could decay in quarks and leptons. Then CR with energies up to m_X can be produced. These topological defects or superheavy particles would lay in the galactic halo ragion. Another exotic explanation of the $UHECR$ postulates that relic topological defectes themselves constitute the primaries [33, 34]. General features of these exotic scenarios are discussed in several reviews [35, 36, 37, 38, 39, 40].

1.5 The cosmic ray mass composition

Experiments built to study CR up to energies E = $10^{14}\ eV$, based on emulsion chambers, spectrometers an other devices connected to balloons or space stations, allowed the determination of the mass composition with high precision. Up to these energies, CR are mainly composed by 99.8% from charge particles, while the remaining 0.2% is composed by photons and neutrinos.

Charged particles are divided mostly in nuclei (98%) and in a fraction in positrons and electrons (2%). Moreover, the 87% of nuclei are protons, largely the principal constituents of the cosmic radiation at these energies, the 12% are helium nuclei and the remaining 1% are heavy nuclei.

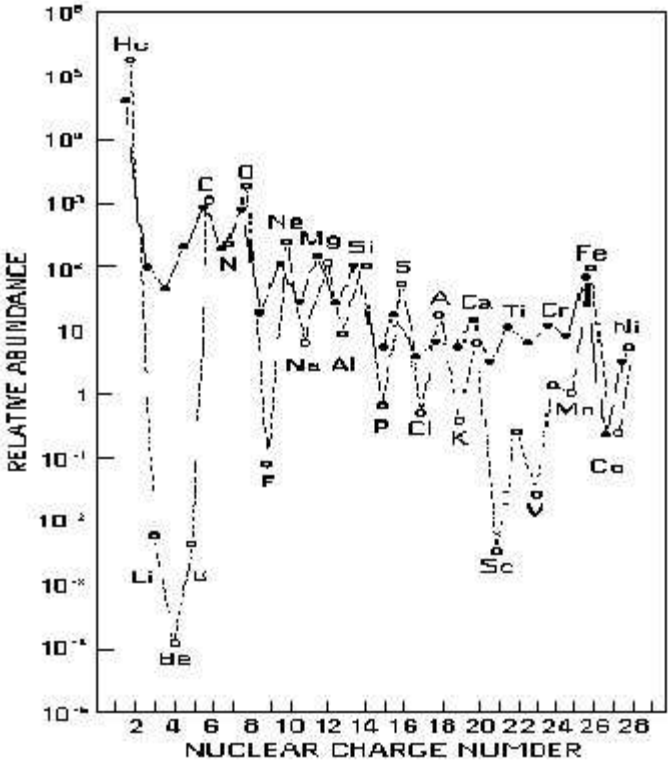

Figure 1.6: Comparison between Solar System (∘) and Cosmic Rays (•) mass composition.

Comparing the relative abundances of cosmic rays with those of Solar System elements, a similar trend with some exceptions is observable (see fig. 1.6): two groups of elements, Li, Be, B and Sc, Ti, V, Cr, Mn, are more abundant in the CR composition than in the Solar System. This discrepancy is easily explained, since these elements are not produced in stellar nucleosintesys and their presence in CR can be due to heavy nuclei fragmentation occurring in collisions with the interstellar medium during CR propagation: C and O fragmentation produces Li, Be and B, while Fe fragmentation produces Sc, Ti, V, Cr, Mn.

At energies around the knee, since it is not possible to perform a direct measurement of the cosmic radiation, the nature of primary particles is inferred from Extensive Air Shower studies. In this energy region a shift towards a heavier nuclei composition is observed. This effect is explicable with the escape from the galaxy of the lighter galactic component of cosmic rays. Actually, at energies above $E \sim 10^{15}\ eV$, the galactic magnetic field is no more able to confine light particles, due to the high value of their magnetic rigidity, that becomes even more heavy appraching the second knee. The magnetic rigidity is defined as $R = \frac{pc}{Ze}$, where p is the momentum of the particle, c is the speed of light and Ze is the particle charge in units of electronic charge. In correspondance of the second knee also particles with a higher atomic number get a magnetic rigidity sufficent to be no more confined in the Galaxy. At higher energies cosmic rays are expected to be protons of extragalactic origin, so a shift towards a lighter composition is predicted.

The mass composition of cosmic rays of $E > 10^{17}\ eV$ in fluorescence experiments is usually measured studying the depth of the maximum of the shower as a function of the energy. This method is usually known as the "Elongation Rate". In UHECR energy region, due to the lack of statistics and to the uncertainties related to the hadronic models used for data interpretation, the situation on mass composition in still not clear.

Results on mass composition from several experiments are reported in section 1.9.1.

1.6 Extensive Air Showers

The cosmic ray primaries interact with the atmosphere producing a shower of secondary particles named *Extensive Air Showers* (EAS). The atmosphere acts as a huge calorimeter, since the primary energy is related to the energy deposited in the atmosphere by the produced particles.

The number of particles produced in successive generations grows up reaching a maximum, then it begins to decrease, because the energy carried by secondary particles becomes lower that the energy needed to produce a new generation. During the propagation in atmosphere, particles gain a transverse momentum that determines a deflection angle $\theta = \frac{p_\perp}{p_\parallel}$ that grows as the energy descreases: this leads to an extension at sea level of the shower front ranging from thousands of m^2 at E = $10^{15}\ eV$, up to hundreds of km^2 at E > $10^{18}\ eV$.

Parameters describing the development of a shower in the atmosphere are the *size N(x)*, that is the number of particles as a function of the traversed atmospheric depth expressed in g/cm^2, and X_{max}, that is the atmospheric depth traversed by the shower up to the point of maximum development. These quantities are related to the primary nature and energy. The shower keeps the direction of the generating primary, developing itself around the *shower axis*. The impact point at ground is defined as the *core* of the shower.

If the cosmic ray primary is a nucleon or a nucleus, the shower begins with an hadronic interaction. The number of hadrons grows generation by generation; in each generation about 30% of the energy is trasferred to the electromagnetic cascade originating by the π^0 mesons decay. Moreover, the electromagnetic shower dissipates up to 90% of the energy by ionization. The remaining energy is kept by muons and neutrinos produced by charged pions decay (π^+, π^-). Figure 1.7 shows a schematic view of the developemnt of a shower.

While the energy of the electromagnetic component is proportional to the energy of the shower itself, the number of muons reaching the ground slowly grows for increasing energies. In a proton induced shower the number of muons reaching the ground is proportional to $E^{0.85}$; assuming that nuclei of atomic number A can be considered as a collection of nuclei each with energy $\frac{E}{A}$, a shower induced by an iron nucleus ($A = 56$) produces 80% more muons at ground than a proton induced shower. In principle, this allows to distinguish between proton and heavier nucleus induced showers.

The knowledge of the processes involved in hadronic showers development is limited to the highest feasible energy with particle accelerators. So far, the highest energy collisions are provided in the Tevatron collider: the energy reached in the center of mass frame is ~ 1.8 TeV, nearly the energy of the *knee*. The Large Hadron Collider (LHC) at CERN will collide protons with protons at E $\sim$ 14 TeV; however, this energy is still a factor 50 smaller than the center of mass energy of the highest energy cosmic ray so far observed, assuming A=1, and the kinematic region of interest is different. At the highest energies, hadronic interaction models are thus extrapolated on the basis of the known processes at lower energies.

Most of the general features of an electromagnetic cascade can be understood in terms of the toy model due to Heitler [41], in which the shower development is characterized only by bremsstrahlung and pair production processes, and in which each interaction process produces the conversion of one particle in two. These processes have the same interaction lenght X_0.

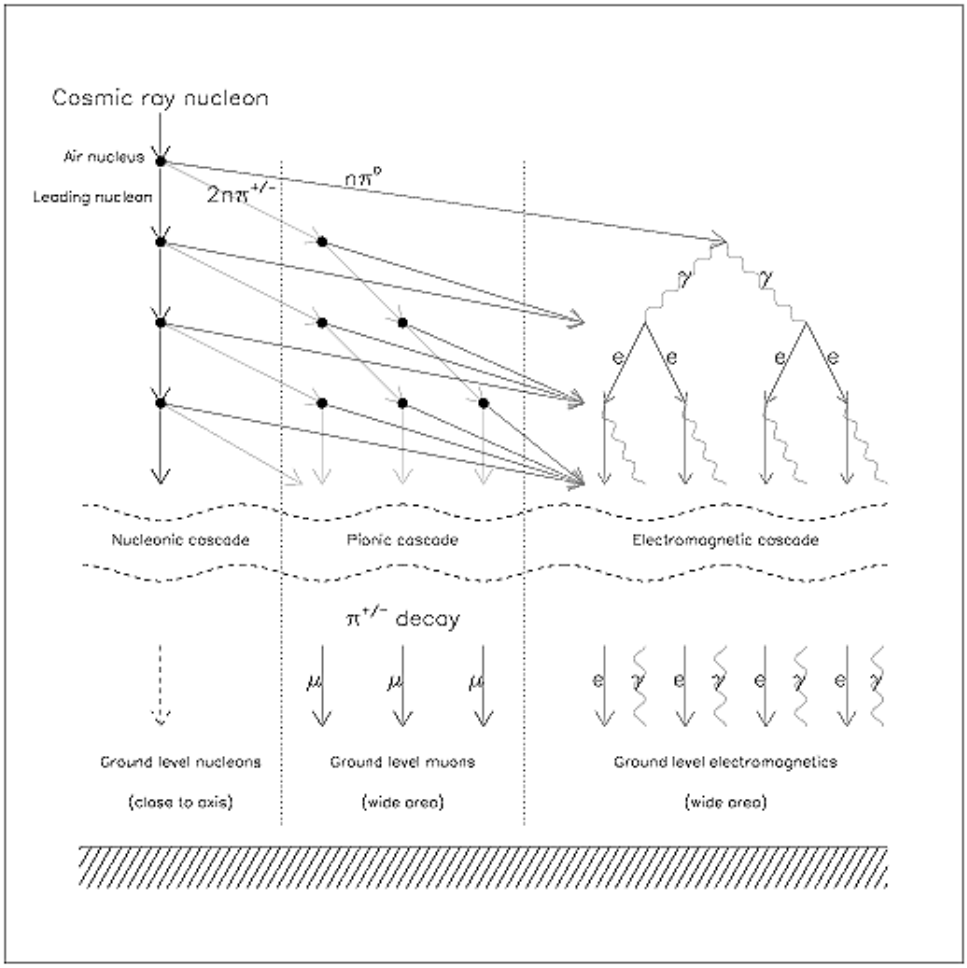

Figure 1.7: Schematic representation of the main processes occurring in the EAS deveopment. It is assumed that the incident cosmic primary is a nucleon. The resulting shower is divided in 3 categories: the nucleon itself (*leading particle*) continuing in the direction of entry in the atmosphere, the hadronic cascade (charged pions) and the electromagnetic cascade produced by neutral pions decay.

Hence, the model assumes:

1. in the bremsstrahlung process, final photon and electron (positron) share the energy of the initial electron (positron);

2. in the pair production process, e^+ and e^- share the energy of the initial photon;

3. multiple scattering is neglected and the shower development is unidimensional;

4. Compton scattering is neglected.

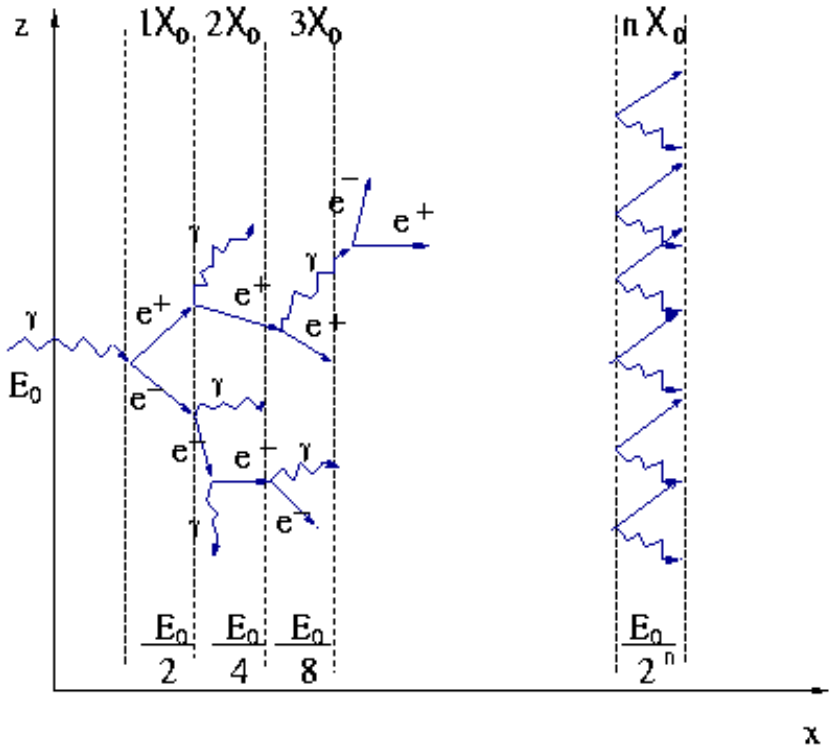

Figure 1.8: Electromagnetic Shower development scheme in the Heitler Model.

In the model, the shower is represented as a tree with branches splitting every X_0, until they fall below the critical energy E_C (see fig. 1.8). Above E_C, the number of particles grows geometrically, so after n ($n = X/X_0$) steps (branchings), the total number of particles as a function of the slant depth is

$$N(X) = 2^{X/X_0} \tag{1.9}$$

while the energy for each particle is

$$E(X) = \frac{E_0}{N(X)} \tag{1.10}$$

where E_0 is the energy of the particle that initiated the shower (the first photon). At the maximum, the number of particles should be

$$N(X_{max}) = \frac{E_0}{E_c} \tag{1.11}$$

then we get

$$X_{max} = \frac{X_0 \ln(E_0/E_C)}{\ln 2} \tag{1.12}$$

For proton showers, the Heitler model predicts that X_{max} scales logarithmically with the primary energy, while N_{max} scales linearly. In the case of heavy nuclei, using the superposition principle as a reasonable approximation, a shower produced by a nucleus of energy E_A and mass A, is modeled by a collection of A proton shower. Then its maximum is $X_{max} \propto \ln(E_0/A)$.

The Heitler model, though very simple, is very useful to get a first intuition about global shower properties.

1.7 Radiation emission in EAS development

During the development of a shower, besides the generation of secondary particles, radiation emission occurrs. This radiation is divided in Cherenkov light, due to electrons, Fluorescence light, due to the interaction of particles with air molecules and Radio emission, due to coherent syncrotron radiation emitted in the Earth magnetic field [59].

1.7.1 Fluorescence Light

During the development of an extensive air shower, most of its energy is dissipated by excitation and ionization of the air molecules along its path. Excited molecules dissipate the energy gained through not radiative collisions, through internal quenching processes[1] or through photon emission in the energy range 300 - 420 nm, defined as fluorescence light (see fig. 1.9).

To predict the amount of fluorescence light emitted along the shower path, it is necessary to find the energy loss rate by means of collisional processes going into fluorescence light. Since the particles mostly affected by energy losses due to collisional processes are those with lower ionization power as electromagnetic particles, and since these are the dominant component in

[1] it is a process in which molecules accomplish a downward electronic transition without emitting radiation.

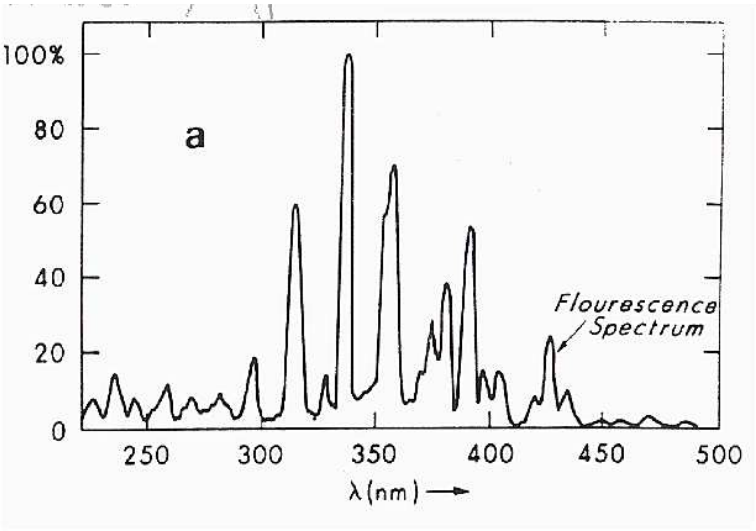

Figure 1.9: Spettro della fluorescenza atmosferica.

a cascade[2], it is possible to assume that the energy loss rate by collision is proportional to the shower size.

Fluorescence light from air results almost entirely from electronic transitions in the N_2 molecule and N_2^+ molecular ion. It has been experimentally observed that the light emission mainly comes out from N_2 second positive system ($2P$) and the N_2^+ first negative system ($1N$) [42, 43, 44], according to standard spectroscopic notation.

Excitation mechanism for these two system are different. The $1N$ system can be excited by direct collision with an high energy particle

$$N_2 + e \rightarrow N_2^{+*} + e + e \tag{1.13}$$

The $2P$ system cannot be directly excitated beacuse the necessary change in the resultant electronic spin of the molecule is forbidden. This band can be excited by collision with low energy particles involving electron exchange with a resultant spin change, or by decay from higher levels, in processes such as:

$$N_2 + e(\uparrow) \rightarrow N_2^*(^3\Pi_u) + e(\downarrow) \tag{1.14}$$

$$N_2^+ + e \rightarrow N_2^*(^3\Pi_u) \tag{1.15}$$

[2]typically the electron and positron population produced in a shower is higher by a factor 2 than other particles population

It should be noted that N_2 molecule has got 18 vibrational levels associated with $2P$ band, whereas $1N$ band has only one possible wavelenght.

The fluorescence efficency is [42],[60]:

$$\frac{n}{E_{dep}}\Big[\frac{\text{photons}}{MeV}\Big] = \epsilon_\lambda \cdot \frac{\lambda}{hc} \tag{1.16}$$

where h is the Plank constant, n is the number of emitted photons, ϵ_λ is the fluorescence efficency as a function of the wavelength and E_{dep} the total energy deposited in air. It is now possible to introduce the *fluorescence yield* N_γ as

$$N_\gamma = \epsilon_\lambda(p,T) \cdot \frac{\lambda}{hc} \cdot \frac{dE}{dx} \cdot \rho_{air}\Big[\frac{\text{photons}}{m}\Big] \tag{1.17}$$

where ρ_{air} is the atmospheric density, dE/dx the energy loss rate and $\epsilon_\lambda(p,T)$ is the fluorescence efficency, which is function of the air pressure and temperature.

The angular distribution of the fluorescence light can be approximated as an isotropic distribution

$$\frac{dn}{dld\Omega} = \frac{N_\gamma N_e}{4\pi} \tag{1.18}$$

where N_e is the number of electrons in the EAS generating the light.

The resultant fluorescence yield corresponds to a scintillation efficiency of only 0.5%. This poor efficiency is compensated for by the overwhelming amount of energy being dissipated by a 10^{20} eV ($\approx 1J$ in 30 μs).

1.7.2 Cherenkov light

Electrons in EAS generate a large amount of Cherenkov light, primarily beamed in the forward direction [47, 48, 49]. The amount of Cherenkov light at any point along the shower front depends upon the previous history of the shower. Thus this light is not proportional to local shower size. Directly-beamed Cherenkov light dominates the fluorescence light at emission angles relative to the EAS axis θ of less then 25° [50]. Moreover, as the Cherenkov component builds up with the propagating shower front, the resultant intense beam can generate enough scattered light at low altitudes such that it competes with the locally produced fluorescence light from the "dying" shower.

An exact calculation of the Cherenkov light signal is not easy, and must be carried out numerically. The number of produced Cherenkov photons can be approximated, with an accuracy within roughly 10% by [50]:

$$\frac{dN_\gamma}{dl} \approx 33 N_e F(1.57 E_s) e^{-h/H_0} \text{ photons/m} \tag{1.19}$$

where N_e is the number of electrons, $F(E)$ the electron fraction with energy $> E$ [**?**], E_s is the energy threshold for the Cherenkov photon emission by an electron, h is the production height and H_0 is an atmospheric scale factor.

The angular distribution of the Cherenkov light depends on the angular distribution of electrons in the shower. In the angular range not Chereknov light dominated ($\theta > 25°$) the angluar distribution is:

$$\frac{d^2 N_\gamma}{dl d\Omega} = \frac{dN_\gamma}{dl} \frac{e^{-\theta/\theta_0}}{2\pi sin\theta} \tag{1.20}$$

whose characteristic angle θ_0 depends on the Cherenkov threshold and is given by

$$\theta_0 \approx 0.83 E^{-0.67} \tag{1.21}$$

1.8 Detection Techniques

The rapid decrease of the integral flux makes extremely difficult the direct observation of primaries of energy $E > 10^{15}\ eV$. For this reason the study and detection of cosmic rays uses different techniques depending on the energy region of interest. Instruments as calorimeters, emulsion chambers, and others can be used to detect primaries up to $E = 10^{14}\ eV$. At these energies the cosmic ray flux is high enough to use compact devices connected to balloons or satellites launched in the higher part of the atmosphere, allowing a *direct* detection of the primaries. At energies $E > 10^{15}\ eV$, the study is necessarily performed detecting the shower of secondary particles that originates from the interactions of the primaries with the atmosphere: this is named *indirect* detection technique.

The indirect detection technique spans an energy range from $10^{12}\ eV$ to the highest detectable energies. Different kind of detectors are used according to the energy range of interest.

$10^{12} < E < 10^{14}\ eV$

At E $=10^{12}\ eV$ primaries are not able to induce a shower of secondary particles detectable at ground, so the technique consists in the detection of the Cherenkov light prduced by electrons in the higher part of the atmosphere. The Cherenkov light is collected by mirrors and focused on PMTs positioned in their focus. The detected light is related to the energy of the electromagnetic component of the shower and hence to the primary energy. This technique can be used only in moonless light with good atmospheric conditions, hence its duty cycle is limited to $\sim 10\%$.

$E > 10^{14} eV$

At these energies, primaries are able to induce a shower detectable at ground, hence the shower particles can be directly detected. Detectors as scintillators of water Cherenkov stations disposed at ground to form an array are usually adopted for this purpose (see fig. 1.10). Since the higher is the energy of the shower, the wider is the shower front, array stations must be disposed in order to achieve a good compromise between sampling of the lateral distribution of particles and energy region of interest.

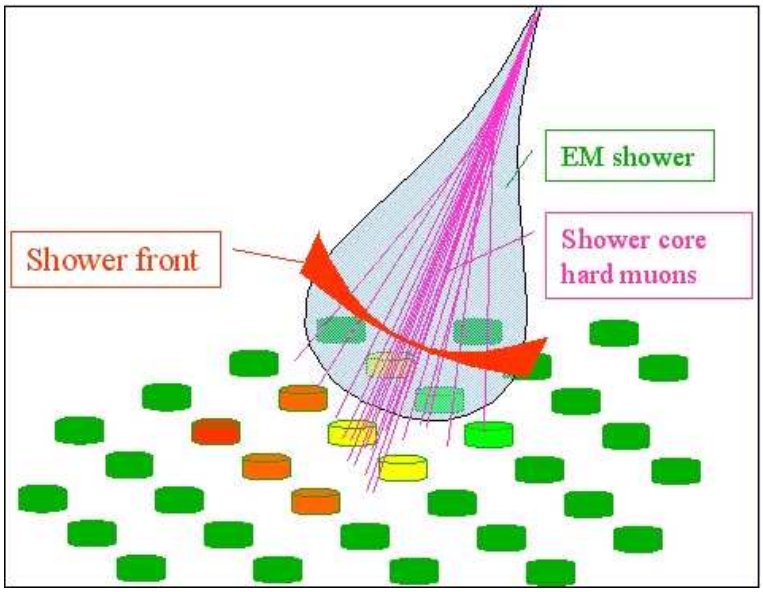

Figure 1.10: Schematization of the arrival of a shower of secondary particles on the array of surface detectors.

$E > 10^{17}\ eV$

At energies above $10^{17}\ eV$ the production of fluorescence light becomes significant, hence it can be detected using telescopes centered in the $300 - 420$ nm wavelenght range. Since this mechanism has an efficiency of 0.5%, only at these energies the light emitted becomes really distinguishable from a background light coming from the stars and the moon.

The detection of the fluorescence light emitted by the shower allows to "photograph" its development. The first complete experiment based on this technique was the Fly's Eye experiment [50] that started to take data in 1982: its name derived from its structure, 67 mirrors with 880 photomultipliers, displaced over a semi-spherical surface. It has now been replaced by its updated version, the High Resolution Fly's Eye (HiRes).

From signal timing and intensity measured by such a detector it is possible to reconstruct the axis and the longitudinal profile of a shower and then to perform a calorimetric measurement of the energy and a direct observation of the shower shower maximum.

In figure 1.11 a schematization of all the techniques used for the detection of secondary particle showers is shown.

1.9 Towards the UHECR puzzle solution

1.9.1 The pre-Auger situation

Although a century of adventurous researches and detailed studies is passed, the UHECRs still show unanswered questions: their nature, sources and how they propagate are unknown.

The two most recent and relevant experiments working on these topics have been AGASA [52, 53, 54], that employed the ground array detection technique, and HiRes [55], that detected cosmic ray showers by means of the fluorescence light emitted during their development through the atmosphere.

They reported results in disagreement. The HiRes Collaboration has observed the ankle, at an energy of 4 EeV and a sharp reduction in the flux above 6×10^{19} eV [56]. Extrapolating the power law with which can be fitted the spectrum at lower energies, above $10^{19.8}$ eV they would have expected 39.9 events, while only 13 are found. The statistical significance of this spectrum reduction is ~ 5 standard deviations.

HiRes Collaboration reported also results about cosmic ray compositions, that support the idea of a proton dominated cosmic radiation in this energy range. In fig. 1.12 a compilation of data on X_{Max}, coming from several experiments including HiRes, for energies above 10^{14}, is shown as a function of

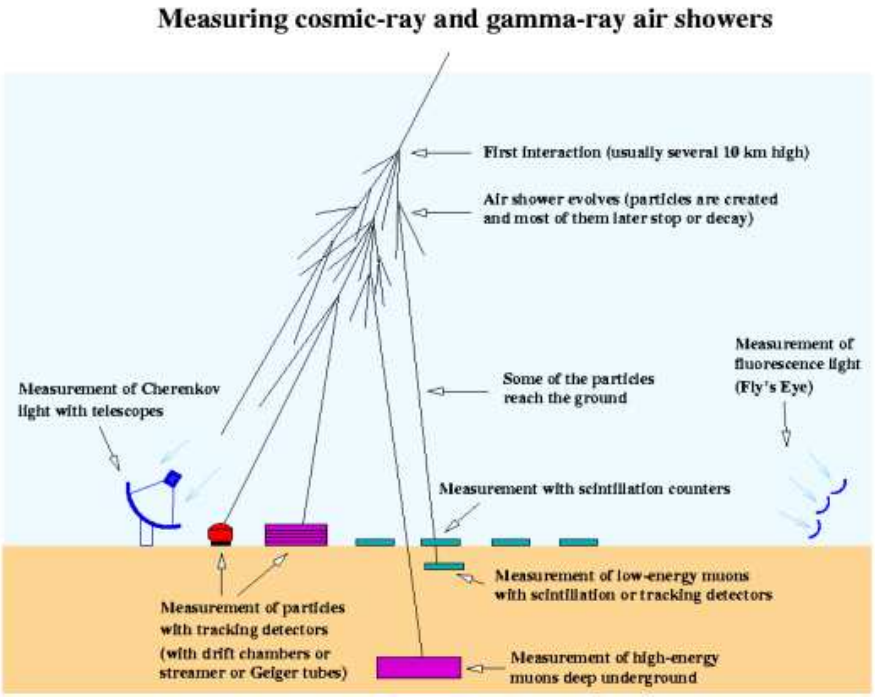

Figure 1.11: Schematization of all detection techniques of cosmic rays above 10^{12} eV.

the energy, compared with expectation values from MonteCarlo simulations of iron nuclei, protons and photons, with three different hadronic interaction models. The data indicate that above the knee the average mass becomes heavier, approaching the iron expections. However, above 10^{18} eV, the trend suggests a change towards a regime of proton dominance.

Giving the light measured composition, the reduction of comsic ray flux is at just the right energy to be caused by the GZK energy loss mechanism.

On the other side, the AGASA Collaboration did not observe the end of the spectrum, they reported 17 events above 10^{20} eV [57], that contradict the flux reduction seen by HiRes. Also the normalization is different. In fig. 1.13 energy spectra from HiRes and AGASA experiments are shown.

These open issues have bees already addressed by the Auger Observatory [58], which combine the two complementary detection techniques adopted by the aforementioned experiments (see chapter 2).

Nowdays, the Pierre Auger Observatory already achieved an exposure grater about 3 times greater than AGASA and comparable to that of the

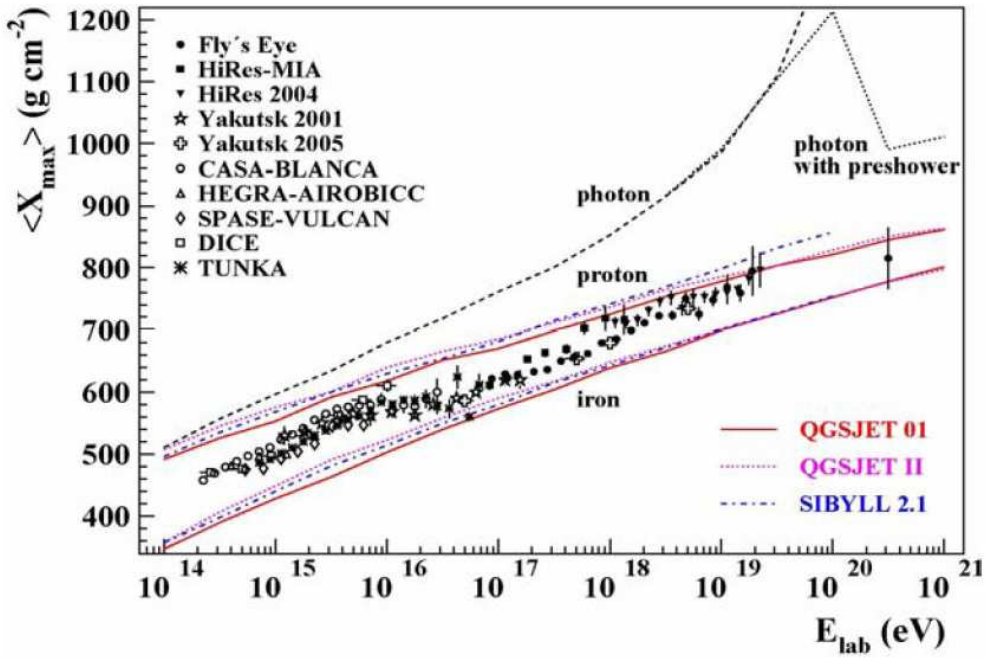

Figure 1.12: Compilation of data on the X_{Max} as a function of the energy compared with predicions from simulations of incident photons, protons and iron nuclei with three different hadronic interaction models.

monocular HiRes detectors at the highest energies and more events have been recorded at the Observatory with energy above 10^{18} eV than have come from the sum of all previous experiments. During the period 1 January 2004 - 31 August 2007, the Auger Observatory has collected 81 events with energies exceeding 40 EeV and zenith angles smaller than 60°, achieving an integrated exposure of 9.0 $\times$ 10^3 km^2 sr yr.

At the last ICRC in Mérida, México 2007, the Auger Collaboration presented its last results about the energy spectrum and mass composition.

1.9.2 The Pierre Auger Energy Spectrum

The hybrid characteristic of the Auger detector allows to estimate a cosmic ray energy spectrum not strongly dependent on our knowledge of mass and hadronic interactions.

In fig. 1.14 the measured Auger energy spectrum is shown, based on 5224 events. A slope (-2.62±0.03) between 4.5 $\times$ 10^{18} eV and 3.6 10^{19} eV [61] is

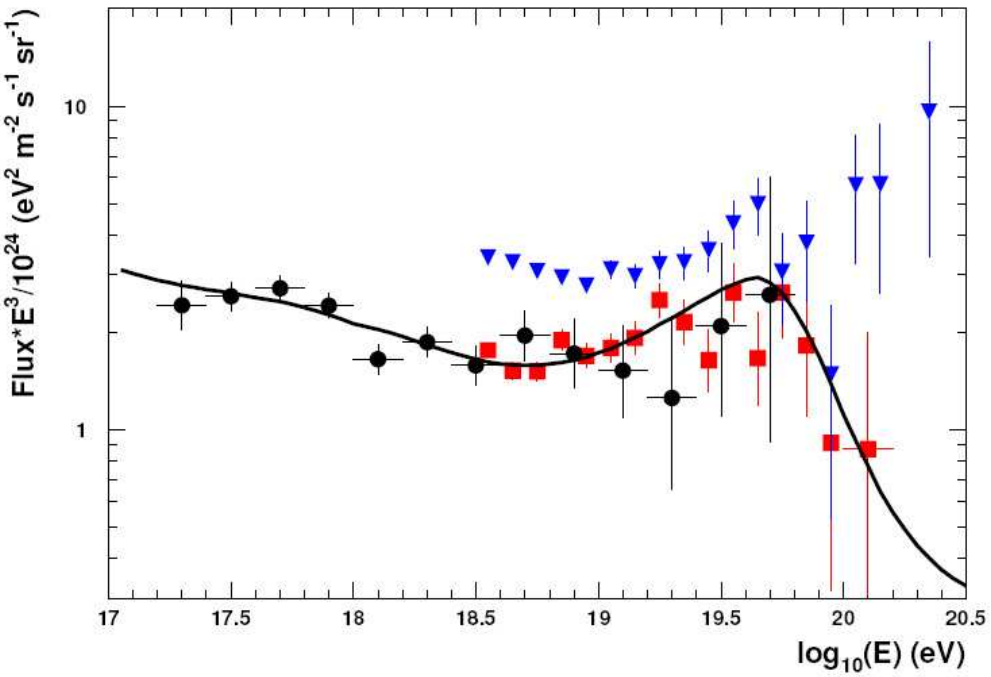

Figure 1.13: High energy cosmic ray spectrum multiplied by E^3 to evidenceits features, as seen by *AGASA* (blue triangle), by HiRes-II (black full circle) and HiRes-I (red full square). The continuous line is the predicted flux coming out from an isotropic source model.

measured. If this power law behavior is extrapolated at higher energies, the number of events expected above 4 EeV and 100 EeV are (132 ± 9) and (30 ± 2.5), while the observed numbers are 51 and 2 respectively. A steepening in the spectrum is clearly visible above 4 EeV with a significance of $\sim 6\ \sigma$. The spectrum has been compiled with SD data with zenith angles lower than 60° and recorded up to 28 February 2007, with energy above 3 EeV (energy range in which the detector is fully efficient). To gain more exposure, it is possible to calculate a spectrum with data having zenith angles ranging between 60° and 80° (named HAS, Horizontal Air Showers). The HAS spectrum contains 734 events and presents a slope of (-2.7±0.1) [62]. The spectrum has been extended at lower energies, down to 10^{18} eV, using hybrid data with at least one triggered tank [63].

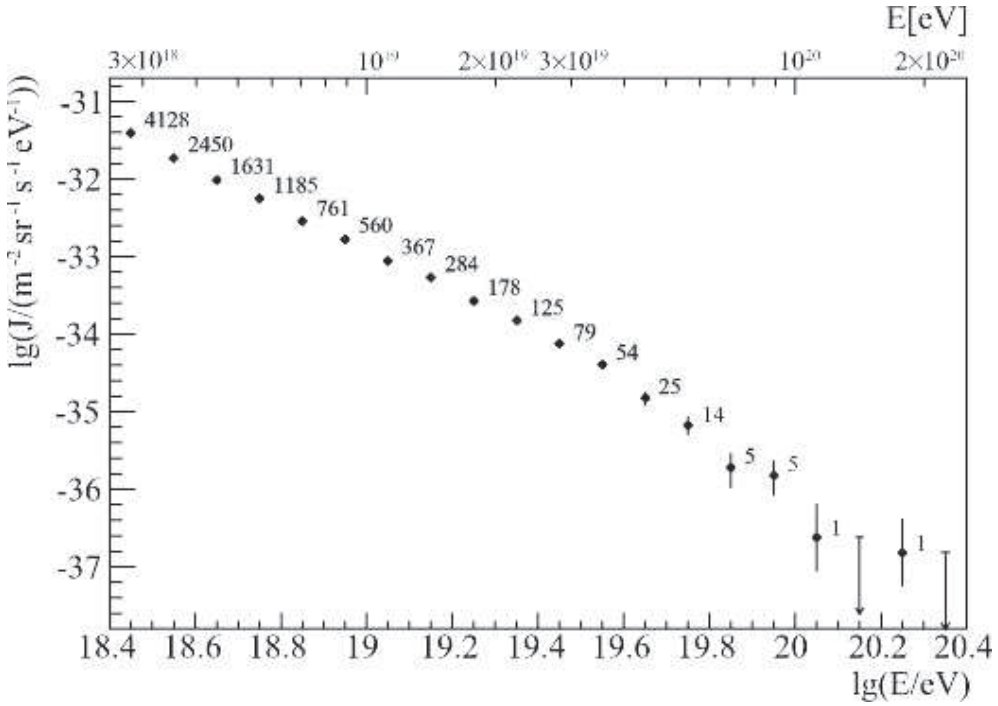

Figure 1.14: The Auger Energy Spectrum

In fig. 1.15 the three spectra are displayed together and they are completely consistent in the region where they overlap. At $\sim$ 4.5 EeV an ankle structure is clearly visible and a steepening is seen a decade higher. Only two events above 100 EeV have been detected and the integral flux above this energy is about 1 event per km^2 per sr per millennium.

1.9.3 Auger Mass Composition

The Auger telescopes could measure directly the depth of shower maxima with a systematic uncertainty less than 15 g/cm^2, if suitable cuts are adopted [69].

In fig. 1.16 the measured X_{Max} compared with the predictions of various MonteCarlo simulations is presented, for a data set of 4105 hybrid events, in which at least one surface detector has been used to constrain the geometry. The data indicate a change in the slop at 2-3 EeV, almost at the same energy in which is possible to see an ankle structure into the energy spectrum. At the highest energies, the cosmic radiation seems not proton-dominated, with

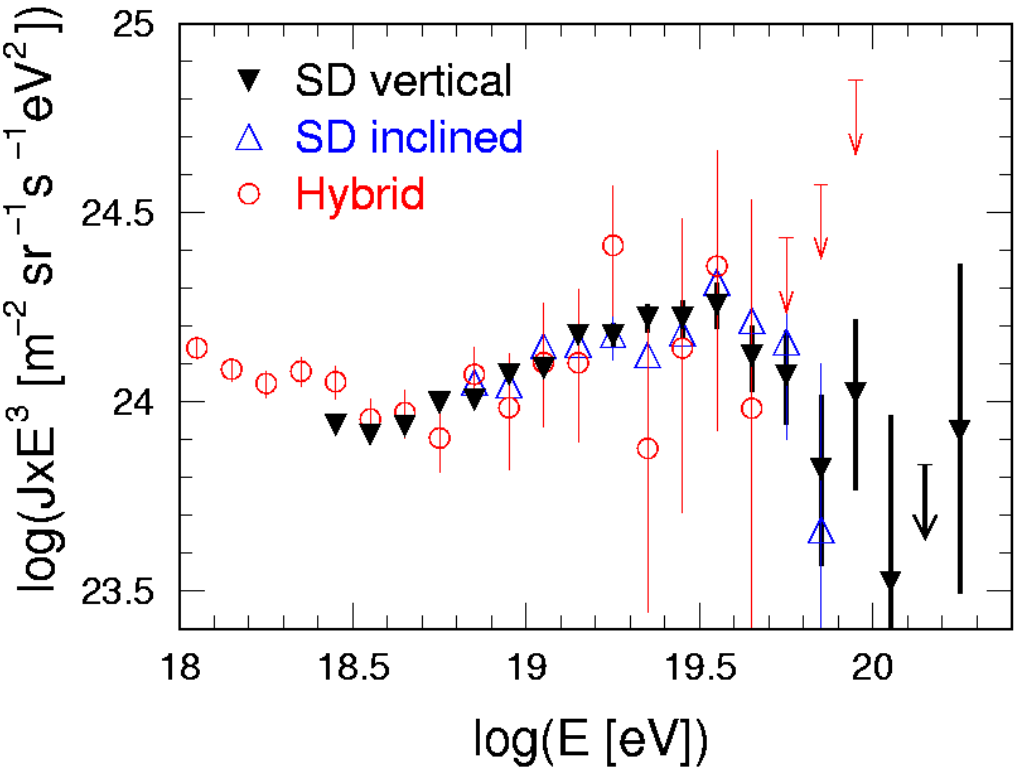

Figure 1.15: Comparison of the energy spectra of cosmic rays obtained with vertical SD, inclined SD and hybrid events.

a mean mass number of about 5.

This unexpected result assumes shower models to be broadly correct.

Auger photon limits

In the so-called "top-down" scenarios, for the production of UHECRs, a significant proportion of CRs at the highest energies would be UHE photons. The predictions are in the range 10% to 50% above 10^{19} eV, depending on the model [70].

The Auger Collaboration recently reported a limit to the photon fraction of the cosmic radiation, independently measured with hybrid data and with ground array only data.

The direct measurement of X_{Max} contained in the hybrid data has been used to discriminate between photonic and nucleonic UHE primaries. As shown in fig. 1.12, the expection values for photon primaries are much more

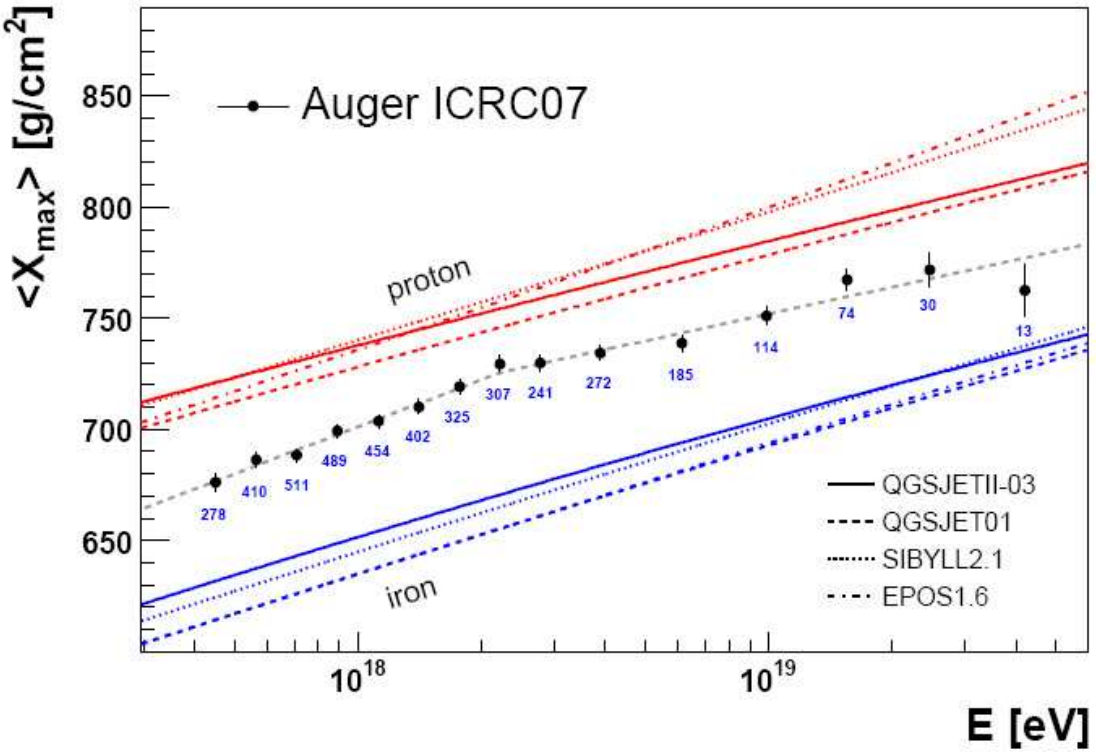

Figure 1.16: Depth of shower maximum as measured with Auger hybrid data in which at least one surface detector has been used to constrain the geometry. Predictions of several hadronic interaction models for pure-protons or pure-iron nuclei are also shown.

deep into the atmosphere than a nucleonic induced shower, due to the lower multiplicity in particle production in an electromagnetic cascade. Taking into account the systematic uncertainties related to the X_{Max} determination and the photon shower simulations employed, the Auger analysis on hybrid data put an upper limit on the photon fraction of 13% above 10 EeV [71].

The analysis relying on only ground array measurements has as key observables the signal risetime (i.e. the time it takes for the signal to rise from 10% to 50%) at 1000 m and the radius of curvature of shower front. Particles with a deeper X_{Max}, as photons, are indeed expected to reach the ground in

a thicker and more curved front. This analysis could use around 10 times more statistics compared with the hybrid detection. No photon candidates were found and an upper limit on the photon fraction of 2.0%, 5.1% and 31% at 10, 20 and 40 EeV respectively has been set [72].

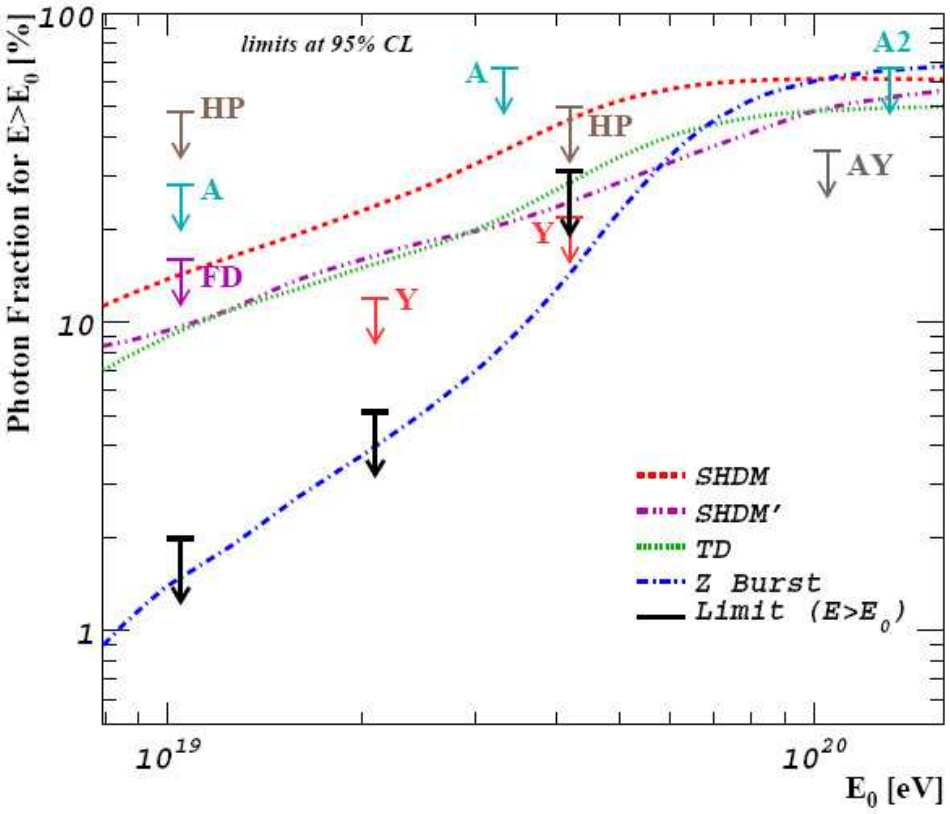

Figure 1.17: Upper limits to the photon fractions obtained by the analysis of hybrid data (labelled FD) and ground array only data (black arrows) compared with predicted photon fluxes from several models [73]. Limits set by AGASA (labelled with A [74] and A2 [75]) by Haverah Park [76](HP) and Yakutsk [77] (Y) are also shown.

In fig. 1.17 the photon limits put by Auger are shown. Auger results disfavour many of the top-down models proposed in connection with the AGASA spectrum that contradicts the existence of the GZK-limit.

Auger neutrino limits

The Auger Observatory ground array is a suitable instrument to identify the shower electromagnetic component (see section 2.4). With this characteristic, it is possible to detect and identify UHE neutrinos in the EeV range and above [78]. The main experimental challange is to identify neutrino-induced showers in the hadronic-induced background. The point for the indentification is to exploit the feature that neutrinos can penetrate large amounts of matter and generate a "young" shower close to the observation level. The hadronic background can be reduced searching for "young showers" among very inclined events. Two different neutrino detection channels have been identified:

- Earth-skimming tau neutrinos, expected to be detected through the detection of showers induced by the decay products of an emerging τ lepton, generated by ν_τs crossing the Earth [79];
- down-going neutrinos, that is sensitive to all neutrino flavours and in which young showers are searched for among showers with zenith angles between 75° and 90° [78].

Recently the Auger Collaboration presented its neutrino limit, using the first detection channel (the analysis on down-going neutrino is still in progress). In fig. 1.18 the Auger limit is compared with other limits. The limit improvement by an order of magnitude will require several years of operation, the Auger limit is anyway the best to date in the energy range where the GZK neutrinos are predicted.

1.9.4 Observation of Anisotropy of UHECR

The search for anisotropies in the arrival directions of UHECRs has been a goal since their discovery. Since at GZK energies they are not expected to be confined by magnetic fields in the disk of our galaxy, it is likely that they originate outside the Galaxy. Furthermore, the existence of the GZK cut-off imposes that thay must have been produced relatively nearby. So, considering that at 10^{19} eV a proton has almost a balistic trajectory and selecting those events with the largest magnetic rigidity, it should be possible to do particle astronomy and check if those events can be combined into clusters pointing to individual point sources or correlated with a collection of astrophysical objects. The AGASA Collaboration claimed an excess of clustering at small angular scale respect with the isotropic expectation [64], this claim was contradicted by HiRes data [65]. Analysis of data recorded

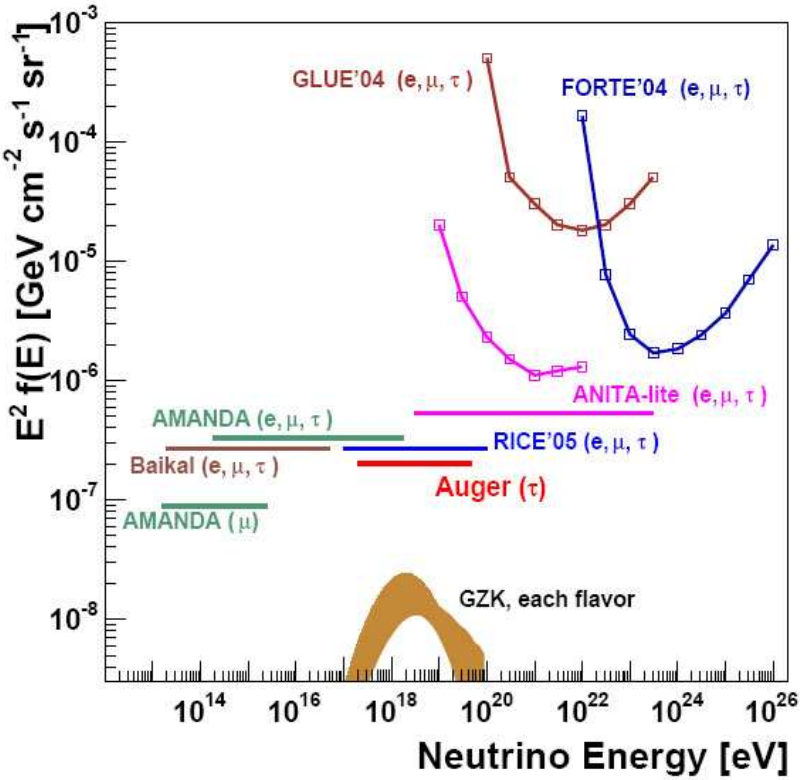

Figure 1.18: Auger upper limit on an E^{-2} diffuse flux of UHE ν_τ, compared with predictions for GZK neutrinos and other experimental limits.

by several cosmic ray experiments revealed a general correlation with the supergalactic plane [66], but with limited statistical significance.

Recentely, the Pierre Auger Collaboration reported the observation of a correlation between the arrival directions of comsic rays with the highest energies measured by the Pierre Auger South Observatory and the positions of nearby AGN [67] from the 12^{th} edition of the catalog of quasar and active nuclei by Véron-Cetty and Véron (V-C catalog) [68]. The departure of the arrival direction distribution from an isotropic one has maximum significance for cosmic rays with energy above 6×10^{19}, in correlation with AGN lying within $\sim$ 75 Mpc. The Pierre Auger Collaboration analysis confirmed the anisotropy hypothesis and the correlation with a confidence level of more than 99% using data collected from 27 May 2006 through 31 August 2007, with parameters specified a priori. The used parameter values are those corresponding to the minimum of the probability P for a set of N events

from an isotropic flux to contain k or more events at a maximum angular distance ψ from any member of the collection of candidate point sources, as obtained from an exploratory scan done with data collected from 1 January 2004 through 27 May 2006. The parameters used in the exploratory scan are the lower energy threshold E^{th} for the cosmic ray events, the maximum source redshift z_{max} and the maximum angular separation ψ. The minimum of P is obtained with $E \geq E^{th} = 56$ EeV, $z_{max} = 0.018$ (≤ 75 Mpc) and $\psi \leq 3.1°$. Applying the analysis to the full data set, the Auger Collaboration found that 20 out of 27 cosmic rays events correlate with at least one of the 442 selected AGN, while only 5.6 were expected for an isotropic flux.

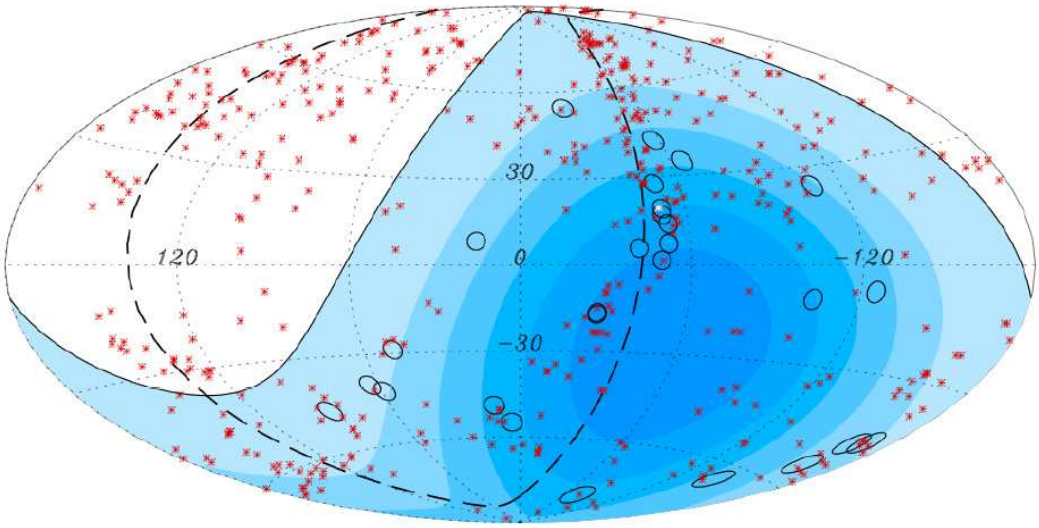

Figure 1.19: Aitoff projection of the celestial sphere in galactic coordinates: the arrival directions of cosmic ray events are represented by 3.1° circles; sky regions with a larger relative exposure are indicated by darker colors; AGN with redshift $z \leq 0.018$ from the V-C catalog are indicated by asterisks and Centaurus A, one of the our closest AGN, is marked in white; the solid line draws the Observatory field of view (zenith angles $\leq 60°$); the dashed line is the supergalactic plane.

In fig. 1.9.4 the sky map as seen by the Auger Observatory is presented, with circles of 3.1° centered at the arrival directions of the 27 events with energy above 57 EeV and asterisks indicating the positions of AGN with

redshift lower than 0.018 from the V-V catalog.

It is clear that with the present statistic is not possible to unequivocally identify the sources, but the Auger Observatory will gather a huge statistic in a few years.

The energy threshold found matches the energy range in which the energy spectrum measured by the Observatory gets reduced by 50% with respect to its power law extrapolation at lower energies. The correlation is consistent with the hypothesis that cosmic rays above 60 EeV are mostly protons and come from sources within our "GZK horizon".

Chapter 2

The Auger Experiment

2.1 Introduction

The Pierre Auger Project is the result of an international effort to measure properties of cosmic rays at the highest energies by detecting Atmospheric Air Showers with unprecedented statistics and precision: 17 countries, about 70 Research Institutes and Universities from all over the world, involving more than 300 physicists, are taking part in the construction and data analysis of the Auger Observatory.

The observatory has been optimized to answer all the open questions on $UHECR$: the spectrum and the mass composition in the $GZK-$region; observation of point-like sources of cosmic rays (or small scale anisotropy); observation of large scale anisotropy.

The Auger South Detector, presently in its final phase of construction, consists of 1600 Cherenkov detectors (tanks) filled with water (Surface Detector, SD) overlooked by 24 telescopes for the detection of the fluorescence light (Fluorescence Detector, FD). Each tank has a volume of 10 m^3 and 3 photomultipliers look at the water inside; tanks are spaced at a distance of 1.5 km each, on a triangular grid, to cover an area of 3000 km^2. The 24 telescopes of the Fluorescence Detector are positioned in 4 stations (eyes) disposed at the borders of the area occupied by the SD. This configuration is chosen to maximize the number of events recorded at the same time by both detectors (hereafter referred as *"hybrid events"*).

The experiment is already solving one of the main problems related to $UHECR$ studies: the lack of statistics. More events of energy above $10^{18} eV$ have been already recorded at the Observatory than have come from the sum of all previous efforts [80].

Pierre Auger Obseratory main features are:

1. **Full Sky coverage:** The project consists of a two-sites observatory, one for each terrestrial hemisphere, in order to provide a full sky coverage, crucial to study the arrival direction distribution. The Southern Observatory is now going to be completed in the Pampa Amarilla near Malargüe, in the Mendoza Province, Argentina. The Northern Observatory should be built near Lamar, Colorado (USA).

2. **Large Aperture:** The Auger South Observatory will cover a 3000 km^2 area; because of its huge aperture, the southern observatory will provide high energy data with high statistics. The Northern Site will most probably cover an area of $\sim$ 10000 km^2.

3. **Hybrid Detection:** The southern observatory is equipped with an array of water Cherenkov particle detectors (SD) to measure the distribution of particles at ground and by four fluorescence stations (FD) to observe the development of the shower in atmosphere. The observatory design is conceived to maximize the fraction of detectable events by both SD and FD. The combined use of these two detection techniques will provide a cross-calibration and better event reconstruction accuracy. In the Southern Observatory a new CR detection technique is being tested, based on the detection of an EAS by means of radio emissions by electron-positon pairs produced by the shower [81]. First results of cosmic rays radio detection are currently being presented to the Collaboration; in case of success of EAS radio detection, the Northern Observatory could be largely instrumented with antennas for radio detection.

Auger South Enhancements

The Pierre Auger Collaboration has decided to include detector enhancements in order to have unitary detection efficiencies down to 10^{17} eV in cosmic rays detection. These enhancements consist in high elevation FD telescopes ($HEAT$, 60° of elevation instead of 30°) and an infill area ($AMIGA$) with both surface detectors and underground muon counters thus allowing a detailed study of the spectrum region where the cosmic rays sources are assumed to change from galactic to extragalactic origins. Presenltly telescopes and muon counters are under construction.

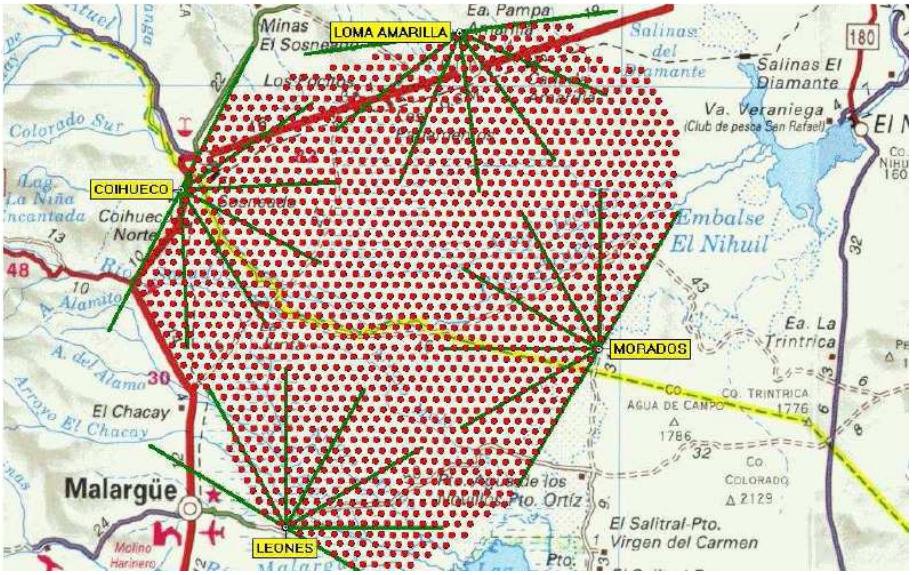

Figure 2.1: The southern site of the Pierre Auger Observatory (Argentina, Mendoza Province).

2.2 The Hybrid Detector

The main feature of the apparatus is its "hybrid" nature: Cherenkov detectors and fluorescence telescopes can perform independent and complementary measurements on showers developing in the field of view of both detectors. The SD measures the lateral and temporal distribution of EAS particles reaching the observation level, while the FD registers their development in the atmosphere: unprecedented precision in the study of showers is reached with the contemporaneous use of both detectors. Both techniques have been separately used in previous experiments (see HiRes and AGASA), but their results turned out to be not consistent at the highest energies (see section 1.9.1).

The surface detector is similar to the apparate built for the Haverah Park [82] experiment, but on larger scale, while the optical component of the observatory makes use of the fluorescence technique tested with success for the first time in the Fly's Eye experiment [83]. While the SD has a 100% duty cyle, the FD can work only during moonless nights with good atmospheric conditions, with a duty cycle of $\sim 10\%$ (it will approach 14% in stable configuration). For this reason, only a fraction of the data collected by the surface detector are also hybrid events.

Both methods have some limits in retrieving the energy spectrum of cos-

mic rays: a fluorescence detector has a direct calibration in energy but its aperture is unknown; on the other hand, the surface detector has a well known aperture but an indirect calibration in energy.

SD energy estimate procedure derives SD energy calibration, by means of simulation methods that are strongly influenced by the hadronic interaction models. On the other hand the FD aperture grows with energy, because events producing more fluorescence light are visible at larger distances, and it also changes night by night, since it is function of the night sky background luminosity and of the atmospheric transparency.

Auger strategy for energy estimate makes use of hybrid events to intercalibrate the detectors, providing confidence in the surface array results alone.

The choice to use both techniques at the same time is based upont the following considerations:

1. **Intercalibration:** the two techniques measure independently and at the same time the energy of the primary of the shower, its arrival direction and its nature: the hybrid nature of the detector makes possible to reveal any systematic effect due to one of the two detection techniques.

2. **Sensitivity to the primary nature:** both the FD and the SD have their own ability to estimate the nature of the primary particle that induces the cascade, measuring different shower parameters. Also in this case the combined use of the two techniques allows to obtain a clearer view.

3. **Hadronic Interaction Models:** the interpretation of experimental data needs the development of an hadronic interaction model that explaines the processes. The interaction energies of events observable by the Auger Observatory (10^{21} eV in the laboratory reference system) are much higher than the energies reached with particle accelerators, also higher than the maximum energy that will be reached with LHC (14×10^{12} eV in the center of mass reference system). So, models developed starting from the study of laboratory processes are not perfectly suitable to describe EAS production processes (lower energy, study of collision processes in the center of mass system instead of the laboratory system, observation of the reaction products at large scattering angles instead of looking at the fragmentation zone, prevalent study of particle-antiparticle processes instead of proton-nucleus or nucleus-nucleus). The hybrid nature of the Auger detector allows to perform contemporaneous measurements of the muonic component, the electronic density and the longitudinal shower development of the same

EAS, so that tight limits can be defined on the hadronic interacton model used for the simulation of EAS processes.

4. **Uniform Exposure:** The installation of an Auger Observatory in both emispheres allows the full-sky study of the arrival directions of cosmic rays that at these energies are not significantly affected by the galactic/extragalactic magnetic fields, hence storing the information of the sources position. The GZK limit (1.3) predicts that sources should lie at distances D < 100 Mpc. Recent results from the Auger Collaboration on UHECR sources will be described in details.

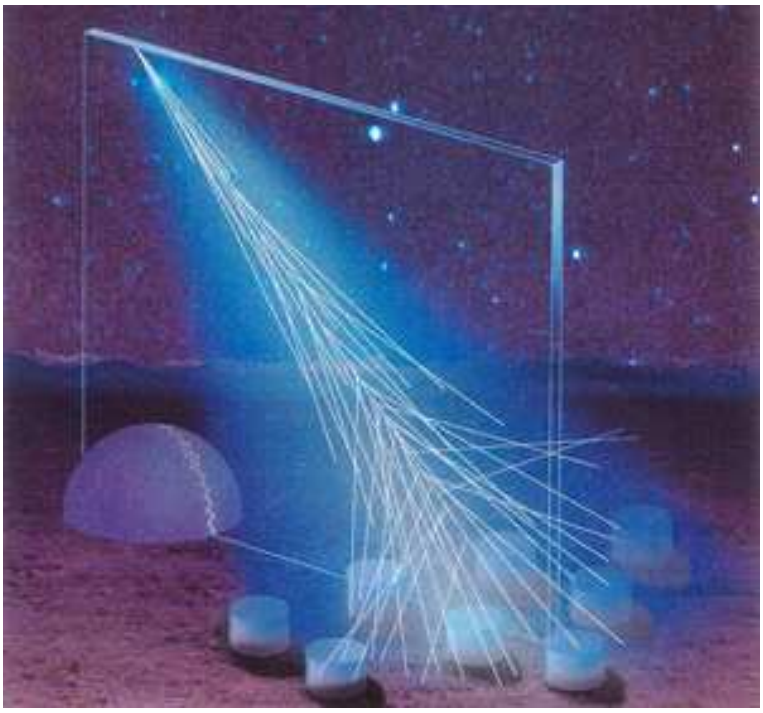

Figure 2.2: Picture of the Auger South Hybrid Detector

2.3 The Southern Observatory

The Pierre Auger South Observatory is located in Malargüe, Argentina, in the Pampa Amarilla upland, which has an altitude between 1300 and 1500 m above sea level, with an average slope of 0.5%. The ground array detectors are located over an ancient riverbed, while the 4 eyes are located over natural embankment, on top of small edges of the area. In figure 2.3 the map of the Auger South site is shown. The four fluorescence detectors are all in operation

(the last eye, Loma Amarilla, started data acquisition in May 2007), and the area already covered by Cherenkov tanks is highlighted in cyan; the situation at september 30^{th} 2007 is shown. The completion of the array is planned for early 2008; presently 1464 tanks are operating out of 1539 that are in the field. It is expected that all tanks will be opeating by March 31^{st} 2008.

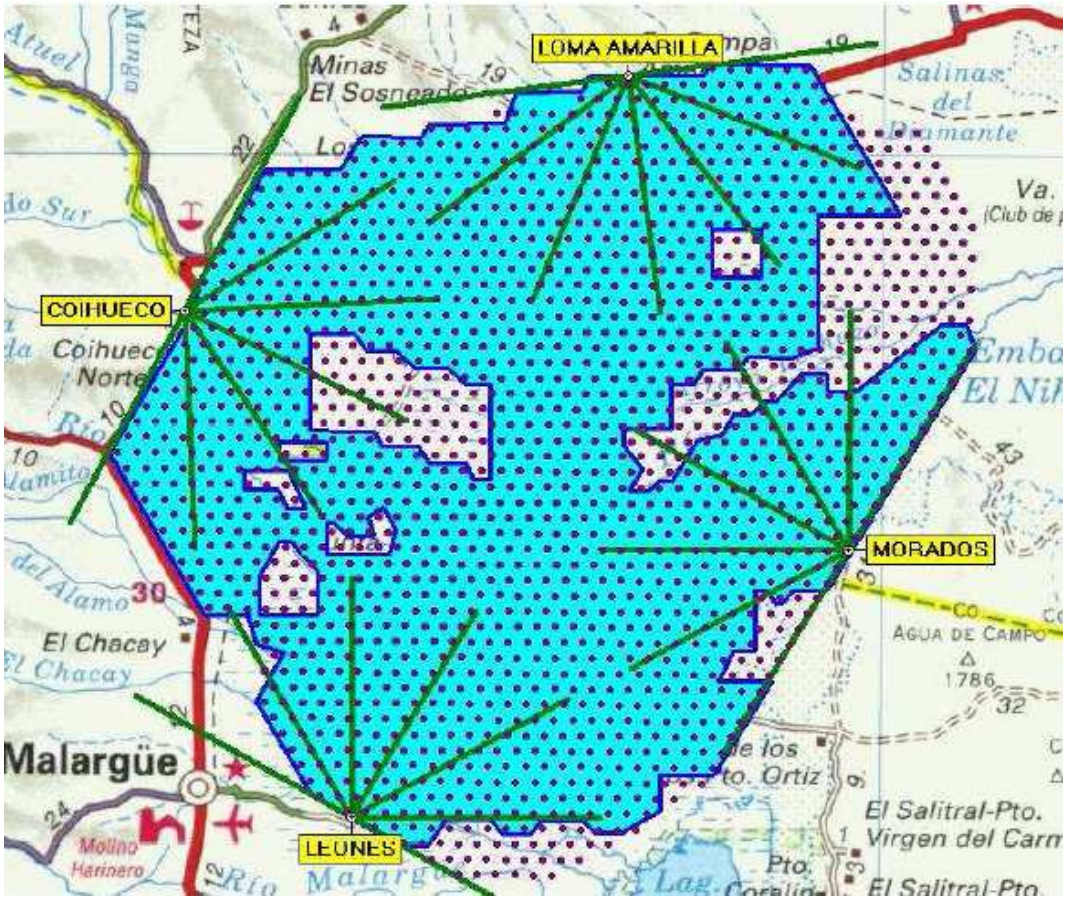

Figure 2.3: Pierre Auger Southern Observatory map. Dots represent surface array detectors, labels correspond to 4 fluorescence eye building. The lines mark azimuthal field of view of each telescope. Cyan area represents operational tanks (situation at september 30^{th} 2007).

The Observatory includes a Central Campus (see fig. 2.4), located in Malargüe, where there are the assembly center, the central data acquisition system ($CDAS$) and the offices.

Figure 2.4: Central Campus building in Malargüe.

2.4 The Surface Detector: SD

The Auger South Surface Detector (SD) is built to measure the lateral density and the time distribution of the shower secondary particles reaching the ground. These parameters are closely related to the energy of the primary that induced the shower, to its arrival direction and to its nature.

The SD consists of 1600 water Cherenkov detectors (*tanks*), disposed on a triangular grid at a distance of 1.5 km each, to cover the 3000 km^2 area, for a $\sim$ 7000 km^2 sr total aperture for zenith angles $\theta < 60°$. The distance between the tanks was established on the basis of the initial requested efficiency of 100% for events with an energy above 10^{19} eV and to have a good sampling of the lateral distribution density. With a spacing of 1.5 km the number of triggered stations is large enough (15 to 20 units) at the very highest energies ($E > 10^{20}$ eV) to allow high quality and unambiguous event reconstruction. With the present configuration the full efficiency is reached at 3×10^{18} eV.

Water Cherenkov detectors have been chosen for the ground array mainly

because of their capability to distinguish muon from electromagnetic component pulses; moreover they show a good sensitivity in detecting inclined showers (high zenith angles), and are quite cheap. An array of 200 water Cherenkov detectors covering a 12 km area has been used for more than 20 years in the Haverah Park experiment; the experience accumulated on these detectors has been useful for the development of the surface array of the Auger experiment. The long time of activity in Haverah Park demonstrates that such an apparate can work for long periods of time with high stability and low costs for mainteinance.

Figure 2.5: A Surface Detector station with the Los Leones FD building in background.

2.4.1 Cherenkov detectors

The ground detector unit, or *tank*, is an opaque cylinder where particles produce light by Cherenkov radiation. Each cylinder has a diameter of 3.6 m and is filled with deionized water up to 1.2 m in height. Three large Photonis XP1802 hemispherical photomultiplier tubes with 9 in diameter (see fig. 2.6) look at the inner water and are placed at 1.2 m from the cylinder axis, in steps of 120° on the upper cylindrical surface. The inner deionized water

is protected by a liner that prevents it from contamination, protects from external light and whose Tyvek surface walls reflect the Cherenkov light emitted in the water. The 1.2 m height of the water in the tank is chosen to optimize muon detection; it is enough to absorb the 90% of the incident electromagnetic shower particles. Muons passing through the tank produce a signal proportional to the distance traversed in the tank itself.

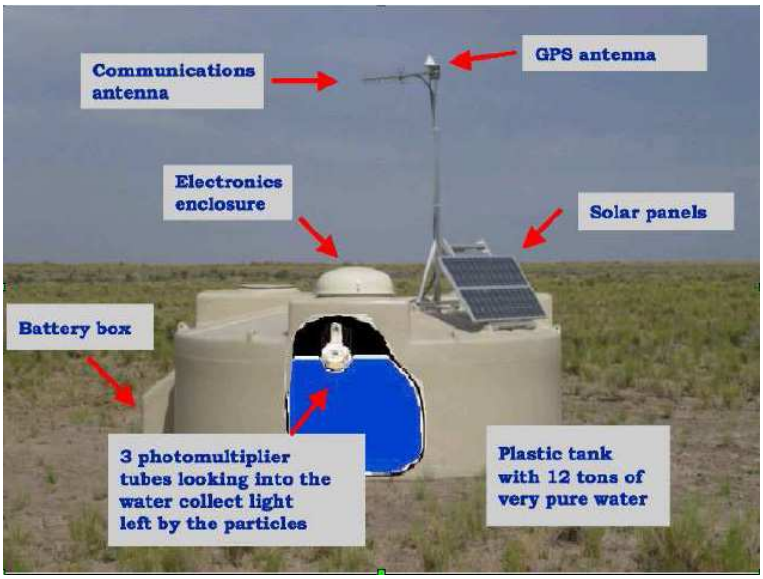

Figure 2.6: Schematization of a surface detector station (SD).

Tanks are equipped with solar panels for power autonomy, a Global Positioning System (GPS) receiver for independent absolute timing and to synchronize data from different stations and a $GSM-$like transceiver unit for wireless communications. PMT signals are digitized by 10 bit fast analog to digital converter ($FADCs$) running at 40 MHz.

2.4.2 SD Calibration

To count how many particles are crossing a tank volume in a defined time interval, the value of the signal corresponding to one crossings particle must be known. For this purpose, the concept of Vertical Equivalent Muon (VEM) has been introduced, defined as the sum of charges collected in the three photomultipliers ($PMTs$) for a relativistic down-going vertical muon crossing the detector. One VEM is then equivalent to a muon track length of 1.2 m, or 0.1 particles/m^2.

Tanks are calibrated using atmospheric muons, a well known uniform background. Atmospheric muon signal is proportional to the path length of the particles within the tank. A test tank was used to calculate the relation between down-going vertical muons and the peak of the histogram obtained from omni-directional muons. Each tank is calibrated matching the photomultipliers gain to obtain the expected trigger rate over a given VEM threshold. This procedure allows to calibrate tanks with a precision of 5%.

2.4.3 The SD operation : Trigger and Event Selection

Two different first level triggers (T1) are used: a threshold trigger (ThT) and a time over threshold trigger (ToT). The ThT is designed to trigger over fast signals, as those produced by the muonic component of very inclined showers. It is a 3-fold trigger with a threshold of 1.75 VEM for each PMT. The ToT is designed to trigger over signals produced by particles far from the core. It requires 12 FADC bins with signals larger than 0.2 VEM in a sliding time window of 3μs for 2 out of 3 PMTs [92].

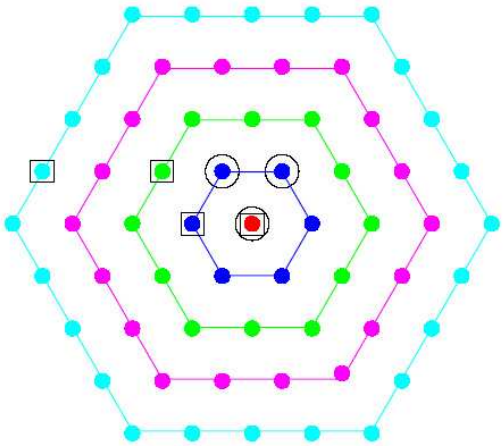

Figure 2.7: 4 hexagons with stations (dots) surrounding the central tank (red dot) are illustrated. Two example of T3 trigger are shown: a 3-fold coicidence (circles) and a 4-fold coincidence (squares).

The second level trigger (T2) is a software trigger that selects the T1 triggers to be sent to CDAS: all ToT are selected, while only ThT with all 3 coincidence PMTs with threshold 3.2 VEM pass the selection.

Second level triggers are promoted third level triggers (T3) if time and space requirements are fulfilled. At each T2, stations that have trigger within a 25 μs window are further considered: only groups of at least 3 stations are

examined for spatial coincidence. For 3-fold coincidence, triggered tanks must be within the first two hexagons centered on the station used as the center of the time bin. For the 4-fold coincidences, one station with a T2 may lie in the 4th hexagon (see fig.2.7).

The fourth trigger level (T4) is a physical trigger, used to select physical events and to reject random coincidences. The requirements are:

1. 3 tanks satisfying the ToT conditions and a minimum compactness, that is one of them must have one of its closest neighbours and one of its second neighbours triggered. The 90% of events selected by the so called $3ToT$ are physical events. It is very efficient for vertical showers.

2. $4-$fold coincidence of any $T2$ with a moderate compactness requirement, that is among 4 tanks, one can be as far as 6 km away from others within an appropriate time window ($4C1$). Only 2% of events selected by this mode are real showers, but it is absolutely needed to detect horizontal showers, which produce fast signals with a wide-spread topological patterns.

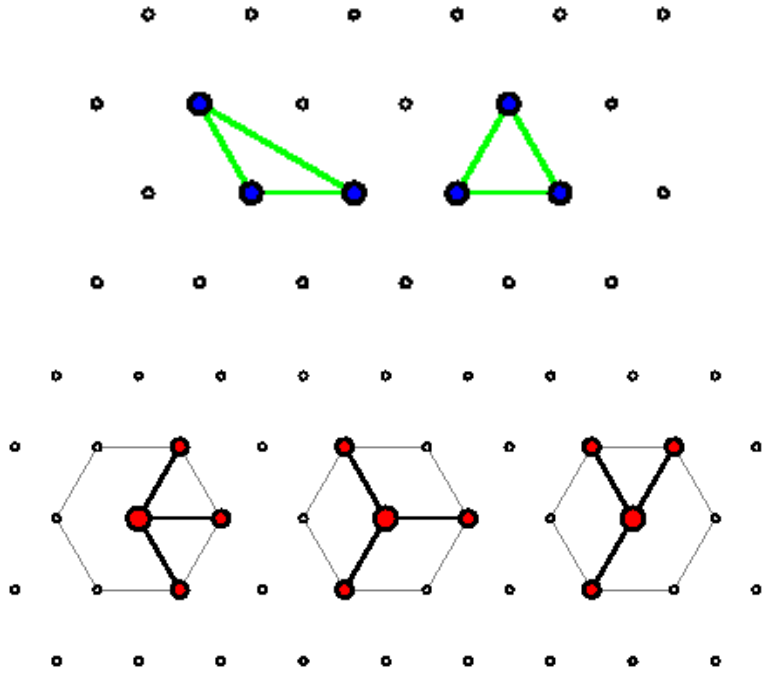

Figure 2.8: T4 trigger configurations: the two possible 3ToT configurations (top) and the three minimal 4C1 configurations (bottom).

Finally, at the moment a quality trigger (T5) requires that the T4 tank with the highest signal must be surrounded by at least 5 working stations among the closest 6 neighbours.

2.5 The Fluorescence Detector: FD

The Fluorescence Detector follows the development of the shower in the atmosphere by detecting the fluorescence light produced by the interaction of charged secondary particles [88] .

The amount of fluorescence light emitted by a shower is proportional to the number of secondary charged particles, allowing a direct measurement of the longitudinal development of the EAS in the atmosphere, in a model-independent way. From the measured shower profile and geometry the position of the shower maximum $Xmax$, which is a parameter sensible to the mass composition of the shower, can be obtained. The energy of the electromagnetic component is calculated by integrating the measured shower profile. Corrections for atmospheric attenuation of the fluorescence light and contamination of the signal by Cherenkov light are needed. Corrections are estimated using data provided by monitoring facilities at the observatory [89].

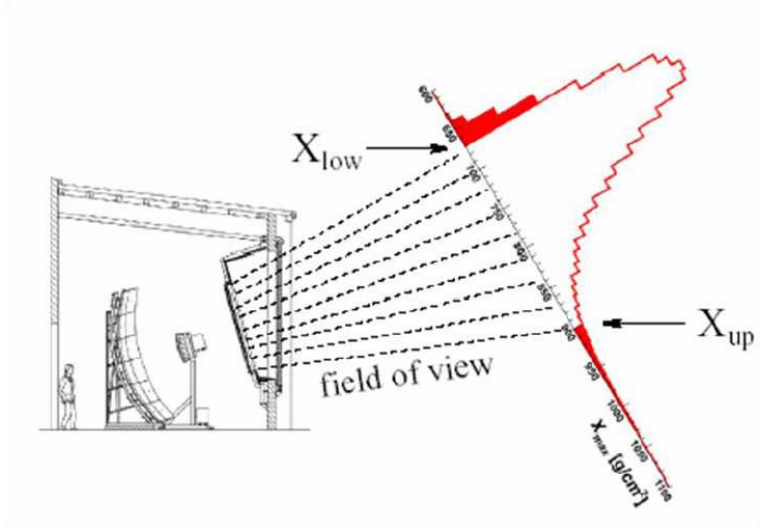

Figure 2.9: Schematic view of the longitudinal profile of a shower.

The Auger Observatory was built in order to maximize the number of hybrid events observed, so any event recorded by the FD has to be seen also

by the SD. A detailed reconstruction of the longitudinal profile of detected showers is needed to obtain an accurate energy estimate, and high precision on the X_{max} measurement is needed to achieve the required sensitivity to distinguish showers initiated by different primaries. On average, fixing the energy, the difference between a proton shower X_{max} and an iron shower X_{max} is about 100 g/cm^2: a resolution in X_{max} of 20 g/cm^2 is required in order to investigate CR primary composition.

An accurate estimate of the longitudinal profile needs an accurate geometrical reconstruction of the shower axis. At large zenith angles (very inclined showers), a small error on the determination of the zenith angle produces a significant error on the atmopsheric depth: FD monocular events (only one eye involved) are not ideal at this purpose, but hybrid reconstruction (including at least one SD tank) can easily achieve this goal.

2.5.1 FD Telescopes

The FD consists of 24 telescopes located in 4 stations built on the top of small elevations on SD area edges (see figure 2.1). Stations, named *"eyes"*, are divided in six *"bays"* each housing a telescope (see fig. 2.10). Each eye has a field of view of 180° in azimuth and 30° in elevation; each telescope has a 30° × 30° FOV. The building has a semicircolar ground plan, with radius of 14 m. Telescopes point radially outward through windows of 3 m (w) × 3.5 m (h).

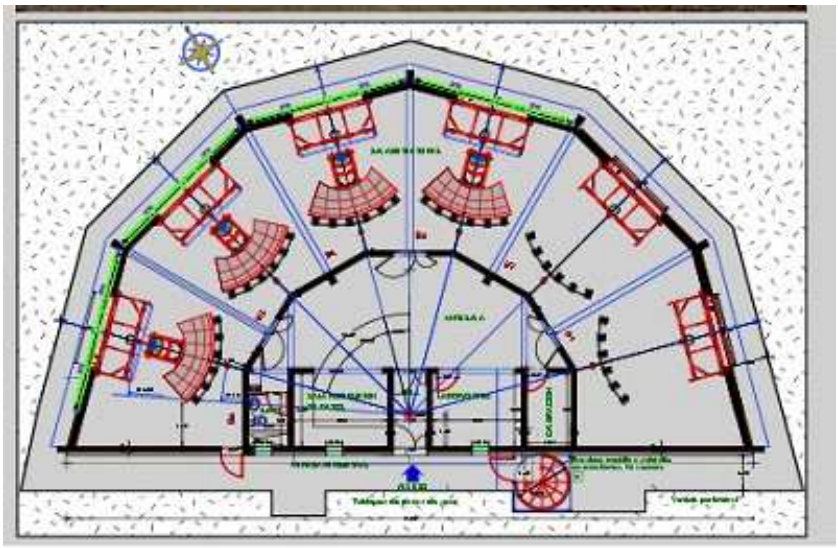

Figure 2.10: Planimetry of Los Leones (Eye1) building; 4 out of 6 telescopes are shown.

At each window corresponds an aperture mechanism from within, while outside two sliding doors (*"shutters"*) protect the telescope from daylight and can be remotely controlled.

Telescopes are constituted by:

- a light collecting system (diaphragm and mirror)
- a light detecting system (the photomultipliers matrix, or *camera*)

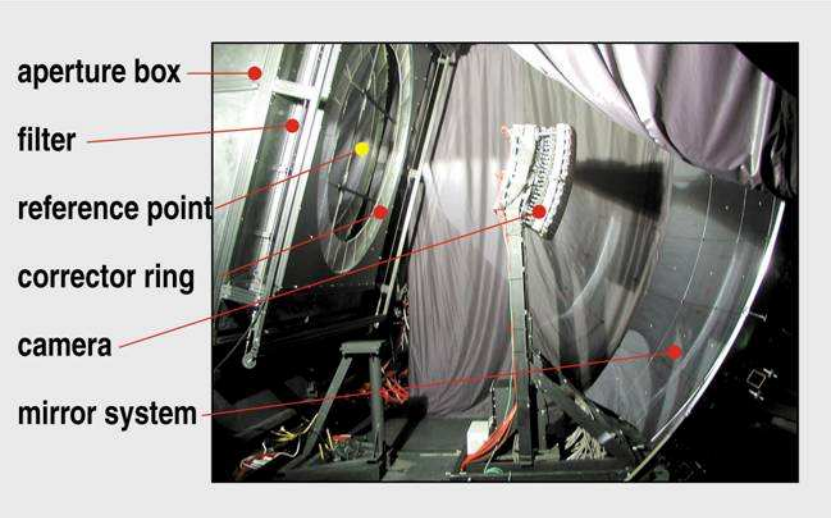

Figure 2.11: Schematic view of an FD telescope. From left to right: attached to the window shutters and the aperture system with filter and corrector ring; camera support holding a 440 PMT camera; on the floor the electronic crate; mirror and its support structure. The indicated reference point defines the center of the telescope geometry.

Light Collecting System

The Auger FD design adopts Schmidt optics to eliminate coma aberration. Telescope optics is almost completely spherically symmetric, so pixels far from telescope axis are equivalent to pixels near the axis.

The optics is composed by a large spherical mirror with radius of $R_m = 3.4$ m and a diaphragm at the mirror's center of curvature.The diaphragm is used to eliminate coma aberration and to guarantee an almost uniform spot size over a large field of view, with a size of the order of 0.5°. The spherical aberration is compensated by means of a Corrector Ring (see fig. 2.12) that

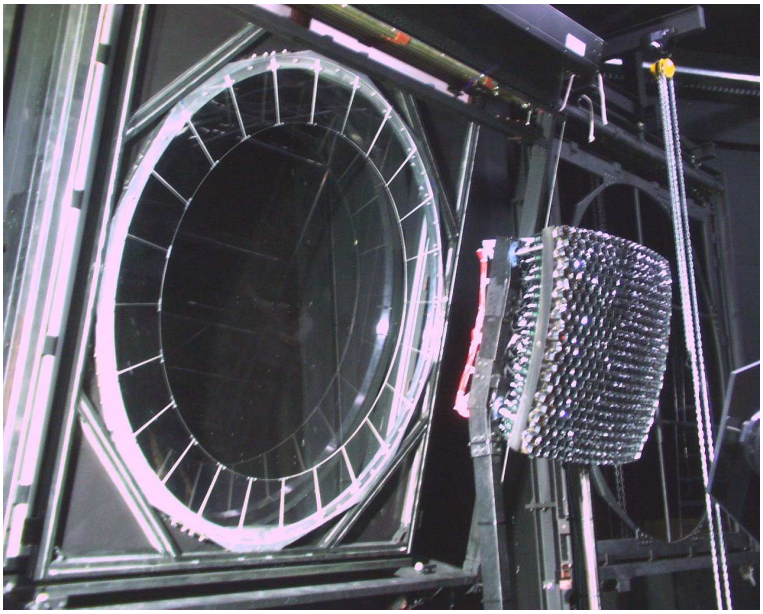

Figure 2.12: Corrector ring and PMT camera.

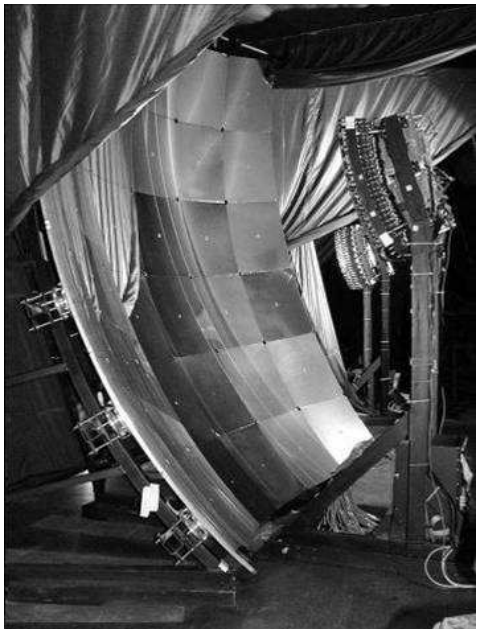

Figure 2.13: Mirror and PMT camera.

is housed in an aperture box that holds also an optical filter transmitting the nitrogen fluorescence wavelength range and blocking out most of the night sky background. The aperture of the FD building has a radius of 1.1 m.

Light Detecting System

A matrix of 440 PMT (see fig.2.12), called *pixels*, constitutes the light detecting system, or *"camera"*, where the light reflected by the mirror is detected (see fig. 2.11). The design and characteristics are fixed in order to achieve the S/N sensitivity imposed by the logitudinal profile resolution criteria. Pixels must lie on the focal surface, i.e. the spherical surface where the circle of least confusion has its minimum size. The radius of the focal surface is $R_{foc} = 1.743\ m$, with a spot size lower then 0.5°. For a better covering of the camera surface, pixels are hexagonal. As compromise between the resolution and the minimum circle of confusion, $PMTs$ have a side to side distance of 45.6 mm, corresponding to a 1.5° angular size.

For the geometrical construction of the camera a cartesian reference system xyz is fixed on the spherical surface (see figure 2.14). In the xz plane, pixel centers are positioned at a distance R_{foc} from the origin. The first center is positioned at $+\Delta\theta/2$ with respect to the z axis; the column is built moving upward starting from this first center. Moving upward in steps of $\Delta\theta = 1.36°$ in the xz plane the center of the following pixel is obtained, and so on. Rows are built moving on the x axis in $\Delta\phi = 1.5°$ steps. Pixel vertices positions (see fig. 2.14(b)) lies at $\Delta\theta/2$ and $\Delta\phi/3$ steps with respect to the center of the corresponding pixel.

Camera body supports (see fig. 2.15) ensure mechanical stability and produce a minimal unavoidable obscuration of the mirror field of view (less then 0.1 m^2).

The camera is formed by hexagonal Photonis $XP3062$[90] photomultipliers. Specific characteristics are:

1. non-uniformity of the response over the photocatode within 15%: the light spot size for an infinity distant point source is about one-third of the pixel size, so the uniformity is not a critical parameter.

2. a nominal gain $5 \times 10^4 - 10^5$.

3. spectral response: the PMT average quantum efficency is 0.25 in the wavelength range of interest.

4. linear response: it is better than 3% over a dynamic range of at least 10^4 for signals of 1 μs.

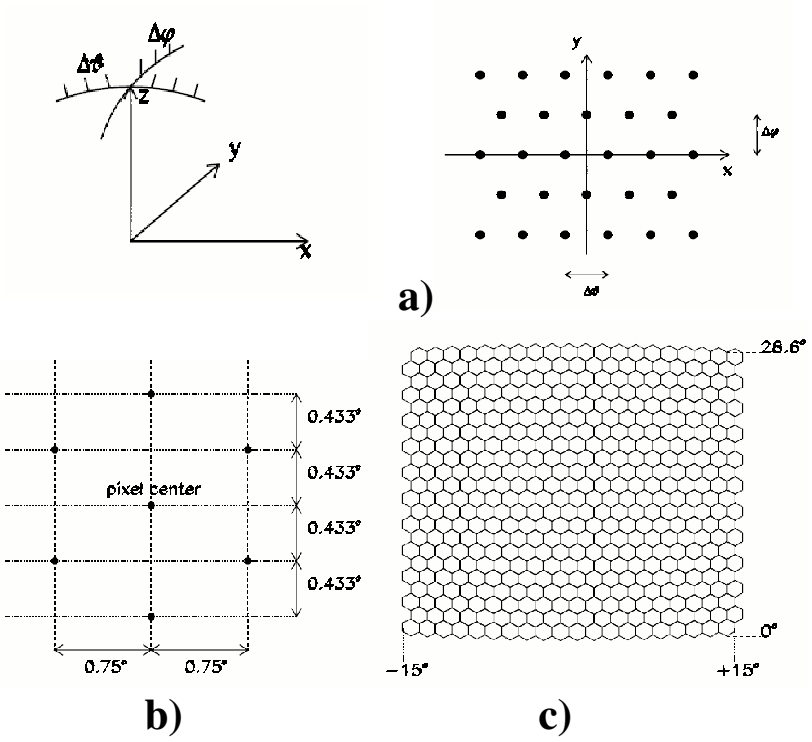

Figure 2.14: Geometrical construction of the FD camera: (a) pixel centers are placed over a spherical surface in steps of $\Delta\theta$ and $\Delta\phi$; (b) disposal of pixel vertices around the PMT center; (c) the matrix of 20×22 pixels.

5. longevity: the integrated anode charge corresponding to the half life of the tube is not less than 500 C with an half life of ~ 50 years.

6. single photoelectron: even if it is not necessary, PMT have a single photoelectron detection capability, which guarantees a good resolution for the tube.

In order to achieve a good geometrical and profile reconstruction accuracy, flash-ADC ($FADC$) to digitize collected light are used. An electronic system with a wide dynamic range and 10 MHz ADC sampling has been developed.

To maximize light collection and to guarantee a sharp transition between adjacent pixels, $PMTs$ are complemented by light collectors. The basic element of a light collector is a reflecting star named "mercedes", with three

Figure 2.15: Camera support.

arms at 120°. At each pixel vertex corresponds a mercedes, hence 6 mercedes surround each PMT (see fig. 2.16). The arm length is approximately half of the pixel side length and its section is an equilateral triangle with base 9.2 mm. In these conditions, a light collection efficency of 94% is obtained (see fig. 2.17).

2.5.2 FD Calibration

A correct reconstruction of the longitudinal profile of a shower and hence the determination of its total energy strongly depends on the conversion from ADC counts of each pixel to the photon flux produced by the shower in its field of view (light flux). Each pixel of the camera has an individual PMT with an FADC readout; the combined effect of all the detector components (including optical filter transmittance, mirror reflectivity, PMT gain and quantum efficiency, etc.) are needed to convert the FADC trace to a number of photons incident on the telescope aperture.

FD calibration is performed as *absolute* (drum, multiwavelength and roving) and *relative* calibration.

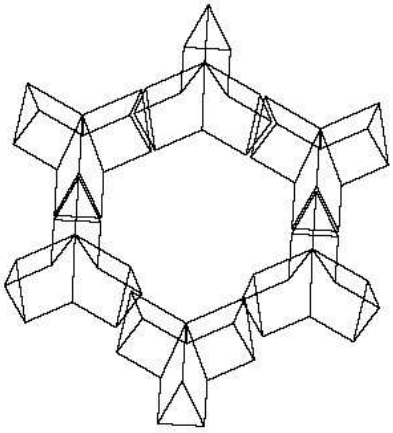

Figure 2.16: Six mercedes positioned to form a pixel. Each mercedes star has three arms at 120°.

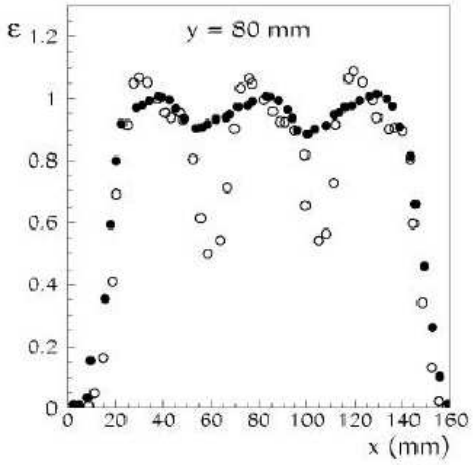

Figure 2.17: Measurement of the light collection efficency with a light spot moved along a line passed over three pixels: • measurements performed with mercedes; ∘ measurements without mercedes.

Absolute Calibration

The "absolute" calibration is performed by means of an *end-to-end*[1] technique involving a 375 *nm* light source mounted at the telescope aperture

[1] "*end-to-end*" means that in the calibration procedure all the effects due to efficiency and geometry of the detector are taken into account

to illuminate all 440 pixels simultaneously and uniformly. The light source, called the *drum*, is a cylinder 1.4 m deep with a 2.5 m diameter (see figure 2.18).

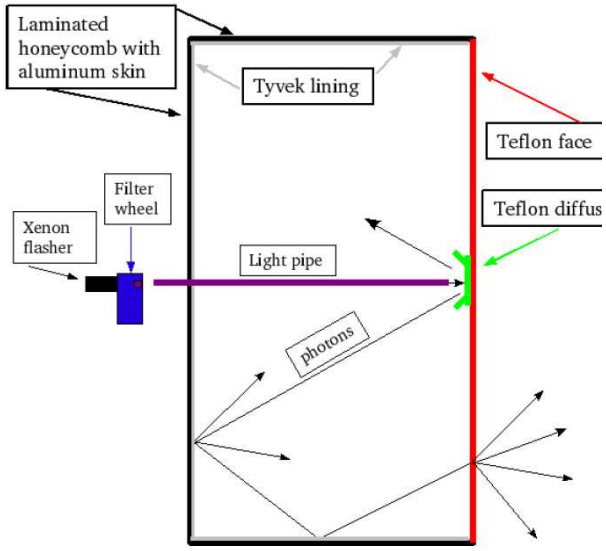

Figure 2.18: The calibration drum.

A light pipe runs from the front face to the back of the drum along the center axis. The drum is powered by UV LEDs for the absolute measurement. Where the light pipe meets the front face of the drum a Teflon diffuser directs the light to the walls and back surfaces of the drum which are lined with diffusively reflective materials. A uniform illumination of the camera is provided and the PTM response to a 375 nm light source is studied.

The response to different wavelenghts (320, 337, 355, 380 and 405 nm) is studied using a xenon flasher. Interpolation between the measured points is based on a response curve predicted from manufacture specifications. This curve is normalized to the absolute measurement made with LEDs at 375 nm.

A portable laser system (*Roving Laser*) has been set up to provide a cross check of the drum calibration. The laser is driven out into the field approximately 4 km in front of the FD buildings and fired vertically. The aerosol attenuation can be neglected at such short distances from FD buildings, and Rayleigh scattering from the molecular component of the atmosphere is known, hence the flux of photons arriving at the telescopes can be predicted

very accurately once the energy is measured by a probe. This technique has the advantage of being independent from the drum calibration and provides a cross check.

Relative calibration

To monitor changes in the response of the single and combined light detecting and light collecting optics components, a relative calibration system has been implemented (see fig. 2.19). Before and after each night of data taking, a relative calibration run is performed, to study night to night and seasonal variations.

The light from 3 different xenon flash light sources is distributed through optical fibers to the 6 telecopes of each eye, in different positions:

Cal A: the source illuminates directly the camera through a diffuser placed at the center of the mirror, to monitor the stability and linearity of the PMTs;

Cal B: the source illuminates the mirror, and the light reflected on the camera, to monitor the combined stability of the mirror reflectivity and camera gain;

Cal C: the source illuminates Tyvec targets inside the telescope doors, then the light pass through the aperture, hits the mirror and is reflected on the camera. The stability of the full telescope is monitored; 5 narrow band interference filters are used to monitor the response at wavelengths 330 nm, 350 nm, 370 nm e 410 nm.

2.5.3 FD operation : Trigger and Event Selection

FD data registration is regulated by a four levels trigger system.

The First Level Trigger (FLT) selects pixels whose signal is above a fixed threshold.

The Second Level Trigger (SLT) individuates valid "patterns" that are compatible with a cosmic ray track on the camera. The validity of a pattern is established by comparison with the five reference topologies shown in figure 2.20, and to all the topologies obtained by rotation and reflexion of the first five. A total of 108 topologies are used for the comparison, for at least 4 out of 5 pixels are required to be over threshold. This request is motivated by the possibility of traces only partially hitting a pixel of the sequence, causing its signal to be under threshold.

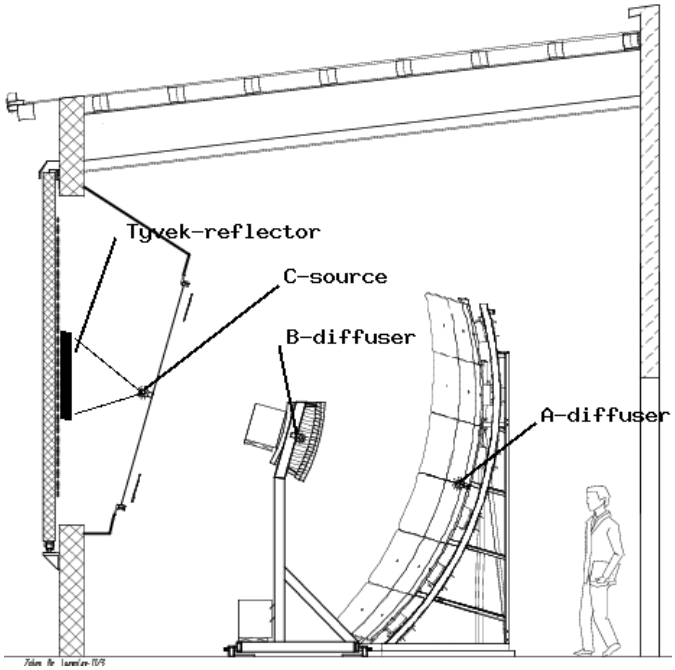

Figure 2.19: Relative calibration light sources positions.

The Third Level Trigger (TLT) is a software trigger based on track lenght and space-time requirements, in order to discard sequences generated by pixels are spacially but not temporarily correlated.

Finally a T3 trigger selects shower candidates requiring tighter space-time criteria and performs a preliminary geometrical reconstruction. Good events are identified on the basis of pixel pulse widths and times between triggered PMTs.

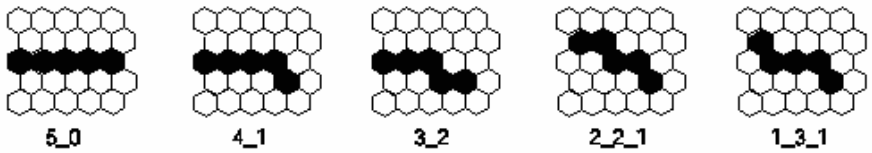

Figure 2.20: Basic valid topologies for T1 trigger level. T1 signal is generated is 4 out of 5 pixels of a sequence are over threshold.

Events passing all trigger levels are registered as fluorescence data. The FD can also drive the SD in hybrid mode: a trigger is sent to the surface array when a shower pass the T3 level. The stations can be matched in time

and position, adding important informations for the geometry reconstruction, improved by SD timing informations.

2.6 Atmospheric Monitoring System

Experiments based on fluorescence detection use the atmosphere as a huge calorimeter, whose properties vary with altitude and time. To obtain a precise estimate of the amount of the fluorescence light emitted by the cosmic ray shower, a detailed knowledge of the atmospheric conditions is required. The largest uncertaities in the fluorescence measurements comes from uncertainties in the atmospheric transmission, air Cherenkov subtraction and light multiple scattering.

In figure 2.21, the Auger map with the position of all the atmospheric monitoring devices is shown.

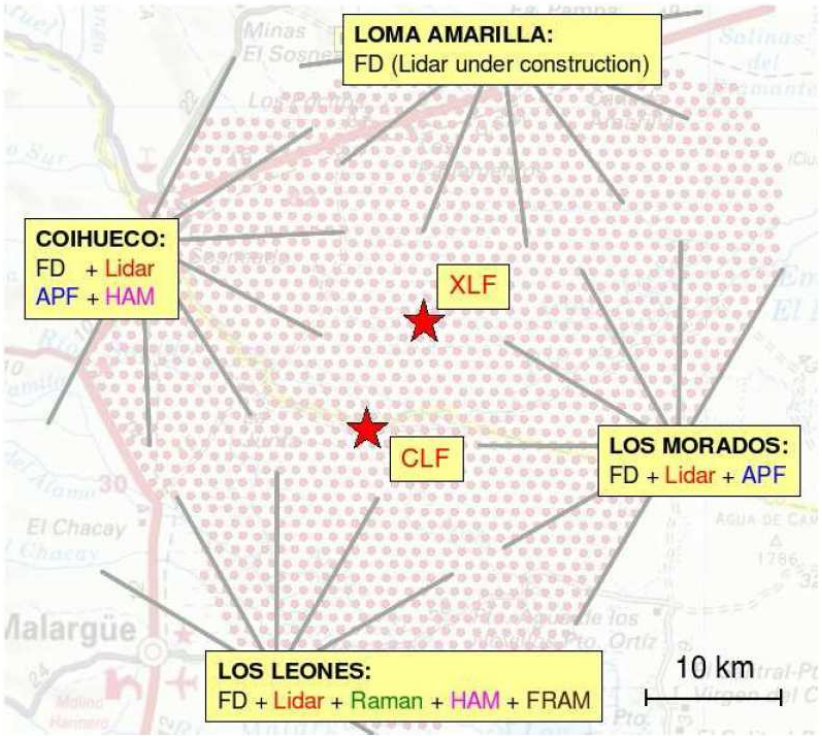

Figure 2.21: Auger South atmospheric monitoring devices

Air Density Profile: balloon launches and weather stations

In order to obtain an air density profile, essential to transform atmospheric depth to geometrical altitude and viceversa, the atmosphere is continuously investigated in campaignes with meteorological radio soundings and with measurements at ground-based weather stations, in order to describe pressure and temperature as a function of the height and time [99]. The determination of the air density profile is needed both to describe the development of the shower in height, and to take correctly into account the Rayleigh attenuation coming from the interaction of fluorescence light with atmospheric molecules.

Horizontal Attenuation Monitor (HAM)

LIDAR systems are complemented by Horizontal Attenuation Monitors (HAM), in which almost horizontal laser shots are used to measure the horizontal attenuation length between FD eyes as a function of the wavelegth. The HAM system consists of a high intensity discharge lamp, located at the Coihueco FD building, and a receiver CCD located at the Los Leones FD building, about 45 km away. The system fires a horizontal, collimated beam of light at 5 wavelengths. A filter wheel in front of the CCD allows monitoring the aerosol extinction coefficient at different wavelengths. To monitor time variations, measurements are hourly performed during FD data acquisition.

Photometric Robotic Atmospheric Monitor (FRAM)

The FRAM is the latest addition to the atmospheric monitoring instruments of the Pierre Auger Observatory. An optical telescope equipped with CCD camera and photometer, it automatically observes a set of selected standard stars and a calibrated terrestrial source. Primarily, the wavelength dependence of the attenuation is derived and the comparison between its vertical values (for stars) and horizontal values (for the terrestrial source) is made. Further, the integral vertical aerosol optical depth can be obtained. A secondary program of the instrument, the detection of optical counterparts of gamma-ray bursts, has already proven successful.

Aerosol Phase Function (APF)

$APFs$ (Aerosol Phase Function Monitors) has been designed to measure the aerosol differential scattering cross-section $d\sigma/d\Omega$, which depends on the

characteristic of the aerosols [103]. Th measurement is made firing a horizontal collimated beam of light from a xenon flash lamp across the field of view of an FD eye. Parameters are measured fitting the horizontal light tracks recorded by the FD, which contain a wide range of light scattering angles from the beam (30° to 150° in azimuth.)

Cloud Cameras

The Observatory cloud sky coverage is monitored by means of infra-red observations at wavelength between 7 and 14 μm, provided by *cloud cameras* [101] located at each eye. The CCs consist of infrared digital camera with a field of view of $45° \times 35°$, positioned on steerable mounts allowing an entire sky view. CCs generate a full picture every 15 minutes.

LIDARs

A LIDAR (Light Detection and Ranging) is present at each FD building to measure the atmospheric aerosol content by backscattered light signals [100]. LIDAR stations are instrumented with a UV laser source and three parabolic mirrors Each parabolic mirror focuses the backscattered laser light into a PMT. LIDAR systems have two main operation modes: (a) a continuos sky scan on a $\approx 50°$ cone around the local vertical; (b) "shoot the shower" mode, on a restricted sample of high energy events, laser pulses are triggered by and shoot in the region of the events.

Laser Facilities : CLF, XLF

Two laser laser facilities (Central Laser Facility, CLF [126] and eXtra Laser Facility, XLF) are located in the middle of the Pierre Auger Observatory SD array, at distances that range from 25to 40 km from FD buildings. They are equipped with UV lasers (355 nm) and optics that direct a beam of calibrated pulsed light into the sky. Light scattered from these beams produce tracks in the fluorescence detectors.

The eXtra Laser Facility (XLF) was built during 2006. Its position, marked in figure 2.21, was nearly equidistant from Coihueco, Los Morados and Loma Amarilla eyes. An accident recently happened (october 18^{th} 2007): the XLF exploded, probably due to a gas leakage. Presently possible causes are under investigation, while the design of the XLF2 is under study.

CLF laser beam can be steered to any direction with an accuracy of 0.2°. By means of an optical fiber, a fraction of the laser light can be injected into a nearby SD tank (Celeste) allowing systematic studies of hybrid geometry

recontruction accuracy. Finally the predictable intensity of light scattered from the beam at each height can be used to measure the aerosol attenuation from the beam to the FD eye; the analysis presented in this work is finalized to this purpose.

2.7 Communications in the Auger Observatory

Since the South Auger Observatory covers a wide area of 3000 km^2, the only viable solution to manage communications is by a system based on radio technology, which was included in the first Auger project design (1991).

The communication system consists of 2 integrated radio networks organized as a 2-layer hierarchy: each individual detector comunicates through the *surface detector wireless LAN (WLAN)*, which is a partitioned network supported by 4 nodes, that are serviced by a high capacity microwave backbone network (MBN).

The MBN supports all the communications regarding each SD station and each FD building. The system consists of two "arms", both terminating at the Observatory Central Campus in Malargüe, where the data are rooted to the central data acquisition system (CDAS). In fig. 2.22 the MBN design is shown.

The surface detector WLAN uses the 902-928 MHz industrial, scientific and medical (ISM) radio band, operating like a cellular telephone system, dividing the Observatory area into a number of sectors. Within each sector communications are managed by a base station.

The base station antennas serving each sector are mounted on the communications towers placed at each FD building and at the Central Campus.

2.8 The Offline Software Framework

Within the Pierre Auger Collaboration, a general purpose software Framework [95]

has been designed in order to implement algorithms and configuration instructions to build the variety of applications required by event simulation and reconstruction tasks.

The framework is flexible as well as robust to support the collaborative effort of a large number of physicists developing a variety of applications over a 20 year experimental run. It is able to handle different data formats in order

Figure 2.22: The backbone layer communication system.

to deal with events, monitoring informations and air shower simulation code outputs.

The framework is implemented in C++ and takes advantage of object oriented design and common open source tools, while keeping the user-side simple enough for C++ novice to learn in a reasonable time. Code implementation has taken place over the last two years and it is now being employed in analysis of data gathered by the observatory.

The *Offline* framework comprises three principal part:

1. a collection of processing *modules* which can be assembled and sequenced through instructions provided in an *XML* file [97];

2. an *event* structure through which modules can relate all pieces of experimental information and which accumulates all simulation and reconstruction results;

3. a *detector* description which provides a gateway to data describing the configuration and performance of the observatory as well as atmospheric conditions as a function of time.

Processing algorithms, developed by the Collaboration, can be inserted in modules, which can be put together defining an analysis *Module Sequence* by means of an *XML* file. This modular design allows to easily exchange code, compare algorithms and build up a variety of applications by combining modules in various sequences.

Cuts, parameters and configuration instructions used by modules or by the framework itself are stored in *XML* files.

The Offline is built on a collection of utilities, including a *XERCES-based* [96] parser, an error logger and a set foundation classes to represent objects such as signal traces, tabulated functions and particles. The utilities collection also provides a geometry package in which objects such as vectors and points keep track of the coordinate system in which they are represented. This allows for their abstract manipulation, as any coordinate trasformation which may be required in an operation between objects is automatically performed. The geometry package also includes support for geodetic coordinates.

The event data structure contains all raw, calibrated, reconstructed and Monte Carlo data and acts as the principale backbone for communication between modules. The event structure is built up dynamically as needed and is instrumented with functions allowing modules to interrogate the event at any point to discover its current constituents.

The detector description provides an intuitive interface from which module authors may retrieve information about the detector configuration and performance. The interface is organized following the hierarchy normally associated with the observatory instruments. Generally, static detector informations are stored in *XML* files, while time-varying monitoring and calibration data are stored in *MySQL* [98] databases. The atmosphere is treated as part of the detector. Data from atmospheric monitoring devices are stored in *MySQL* databases.

2.9 SD Reconstruction

2.9.1 Geometry Reconstruction

In the geometric reconstruction of an SD event, the observable quantities are the coordinates of the i-th station triggered, known by the GPS, and the arrival time of the incoming shower front t_i on the station, determined by the PMTs' ADC traces (see figure 2.23).

In the first phase PMTs' FADC traces of the triggered stations are used to infer the temporal window t_s of the signal and the initial time t_0. Then

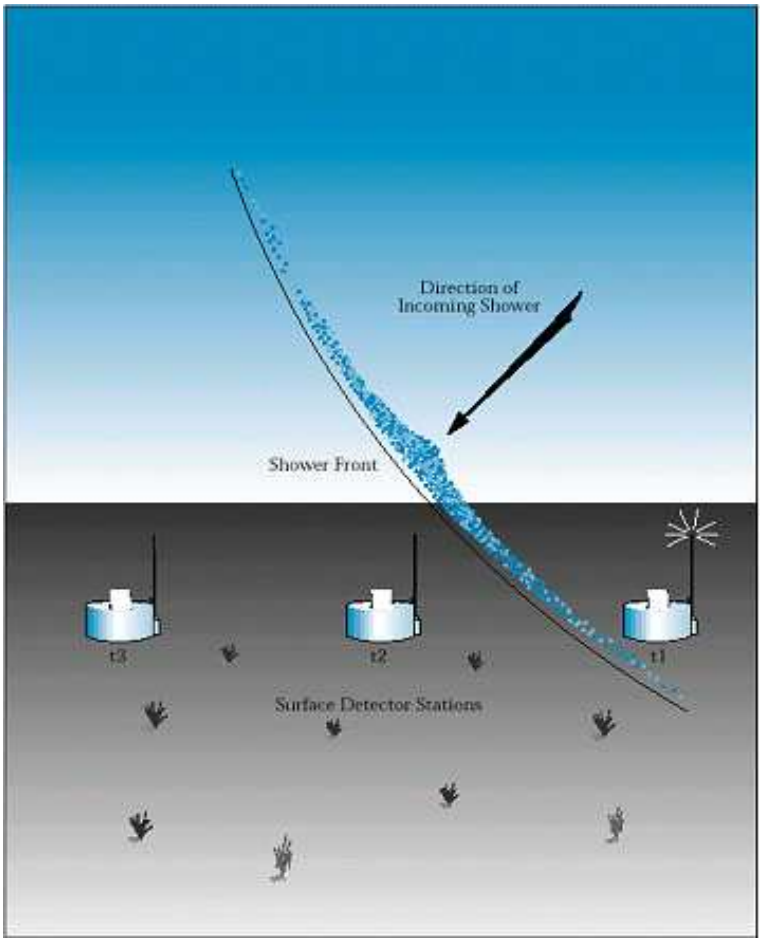

Figure 2.23: Shower front reaching SD stations: fired tanks trigger in sequence (t1 - t2 - t3).

the determination of the *core* follows: its position is inferred by the weighted average of x_i and y_i coordinates of the triggered stations, using the charge of their signal S_i as weight.

In a coodinate reference system x, y, z, where z is the vertical, *core* coordinates are:

$$x_c = \frac{\sum W_i x_i}{\sum W_i} \tag{2.1}$$

$$y_c = \frac{\sum W_i y_i}{\sum W_i} \tag{2.2}$$

with $W_i = \sqrt{(S_i)}$.

The second phase is the reconstruction of the shower axis. The direction is established on the basis of the shower front arrival times on SD stations. The shower core is the reference point and a time T_0, worked out from the weighted average of triggered tank times, as done for the core, is associated to it. For each time t, the shower front can be represented as a point $x(\vec{t})$ moving along the shower axis $\hat{a}$ at c velocity, hence:

$$x(\vec{t}) - \vec{b} = -c(t - T_0)\hat{a} \tag{2.3}$$

where the versor for the shower axis is pointing toward the source. In a flat shower front approximation, the time t at which the front passes through a point P on the ground, identified by the vector $x(\vec{t})$, is given by:

$$ct = cT_0 - (x(\vec{t}) - \vec{b}) \cdot \hat{a} \tag{2.4}$$

Assume that only errors σ_t associated with the time of triggered tanks are significative, the shower axis is estimated minimizing the relation [93]:

$$\chi^2 = \frac{1}{\sigma_t^2} \sum_i [t_i - t(x_i(\vec{t}))]^2] = \frac{1}{c^2\sigma_t^2} \sum_i [ct_i - cT_0 + \vec{x_i} \cdot \hat{a}]^2 \tag{2.5}$$

where $\vec{x_i}$, t_i and $t(x_i(\vec{t}))$ are the measured and expected position and the time for the $i-$th tank, respectively.

Let be $\hat{a} = (u, v, w)$, $\vec{x_i} = (x_i, y_i, z_i)$ and $c\sigma_t = \sigma$, eq. 2.5 becomes

$$\chi^2 = \frac{1}{\sigma^2} \sum_i [ct_i - cT_0 + x_i u + y_i v + z_i w]^2. \tag{2.6}$$

Minimizing the previous equation, it is possible to get $\hat{a} = (u, v, w)$, of course with the condition

$$u^2 + v^2 + w^2 - 1 = 0. \tag{2.7}$$

In the above minimization, the error definition plays a leading role. Since time dispersion increases going away from the core, tanks very far away could cause the failure of this procedure. The errors are usually defined as a function of the signal. One adopted solution, derived from simulation studies, is [94]

$$\sigma_i(ns) = 1800/(S_i)^{0.85} \tag{2.8}$$

where S_i is the signal recorded by the $i-$th tank. If necessary the procedure is reiterated using a parabolic approximation for the shower front [94].

2.9.2 Energy Reconstruction

The SD-only measurement of the energy of the primary particle starts from the determination of the Lateral Distribution Function (LDF). Each experiment makes use of a specific function to obtain the best LDF. The function depends on the configuration of the detector used, and it is chosen on the basis of the results obtained simulating the apparatus, studying the features of NKG function. This formula describes the transverse development of electromagnetic showers, that is dominated by Coulomb scattering of charged particles off nuclei in the atmosphere.

It was demonstrated by simulations that for the Auger South ground array spacing, at 1000 m from the shower core the dependence of the signal size $S(r)$ from statistical and first-interaction point fluctuations and from the primary nature is minimized. Therefore, the observable that best relates to the primary energy is the signal size at 1000 m ($S(1000)$).

To infer the primary energy, the lateral distribution of density of particles at ground is interpolated with the chosen function (see figure 2.24) and the value at 1000 m from the core ($S(1000)$) is extrapolated.

The function used in the Auger Experiment is [87]:

$$\mathrm{S(r)} = \mathrm{S(1000)} \left(\frac{\mathrm{r}}{1000}\right)^{-\beta} \left(\frac{\mathrm{r}+700}{1700}\right)^{-\beta}$$

where r is the distance to the shower axis in meters, $S(r)$ is the signal size at a core distance r, $S(1000)$ is the size parameter of the shower and β is called the *slope* of the LDF.

The conversion from $S(1000)$ to energy is performed by means of simulations (in this case the energy estimate is model-dependent) or by correlation with FD energy, as performed in Auger and described in section 2.11.

2.10 FD Reconstruction: mono and hybrid

The reconstruction of fluorescence events is divided in *geometrical* and *profile* reconstruction. In the geometrical reconstruction the shower track and timing informations are used to derive the shower axis. In the latter, employing shower geometry informations and signals recorded by the fluorescence detector, the shower profile is estimated.

The FD directly measures the deposited energy in the atmosphere by the electromagnetic component of a shower, which carries away more than 95% of the shower energy (it depends on the primary particle composition and energy); hence, the energy is inferred in a model-independent way. The

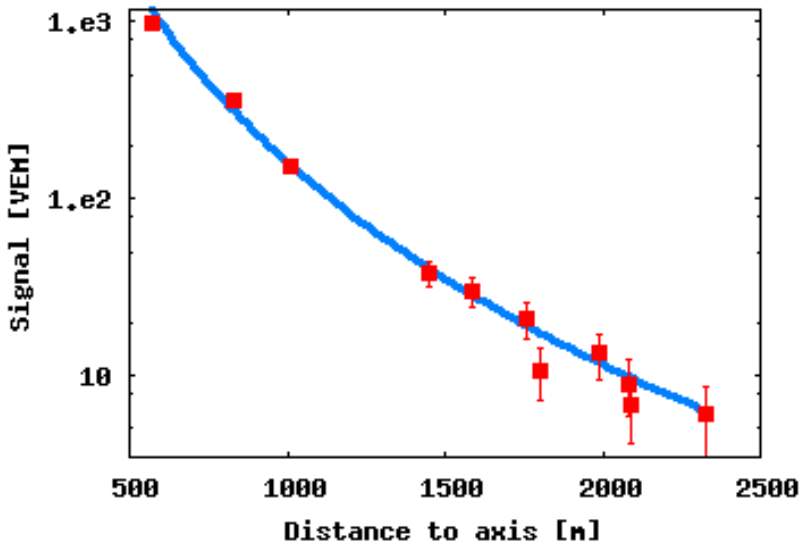

Figure 2.24: Signals of SD stations hitted by a shower as a function of the *core* distance (m). The lateral distribution is fitted with the Auger LDF.

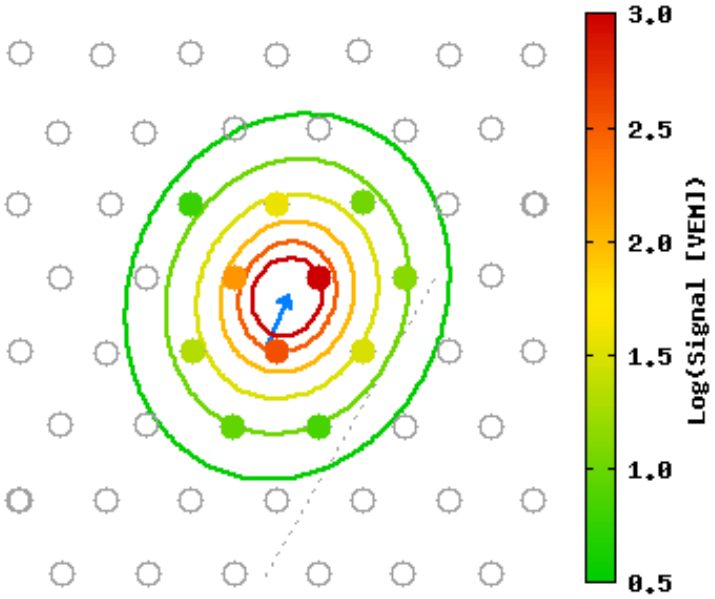

Figure 2.25: SD array view: triggered stations are emphasized by circles. Colors are used to diversify the intensity of PMT signals.

hybrid detection allows to build a corrispondence between the SD energy estimator $S(1000)$, and the energy measured by the FD: so it is possible to perform an energy calibration of the ground array. This will be discussed in details in section 2.11.

The biggest limit of the mono FD reconstruction (only one eye involved) is the geometrical step, because of large uncertainties. The hybrid design provides a solution to this problem: the ground array receives an external trigger by the FD in case of $T3$ events (see 2.5.3), and the system associates any possible tank correlated with it. Most of FD events will be hybrid event and 60% of them will involve only a few SD tanks (sub-threshold shower).

2.10.1 Geometry Reconstruction

Geometrical reconstruction is a two-steps process (see fig. 2.26):

1. the determination of the Shower Detector Plane (SDP), i.e. the plane containing the shower axis and the observation point;

2. the shower axis reconstruction, within the SDP.

The shower geometry would be completely fixed once we determine the SDP, by means of its normal versor, and the axis position and orientation within the SDP.

Shower Detector Plane Reconstruction

Since the Shower Detector Plane contains the shower axis and the observation point, the directions of those pixels receiving light from the shower should lie within the plane.

The SDP normal vector, $\vec{n}$ is found minimizing:

$$\chi^2 = \sum_i (\vec{r}_i \cdot \hat{n}) \cdot w_i \tag{2.9}$$

where $\vec{r}_i$ is pointing direction of the $i-$th PMT and w_i is a weight proportional to its signal. The sum is performed over all triggered pixels. Using SDP reconstruction, it is possible to discard triggered pixels away from the fit.

Shower Axis Reconstruction

The second reconstruction step is the determination of the shower axis within the SDP. In the mono reconstruction, it is estimated using the timing

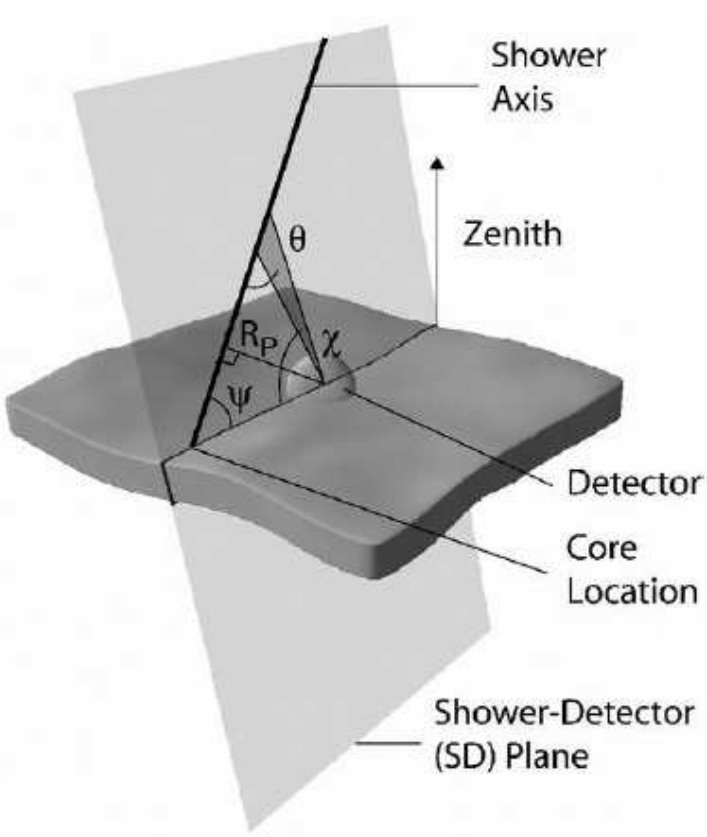

Figure 2.26: Geometry of an EAS trajectory. The Shower Detector Plane contains both the shower axis and the observation point.

information from FD signals. In the hybrid reconstruction, additional informations from the ground array can be used to improve reconstruction performances.

Mono Reconstruction

In the SDP, parameters R_P, χ_0 and T_0 are defined respectively as:

R_P **:** the minimum distance between the axis and the observation point (impact parameter);

χ_0 **:** the angle between the trajectory and the horizontal plane passing from the detector within the SDP;

T_0 **:** the time at which the shower front plane passes through the detector center.

For a graphical description, see fig. 2.26 and fig. 2.27.

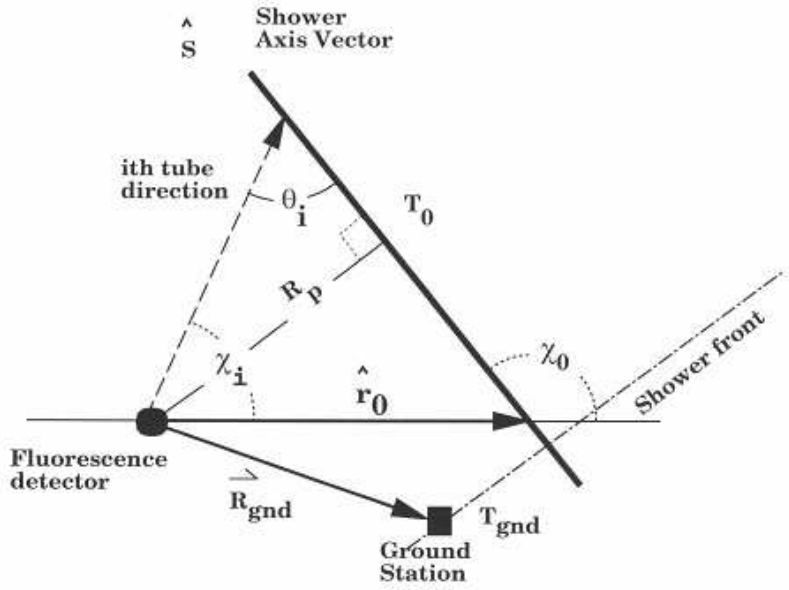

Figure 2.27: *EAS* geometry within the *SDP*. The picture includes an SD station outside the *SDP* and involved in the event.

The light reaching the PMT at time t_i from any point with viewing angle θ_i is delayed with respect to the arrival time T_0. The delay is:

$$\delta_t(\theta_i) = t_i T_0 = \frac{R_P}{c\, sin\theta_i} - \frac{R_P}{c\, tan\theta_i} = \frac{R_P tan(\theta_i/2)}{c} \tag{2.10}$$

where c is the speed of light, t_i is the $i-$th tube trigger time and θ_i is related to χ_0 by

$$\theta_i = \chi_0 - \chi_i \tag{2.11}$$

where χ_i is the tube elevation angle in the plane (see fig. 2.27).
The set of axis parameters (R_p, χ_0, T_0) is determined minimizing:

$$\chi^2 = \sum_i w_i (t_i - t_{th})^2 \tag{2.12}$$

where t_i is the $i-$th tube time, w_i is a weight proportional to its signal and t_{th} is

$$t_{th} = T_0 + \frac{R_p}{c} \tan\Big(\frac{\chi_0 - \chi_i}{2}\Big). \tag{2.13}$$

Presently t_i is defined as the time of the center of signal of the $i-$th PMT. Fig. 2.28 shows a time fit example.

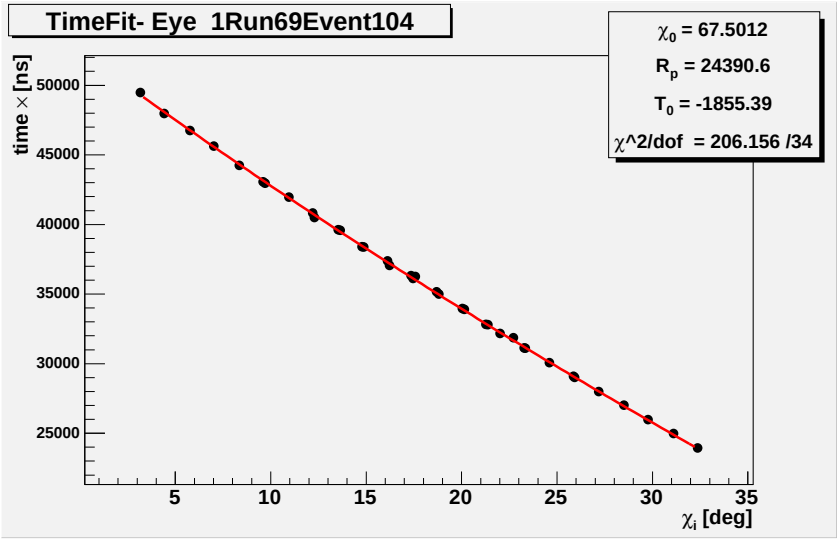

Figure 2.28: Time fit example: experimental points superimposed to the fit result.

Hybrid Reconstruction

Since the ground array is going to be completed, most of FD events could be reconstructed using SD information to improve the time fit performance. The expected arrival time t_k of the shower front at the $k-$th tank as a function of axis parameters is

$$t_k = T_0 + \frac{\vec{R}_{gnd,k} \cdot \hat{S}}{c} \tag{2.14}$$

where $\vec{R}_{gnd,k}$ is the vector from the eye to the SD tank k and $\hat{S}$ is the shower axis versor. So, axis parameters could be derived minimizing

$$\chi^2 = \chi^2_{FD} + \chi^2_{SD} \tag{2.15}$$

using terms from FD and SD data. An accurate knowledge of FD-SD time offset is mandatory. Currently it is measured by means of laser shots of known energy and geometry.

The timing information coming from the SD introduce new terms in the function with a different dependence on parameters.

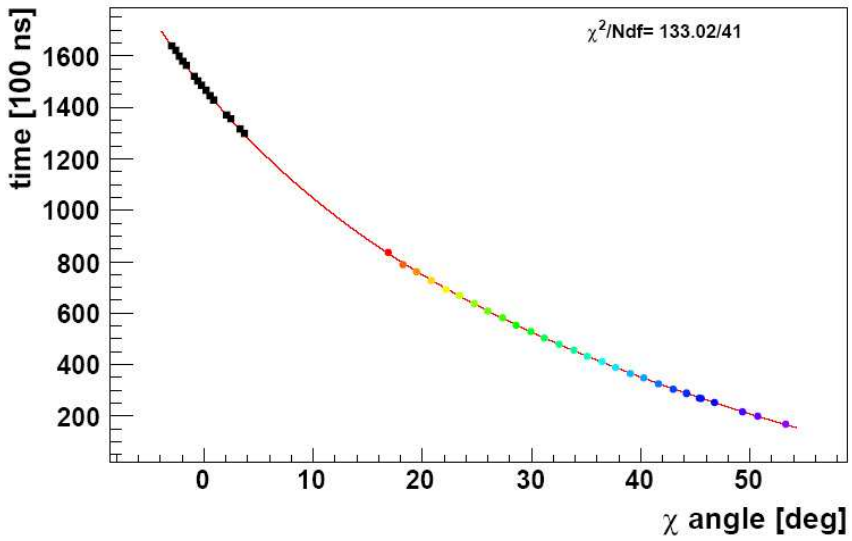

Figure 2.29: Hybrid Time fit example: experimental points from SD and FD superimposed to the hybrid fit result.

In fig. 2.29 an example of hybrid time fit is presented. An evident improvement with respect to the mono fit is shown: the stability of the mono reconstruction fit is based upon the capability to determine the curvature of the time-fit distribution.

In figure 2.30 the FD mono vs hybrid geometry reconstruction uncertainty is shown. For the mono reconstruction, not only the uncertainties in R_p and χ_0 are larger, but they are also strongly correlated. Using the timing information of the tanks the degeneracy in the FD mono geometry reconstruction is broken and the reconstruction is greatly improved.

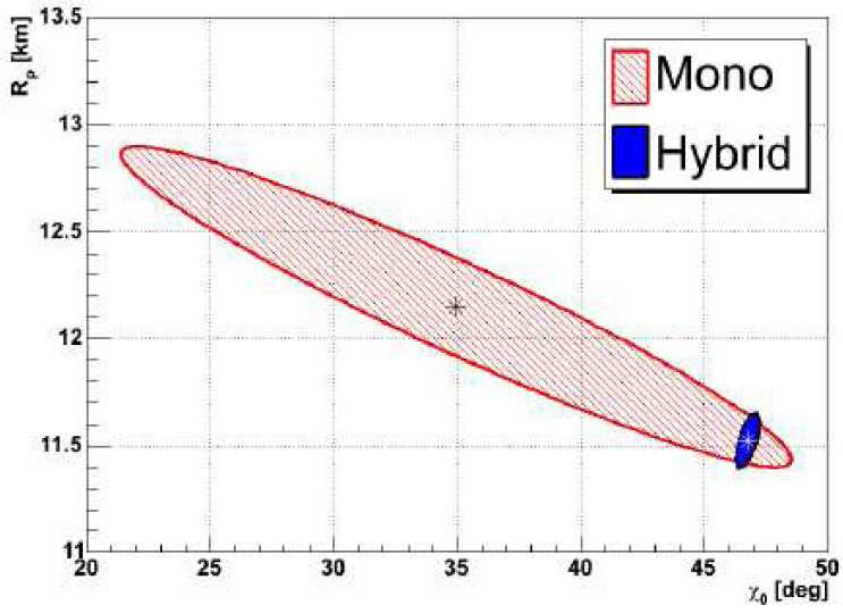

Figure 2.30: FD mono reconstruction uncertainty (red) versus hybrid uncertainty (blue).

2.10.2 Longitudinal Profile and Energy Reconstruction

In order to extract physical information from recorded data, once the shower geometry has been reconstructed, it is possible to determine the shower longitudinal development. This procedure consists of 3 steps:

1. **Determination of the light profile**, i.e. the number of photons reaching the aperture of the detector as a function of $FADC$ time bins. For each time bin t_i, the expected direction the fluorescence light is coming from is given by the vector $\vec{R}_i$ pointing from the eye to the shower axis. This direction forms an angle χ_i with the horizontal plane within the SDP, that is calculated inverting eq. 2.10

$$\chi_i = \chi_0 - 2\tan\Big(\frac{c}{R_p}(t_i - T_0)\Big) \tag{2.16}$$

   Then the total charge recorded by FD telescopes is computed, summing the charge over all (triggered and not) pixels whose angle between their pointing directions and $\vec{R}_i$ is lower than a value ζ. The value of the parameter ζ is dynamically computed, event by event, maximizing the

signal to noise ratio over all the light profile. The result is the determination of the light profile reaching the detector as a function of time (see fig. 2.31).

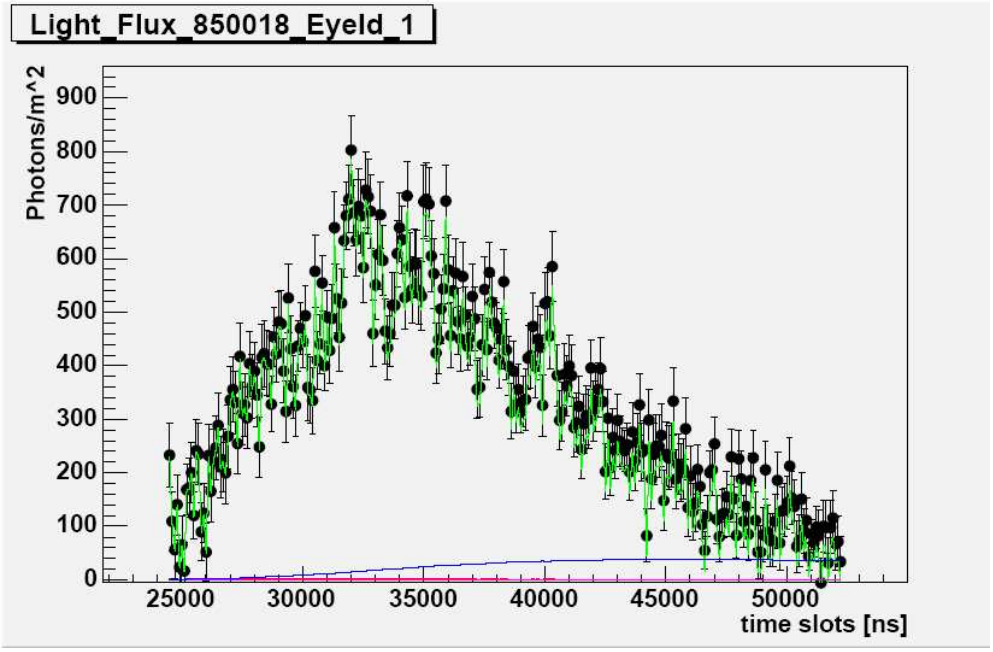

Figure 2.31: Light profile reaching the detector as a function of time

2. **Light at track back-propagation**. Starting from the computed light flux at diaphragm, photons are back-propagated through the atmosphere to their production point along the shower trajectory. At this stage the atmospheric attenuation suffered by light in its travel from source to the detector is taken into account. The number of photons as a function of the traversed slant depth are calculated (i.e., photons at trace).

3. **Longitudinal Profile Reconstruction**. The reconstruction of the longitudinal profile (figure 2.32) is performed using directly the ionization energy deposit of shower particles in the atmosphere, proportional to the number of fluorescence photons produced, in contrast with the typically considered shower size profile. With this approach, the calorimetric shower energy is directly given by the integral of the energy deposit profile. An analytic least-square solution for the estimation of the profile has been developed, in which both fluorescence and Cherenkov

lights are treated as signal [117], while in the standard approach the Cherenkov contribution is subtracted in an iterative way. This method allows to avoid rejection of events with a large Cherenkov contamination, once experimental systematic uncertainties are well understood.

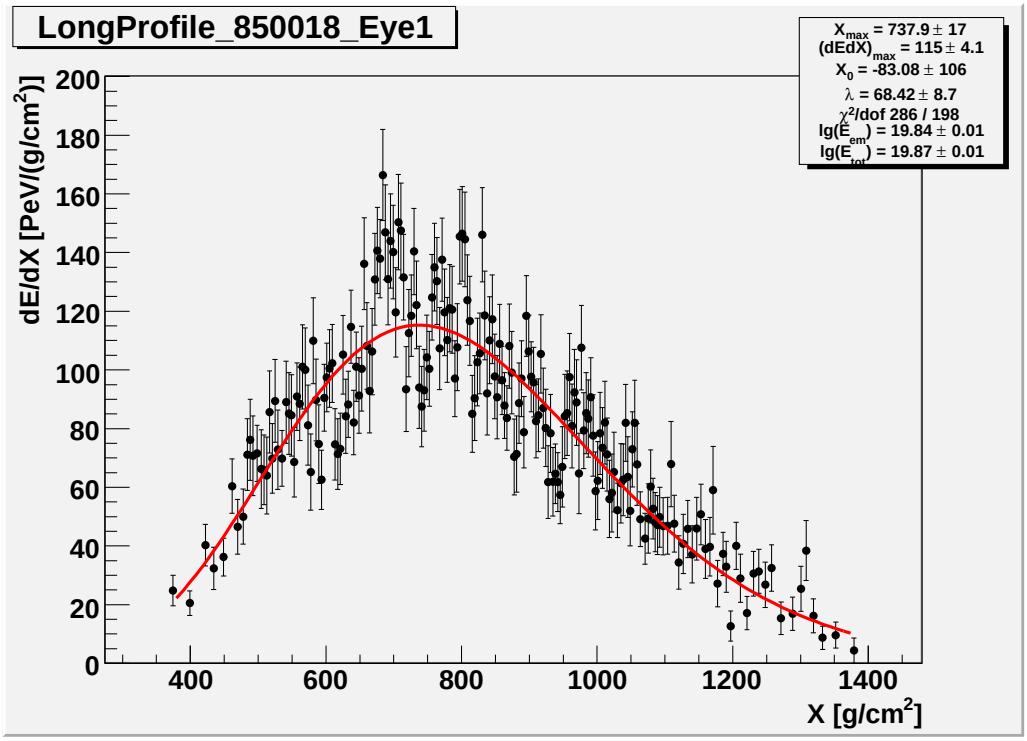

Figure 2.32: Energy deposit as a function of the atmospheric slant depth

FD Energy Estimation

Once the longitudinal profile is reconstructed, the energy of the electromagnetic component of a shower can be directly calculated by integrating the energy deposit profile:

$$E_{em} = \int_{X_1}^{\infty} \frac{dE}{dX}(E)dX \tag{2.17}$$

To infer the shower total energy E, it is possible to use a parametrization [104] for the unseen energy in terms of E_{em} in EeV units:

$$\frac{E}{E_{em}} = \frac{1}{0.958 - 0.048 E_{em}^{-0.162}} \tag{2.18}$$

obtained for proton primaries with QGSJET model with a zenith angle of 45°. This correction introduces a 5% energy uncertainty. It is clearly not applicable to a case of a pure electromagnetic shower, because its profile is not described by a Gaisser-Hillas parametrization as well as the one coming from an hadronic shower.

2.11 SD-FD calibration

As seen in the sec. 2.9.2, the FD calorimetric energy measurement is almost model-independent, the systematic uncertainty introduced by the unseen energy correction is only at level of 5%. For ground-based experiments, the energy calibration is performed using simulation results and hence it relies on the assumption of the high energy hadronic interaction model. For example, estimating the energy of AGASA events near 100 EeV using either protons and the SIBYLL model, or iron nuclei with the QGSJET01 model, leads to a energy ratio of 1.33. Hence, hybrid data, which represent a 10% of the total, can be used to calibrate the Auger surface array, exploiting the hybrid nature of the detector. The resulting cosmic ray flux is then almost independent from shower models or composition assumptions.

As already said in section 2.9.2, the energy estimator for SD events is S(1000). The stage of the shower development represented by S(1000), at ground, depends on zenith angle θ. The function that describes the dependence of S(1000) from θ is called the attenuation curve; it provides the conversion from S(1000) at a given depth (i.e. for a shower with zenith angle θ) to the equivalent S(1000) to a reference depth (i.e. with a reference zenith angle). The reference depth adopted by the Auger Collaboration corresponds to a zenith angle $\theta = 38°$ (1142 g/cm^2), which corresponds to the average of the zenith angle distribution of real events. The equivalent signal, and then the SD energy estimator, is indicated as S_{38}. The *attenuation curve* is empirically obtained using the Constant Intensity Cut (CIC) method (introduced by the MIT group [105], its application to the Auger data is described in [61]). This method assumes an isotropic distribution of the cosmic radiation and hence the independence of the integral flux from the zenith angle above a certain energy. Then, SD events are calibrated appling the correlation curve of log(S_{38}) vs log(FD energy) for hybrid events which can be reconstructed by both SD and FD apparatus and satisfies strict criteria [61]. In fig. 2.11 the calibration curve is shown. At the last ICRC in Mérida, México

2007, the Auger Collaboration presented a calibration curve with 357 hybrids events collected up to 28 February 2007. The limited statistics leads to an uncertainty in the energy scale due to the calibration curve of 18% [61].

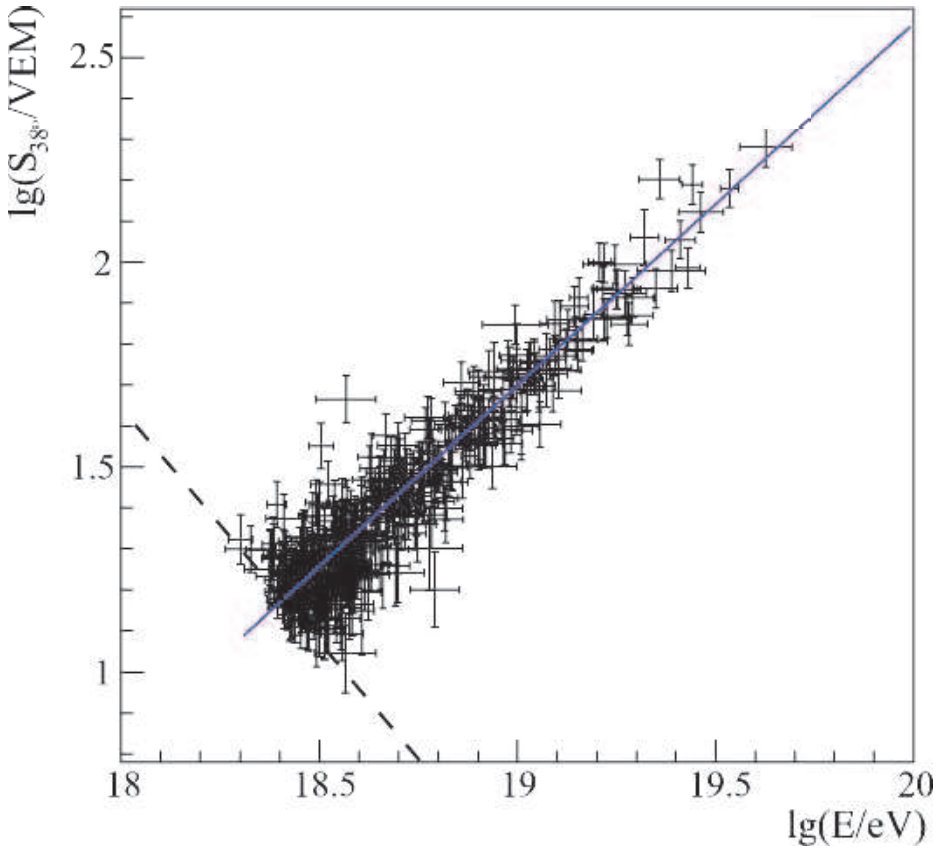

Figure 2.33: Calibration curve for 357 hybrid events with simultaneous measurement of $S_{38}(1000)$ and FD energy (taken from [61]).

Table 2.1 summarizes the systematic uncertainties affecting the FD energy determination. These uncertainties, summed in quadrature produce a total indetermination of 22% [106]. The main terms contributing to the total uncertainty are the fluorescence yield (14%), the absolute calibration (9.5%) and the reconstruction (10%). Efforts to reduce these main terms are underway; results from the AirFly experiment [107] are expected.

	uncertainty %
Fluorescence Yield	14
Detector Calibration	9.5
P,T, and humidity effectes on yield	7
Atmosphere (attenuation)	4
Missing Energy	5
Reconstruction	10
Total	22

Table 2.1: Current estimates of the systematic uncertainties affecting energy reconstruction. Values are extracted from [106].

The first 4-fold event of the Auger Observatory

A schematic view of the first four-fold event is shown in fig 2.34. It was detected on May 21^{th} 2007, from all four FD eyes together with the SD array. The event, coming at a zenith angle $\sim 65°$, has a reconstructed energy of $\sim 10^{19}\ eV$, a X_{max} of $790 g/cm^2$ [108].

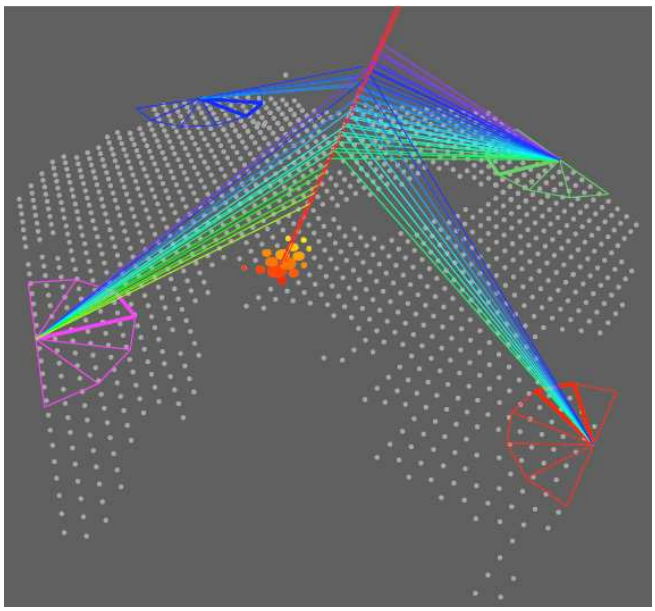

Figure 2.34: Schematic view of the event of May 21^{th} 2007.

Chapter 3

Atmospheric Transparency Measurements at the Pierre Auger Observatory

3.1 Introduction

In the Pierre Auger Experiment, the fluorescence technique to detect *EAS* makes use of the atmosphere as a huge calorimeter, whose properties must be continuously monitored to ensure a reliable energy estimate. Several instruments are presently working at the Observatory site to provide the atmospheric informations needed (see section 2.6).

The fluorescence light emitted during the development of a shower is scattered and attenuated by the atmosphere in its travel towards the FD buildings. Light extinction in atmosphere is mainly due to:

- molecular scattering, divided in elastic Rayleigh and anelastic Raman scattering;
- elastic aerosol Mie scattering;
- atmospheric absorption (mainly due to ozone).

Both molecules and aerosols in the atmosphere predominantly scatter, rather than absorb, fluorescence photons. Some absorption does occur (due to ozone and because the single scatter albedo of the aerosols is typically slightly less than unity) but these effects are small. In the following, the term "attenuation" is used to indicate photons that are scattered in such a way that they do not contribute to the light signal recorded by FD.

All attenuation processes are usually described in terms of atmospheric transmission coefficients ($T^{\lambda}_{mol}(s)$, $T^{\lambda}_{aer}(s)$ and $T^{\lambda}_{abs}(s)$), indicating the fraction of transmitted light intensity as a function of the wavelength λ and of the distance s. An accurate measurement of the transmission factors during data acquisition allows to obtain the needed corrections to infer the primary energy, starting from the intensity of the light detected. Two out of the three factors, T_{abs} and T_{mol}, are measurable once density, temperature and pressure of the atmosphere are known. The third factor, T_{aer}, depends on the aerosol distribution $n_{aer}(r, s)$ in dimension (r) and height (s), that is a highly variable component and can change significantly in a short time.

3.2 Atmospheric Attenuation Processes

Main fluorescence light extinction processes are the molecular Rayleigh elastic scattering and the aerosol Mie elastic scattering. The photon absorption mechanism due to atmospheric gas is negligible: the associated transmission factor T_{abs} is nearly 1 in the wavelength interval of the fluorescence light. Moreover, in the molecular processes, Raman anelastic cross section is 3 orders of magnitude smaller than the Rayleigh elastic one, hence it can be neglected in the total calculation of the molecular transmission coefficient $T^{\lambda}_{mol}(s)$.

3.2.1 Rayleigh Scattering

Fluorescence photons interact in the atmosphere with air molecules (mainly nitrogen, in a smaller fraction oxigen), suffering an elastic scattering process known as *Rayleigh scattering*. The amount of light scattered out of a beam composed by N_{γ} photons is [50]:

$$\frac{dN_{\gamma}}{dl} = -\rho \frac{N_{\gamma}}{x_R} \left(\frac{400}{\lambda}\right)^4 \tag{3.1}$$

where ρ is the molecular air density, λ is the wavelength of the scattered light and x_R is the mean free path, equal to 2874 g/cm^2, as reported by Bucholtz [109].

Assuming an isoterm description of the atmosphere, ρ can be approximated to:

$$\rho = \rho_0 e^{-h/H_0} \tag{3.2}$$

where ρ_0 is the air density as estimated at the experiment site.

Taking into account the angular distribution estimated for the Rayleigh scattering, the total amount of light diffused by this process is:

$$\frac{d^2N_\gamma}{dld\Omega} = \frac{dN_\gamma}{dl}\frac{3}{16\pi}(1 + cos^2\theta) \tag{3.3}$$

3.2.2 Mie Scattering

The 98% of the atmosphere is composed by N_2 and O_2 molecules: the remaining 2% is made by minor gas components and by particles suspended in air (dust, liquid droplets, etc.) named *aerosol*. Their radius typically ranges from 0.1μm to 10μm; hence they are much larger than N_2 (r = 1.8 Å) and O_2 (r = 1.7 Å) molecules.

Aerosols show a complex dynamic behaviour, due to the influence of gravity and of the motion of neighbour molecules, besides the inner variability of their physical and chemical properties, depending on the process by which they were created (volcanic eruptions, air pollution, etc.). The aerosols property to interact with electromagnetic waves strongly depends on their shape, dimensions and chemical composition.

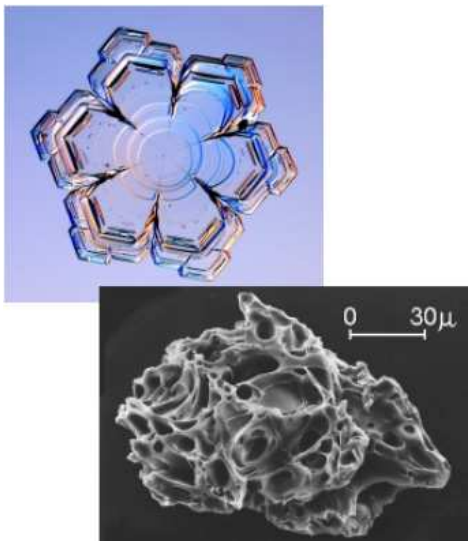

Figure 3.1: Examples of aerosols.

The Mie scattering is the aerosol elastic diffusion of the light, where aerosol dimensions are of the order of magnitude of the incident light wavelength. The main difficulty occurring in the evaluation of the amount of light

diffused by this process lies in the aerosol density distribution, a strongly variable parameter (see section 3.3.2).

The amount of fluorescence light diffused out of a beam of N_γ photons due to Mie scattering is [50]:

$$\frac{dN_\gamma}{dl} = -\frac{N_\gamma}{L_{mie}} e^{-h/H_{mie}} \tag{3.4}$$

where L_{mie} is the Aerosol Horizontal Attenuation Length at FD buildings height ($z = 0$ corresponds to 1412 m a.s.l.), while H_{mie} is the Scale Height factor that describes the rapidity of extinction of aerosols with growing heigths. The angular distribution is strongly peaked in the forward direction, but not as much as for the Cherenkov light. Approximately, for angles between 5° and 60° the amount of light diffused is given by:

$$\frac{d^2N_\gamma}{dld\Omega} \approx \frac{dN_\gamma}{dl} 0.80 e^{-\theta/\theta_M} \tag{3.5}$$

where $\theta_M \approx 26.7°$.

3.3 The Atmospheric Transparency

The fluorescence light collected by a single pixel of the FD telescopes is described by the equation:

$$I_{FD}(s) = \int_{\Delta\lambda} I^\lambda(s)\eta(\lambda)QE(\lambda)d\lambda \tag{3.6}$$

where:

s **:** distance between the telescope and the source of the fluorescence light along the line of sight;

$I_{FD}(s)$ **:** light intensity detected by a single FD pixel;

$\Delta\lambda$ **:** fluorescence light spectrum (300-420 nm);

$I^\lambda(s)$ **:** fluorescence light intensity detected by the FD mirror;

$\eta(\lambda)$ **:** FD optical transmission efficiency;

$QE(\lambda)$ **:** PMT quantum efficiency.

The amount of fluorescence light collected at the FD aperture $[I^\lambda(s)]$ is proportional to the light intensity at the source $[I_0^\lambda(s)]$:

$$I^\lambda(s) = I_0^\lambda(s) T_{mol}^\lambda(s) T_{aer}^\lambda(s)(1+f)\frac{d\Omega}{4\pi} \tag{3.7}$$

where:

$I_0^\lambda(s)$ **:** fluorescence light intensity at height z, where $z = s \times sin(\theta)$, and θ is the elevation angle of the FD line of sight;

$T_{mol}^\lambda(s)$ molecular Rayleigh trasmission coefficient at λ;

$T_{aer}^\lambda(s)$ aerosol transmission coefficient;

f higher order corrections, due to multiple scatterings;

$d\Omega$ solid angle to the FD.

To measure the intensity of fluorescence light emitted by the shower in the FD field of view $I_0^\lambda(s)$ (photons at trace, see section 2.10.2), needed to estimate the primary energy, the two trasmission factors T_{mol} and T_{aer} must be determined.

The Rayleigh contribution T_{mol} is well understood and can be evaluated once the molecular density profile is known [99]. The evaluation of the Mie contribution T_{aer} needs continuous monitoring of the atmospheric conditions.

3.3.1 Molecular Transmission Factor : T_{mol}

The molecular transmission factor $\mathrm{T}_{mol}^\lambda(\mathrm{s})$ is funcion of the total Rayleigh cross section and of the atmospheric molecular density:

$$T_{mol}^\lambda(s) = exp\left(-\int_0^s \sigma_{mol}^\lambda n_{mol}(s) ds\right) \tag{3.8}$$

The molecular density profile $n_{mol}(s)$ depends on the range along the line of sight s, while the cross section σ_{mol}^λ depends on the wavelength following a $(1/\lambda)^4$ law, according to equation 3.1.

Once temperature and pressure as a function of the height are known, the molecular density profile $\mathrm{n}_{mol}(\mathrm{z})$ is obtained applying the Ideal Gas Law:

$$P(z) \cdot V = N \cdot K_B \cdot T(z)$$

and hence:

$$\frac{N}{V} = n_{mol}(z) = \frac{P(z)}{K_B \cdot T(z)}$$

where z is the height and not the range along the light of sight.

Radio Soundings and Weather Stations at the Auger Observatory

The atmospheric molecular density profile $n_{mol}(s)$ is continuously monitored [99]. A detailed study of the temperature, density and pressure properties of the atmosphere, together with wind speed and direction above the Auger South Observatory is systematically operated. Since august 2002, meteorological radio soundings have been performed in several campaigns near Malargüe. The radiosondes are launched above the site of the experiment on helium-filled balloons (see fig. 3.2). A set of data is taken about every 20 m during ascent up to 25 km a.s.l. in average. Ground-based weather stations record temperature, pressure, relative humidity, and wind data every 5 min. The results of these measurements have been parametrized and organized in monthly profiles, named Malargüe Monthly Models, which are employed in the simulation and reconstruction of showers.

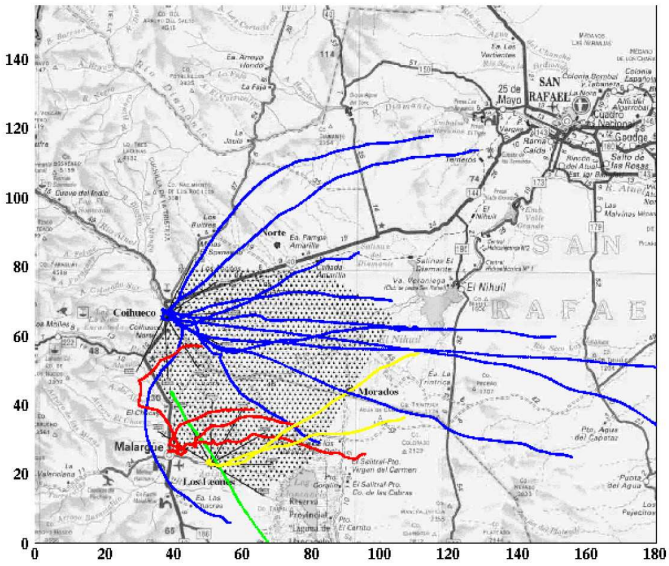

Figure 3.2: Tracks of a subset of balloon launches.

3.3.2 Aerosol Transmission Factor : T_{aer}

The aerosol transmission factor is :

$$T^{\lambda}_{aer}(s) = \exp\left(-\int_0^s \left[\int_0^{\infty} dr \pi r^2 Q_{ext}(r, m, \lambda) n_{aer}(s, r)\right] ds\right) \qquad (3.9)$$

It is the most complex of the transmission factors, because of its dependence on $n_{aer}(s, r)$, i.e. the *aerosol Size Distribution* (SZD), that indicates

the number of aerosol per cm^3, in the range along the line of sight s, with radius between r and $r + dr$ (assuming a spherical shape).

The probability of interaction between fluorescence photons with wavelength λ and aerosols with radius r and refraction index m is described by the product of the extinction efficiency factor $Q_{ext}(r,m,\lambda)$ with the aerosol geometrical section πr^2.

Assuming an horizontally uniform aerosol distribution, $T^{\lambda}_{aer}(s)$ can be defined as a function of the aerosol extinction coefficient $\alpha_{aer}(z)$ from the ground to a point at altitude h observed at an elevation angle ψ:

$$T^{\lambda}_{aer}(h) = \exp\left(-\int_0^h \alpha_{aer}(z)dz/\sin\psi\right) \tag{3.10}$$

Introducing the Vertical Aerosol Optical Depth $VAOD_{aer}(h)$, that is the integral of the aerosol extinction $\alpha_{aer}(z)$ from the ground to a point at altitude h, $T^{\lambda}_{aer}(s)$ can be defined as:

$$T^{\lambda}_{aer}(h) = \exp\left[-(VAOD(h)/\sin\psi)\right] \tag{3.11}$$

The transmission factor $T^{\lambda}_{aer}(s)$ may be fully characterized by three independent measurements: the height profile of the Vertical Aerosol Optical Depth VAOD(z), its wavelength dependence, and the normalized aerosol differential scattering cross section, or phase function, $P(\theta)$.

Devices for the Atmospheric Aerosol Monitoring

Since aerosols can change significantly in the course of a few hours, they are systematically measured at all FD sites, and the parameters most important for shower reconstruction are recorded hourly.

The optical depth is measured by two distinct systems: the Central Laser Facility (CLF), which provide the FDs with calibrated laser shots and the backscatter LIDARs, which are independent telescopes operating at every FD site. Aerosol scattering is directly measured by Aerosol Phase Function monitors (APFs) at two out of the four FD locations; and the wavelength dependence of the optical depth is measured by a Horizontal Attenuation Monitor (HAM) and the robotic astronomical telescope FRAM. A detailed description of all these devices follows.

VAOD wavelength dependence (HAM - FRAM)

A commonly used parameterization of VAOD dependence on the wavelength is a power law expression by Ångstrøm [110]:

$$\mathrm{VAOD}(\lambda) = \mathrm{VAOD}(\lambda_0) \left(\frac{\lambda_0}{\lambda}\right)^{\gamma} \tag{3.12}$$

where γ is known as the Ångstrøm coefficient, and $\lambda_0 = 355$ nm, approximately in the center of the nitrogen fluorescence spectrum. At the Pierre Auger Observatory, observations of γ are performed by two instruments: the Horizontal Attenuation Monitor, or HAM and the Photometric Robotic Telescope for Astronomical Monitoring, or FRAM.

The HAM consists of a high intensity discharge lamp located at Coihueco, observed by a CCD camera placed 45 km away, at Los Leones. Using a filter wheel, the CCD records the aerosol extinction coefficient, and hence the aerosol optical depth between the two sites, at five different wavelengths (365, 404, 436 and 542 nm). The average Ångstrøm coefficient observed by the HAM between July 2006 and February 2007 is $\gamma = 0.7 \pm 0.5$.

The FRAM is an independent and fully robotic system that performs photometric calibrations of the night sky at several UV and optical wavelengths. Located at Los Leones, FRAM uses a 20 cm telescope and a photometer to observe the sky [113]. The system is capable of many types of astronomical measurements [114], but its primary nightly function is to observe a set of standard stars and the HAM light source at Coihueco. From these observations it can obtain estimates of atmospheric extinction and the extinction wavelength dependence. FRAM performs hourly automatic observations of the HAM light source and several standard stars, recording the photon flux in the photometer at five wavelengths. Using clear night data, these instrumental magnitudes can be converted into total optical depths [113]; the aerosol optical depth is obtained by subtracting an estimate of the molecular optical depth for that hour. Finally, the Ångstrøm exponent is determined by fitting the wavelength dependence of the optical depth. The average exponent observed by FRAM between June 2006 and March 2007 is -0.1 ± 0.9, in agreement with the HAM observations and theoretical expectations ($\gamma \sim 0$) for a desert atmosphere [115].

VAOD phase function (APF)

Aerosols not only attenuate light from air showers, but also scatter Cherenkov light into the FD field of view, contaminating the fluorescence signal and affecting estimates of shower energy. To properly account for Cherenkov contamination, the scattering properties of the atmosphere must be well understood.

Figure 3.3: The FRAM.

Aerosol scattering depends on the physical properties of the particles in the atmosphere: as already said in section 3.2.2, the distribution of light scattered by aerosols is very strongly peaked in the forward direction, reaches a minimum near 90°, and has a small backscattering component. The scattering probability as a function of scattering angle θ is reasonably approximated by the parameterization:

$$P(\theta) = \frac{1-g^2}{4\pi} \cdot \left(\frac{1}{(1+g^2-2gcos\theta)^{3/2}} + f\frac{3cos^2\theta - 1}{2(1+g^2)^{3/2}} \right) \tag{3.13}$$

where the two terms correspond to the forward and backward scattering peaks, respectively. In this expression, g $=<$ cosθ $>$ measures the asymmetry of scattering, and f determines the relative strength of forward and backward scattering. The parameters f and g are observable quantities affected by local aerosol characteristics.

Proper estimation of light scattering from $P(\theta)$ given in eq. 3.13 requires the determination of parameters f and g. These quantities are measured by Aerosol Phase Function monitors (APFs) located several km from the FDs at Coihueco and Los Morados [111]. Using a collimated xenon flash lamp, each APF fires an hourly sequence of 350 nm shots horizontally across the FD field of view, covering 30° to 150° in azimuth. The scattering parameters f and g can be determined simply by fitting the horizontal light track recorded by the FD.

Ten months of APF measurements at Coihueco have yielded a site average of $g = 0.59 \pm 0.08$ for the local asymmetry parameter, excluding clear nights

when g = 0. The distribution of g is comparable to measurements reported in the literature for similar climates [112].

Aerosol Optical Depth : LIDAR and CLF

Two instruments are presently operational to measure the Vertical Aerosol Optical Depth: the CLF and the LIDARs (LIght Detection and Ranging) [100].

Since the atmospheric aerosol determination described in this work is performed on laser data produced with the CLF, a detailed description of the system is given in the next section.

Three out of the four elastic backscatter LIDAR stations, one at each fluorescence site, are already operational. The Loma Amarilla station is currently under construction. At each LIDAR station, a high-repetition UV laser sends short laser light pulses into the atmosphere in the direction of interest. The backscattered signal is detected by photomultipliers positioned at the focus of the three parabolic mirrors. Both the laser and the mirrors are mounted on a steering frame that allows the LIDAR to cover the full azimuth and elevation of the sky.

During each hour of FD data taking, the four LIDARs perform a routine scan of the sky over each FD . The data provide information about the height and coverage of clouds as well as their depth and opacity, and the local aerosol scattering and absorption properties of the atmosphere. In addition to this routine operation, the LIDAR system is used for real time monitoring of the atmospheric homogeneity between the FDs and selected cosmic ray events. For example, if a high energy hybrid event is observed with the SD and one or more FDs, the routine scan is interrupted and, within 2 to 4 minutes from the event detection, the LIDAR scans the atmosphere in the nearby of the air shower reported by the FD. This procedure is called *"shoot-the-shower"* (StS), and allows for a rejection of events where the light profile from the track is distorted by clouds or other aerosol nonuniformities that are not well characterized by the average hourly aerosol measurements. Both light reflection and opacity can distort the light profile.

At each FD, the local LIDARs provide the aerosol scattering coefficient, $\alpha_{aer}(h)$. The integral of $\alpha_{aer}(h)$ from the FD height to h gives the vertical aerosol optical depth, VAOD(h) , which determines the transmission loss of light from each segment of the cosmic ray track to the FD. A method to obtain VAOD(h) from LIDAR scans is described in detail in [116].

In addition to operating the elastic backscatter LIDARs, the Pierre Auger

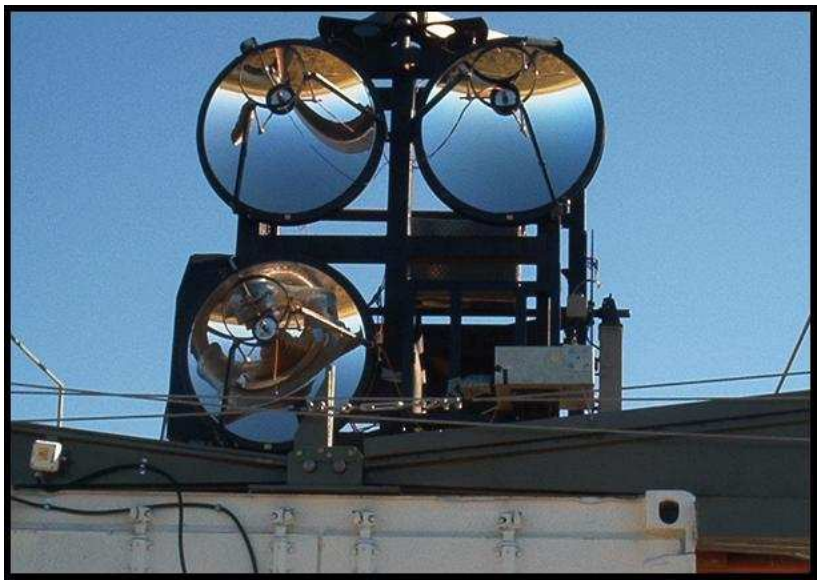

Figure 3.4: LIDAR station mirrors.

Collaboration is currently also testing a *Raman LIDAR*, which is operating in conjunction with the Los Leones elastic LIDAR. The Raman technique is based on molecular inelastic Raman scattering; the inelastic component is suppressed compared to elastic Rayleigh scattering since the Raman scattering cross-section is about three orders of magnitude smaller than the corresponding Rayleigh cross-section. In Raman scattering, the scattered photon suffers a frequency shift that is characteristic of the irradiated molecule.

Los Leones LIDAR station receiver has three channels to detect the light intensity at various wavelengths: one channel collects the elastic LIDAR return, while the other two correspond to the atmospheric oxygen and nitrogen Raman LIDAR backscatter, at about 375 nm and 387 nm, respectively. In principle, the Raman LIDAR technique has the advantage of avoiding the assumption on the so called LIDAR ratio (the ratio between aerosol backscatter and extinction), needed in the elastic channel [100], making use of the O_2 and N_2 channels. A practical disadvantage of the Raman LIDAR technique is the small Raman molecular cross-section. As a consequence, the laser source has to be operated at high power and interference with FD operation must be avoided. Currently, Raman LIDAR runs at the Pierre Auger Observatory

are only performed before and after the FD nightly data acquisition.

Aerosol Description in the Auger Offline Software

The implementation of the aerosol parameters into the Auger Offline software is designed dividing the observatory area into 5 regions (*slices*, see fig. 3.5) centered on the atmospheric monitoring devices: one for each Lidar stations, and one more central region associated to the Central Laser Facility site. Horizontal uniformity of the aerosol concentration is assumed in each slice, which is divided in vertical layers. The Auger aerosol database is filled in steps of 200 m starting from the ground up to the maximum height analyzable. Heights are referred to the sea level.

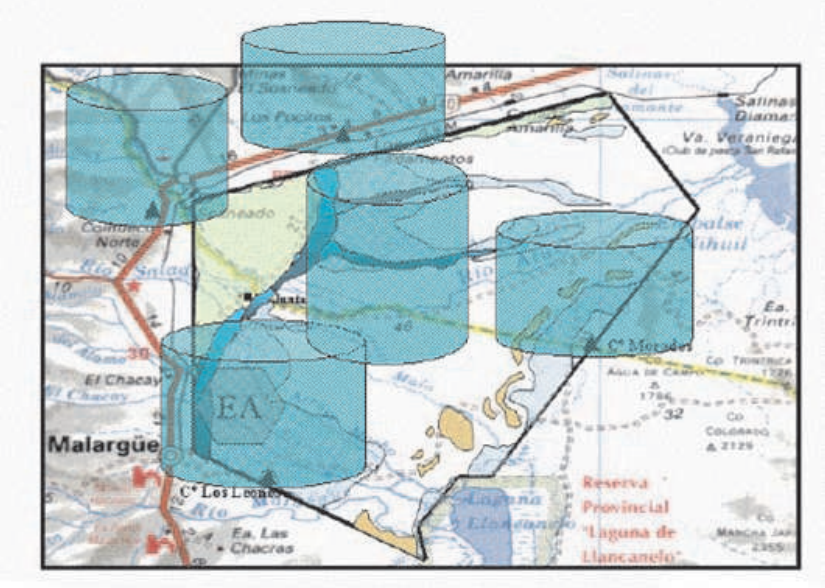

Figure 3.5: The five slices.

3.4 The Central Laser Facility

The Central Laser Facility is located approximately equidistant from three of the four FD eyes, approximately 26 km away from Los Leones and 30 km away from Coihueco and Los Morados eyes. It produces a calibrated test beam at 355 nm, near the middle of the nitrogen fluorescence spectrum; in

particular, the wavelength of the light emitted from the CLF is between the two major N fluorescence bands at 337 nm and 357 nm. When the laser is firing at its maximum power, the amount of light scattered out of each 7 ns laser pulse is roughly equivalent to the amount of fluorescence light emitted by an air shower with energy in the range of the predicted Greisen-Zatsepin-Kuzmin (GZK) suppression ($\sim 10^{20} eV$).

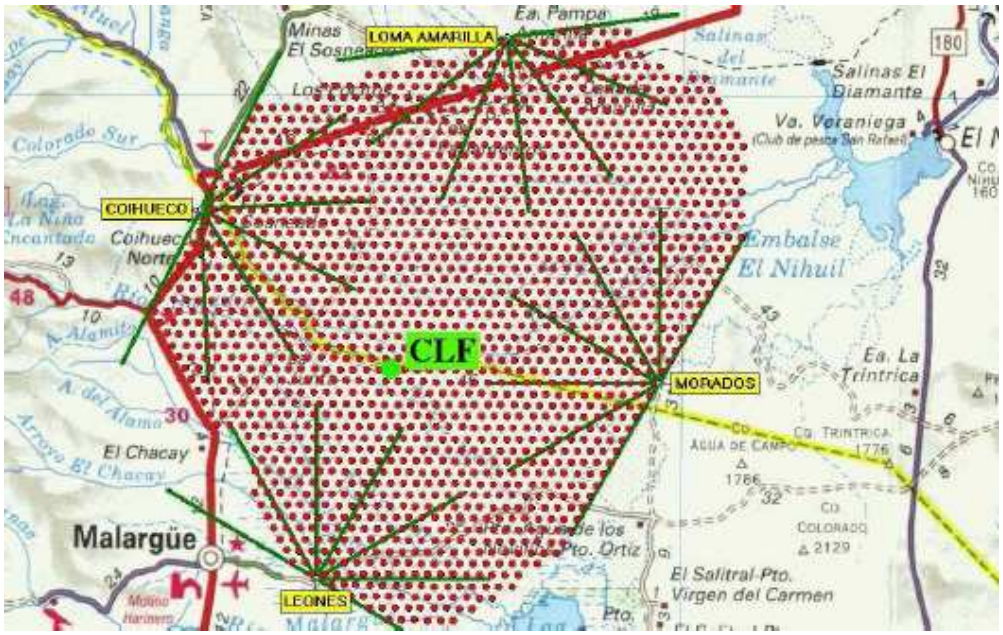

Figure 3.6: The location of CLF shown in the schematic layout of the Pierre Auger Southern Observatory

As a pulse of laser light travels through the atmosphere, the molecular and aerosol components in the atmosphere scatter light out of the beam; the atmosphere scatters nearly equal amounts of light towards each FD building, as the fluorescence light emitted by a shower, and this scattered light produces tracks in the FD. Hence, the analysis of the amount of CLF light that reaches the FD building can be used to infer the aerosol concentration.

3.4.1 Research Goals of the Central Laser Facility

Originally conceived of as part of the extensive effort to monitor the atmosphere over the observatory, the CLF can also provide an on-demand, steerable test beam for the fluorescence detector. When the FD is in operation, the laser tracks provide an ongoing confirmation that the FD eyes are

functioning and able to detect light from the center of the array. Other uses for the laser at the CLF include:

Atmospheric Monitoring: vertical laser shots are used to derive the atmospheric clarity. The longitudinal profiles of vertical tracks recorded by the FD eyes are grouped together by hour and fit to generate a database of aerosol optical depth. For the fitting, the laser profiles are normalized to the expected profile for a very clear (aerosol-free night). Currently, CLF shots are used to obtain the aerosol measurements that are a vital part of reconstructing the FD shower data. A vertical CLF track will be simultaneously visible from up to four separate FD locations at the perimeter of the surface array. Thus, differences in the amount of light observed by the FD eyes can be used to monitor the horizontal uniformity of the atmosphere across the aperture of the fluorescence detector.

Photometric Calibration the energy of each laser track is determined from the FD data using the same method employed for air showers. The reconstruction process includes correcting the raw data for both detector gain and atmopheric transmission. As mentioned previously, the energy of individual laser shots is measured by at least one independent probe (two probes in the case of vertical shots). By comparing the measured and reconstructed laser energy for a variety of pointing directions and atmospheric conditions, the end-to-end photometric resolution of the FD eyes can be cross-checked. Since the laser is fired every 15 minutes when the FD is operating, CLF data can be used to classify viewing conditions. During the periods when the laser energy is reconstructed accurately, the measured air shower energies can also be considered to be reliable.

Time Synchonization vertical tracks from the CLF can be seen by all FD eyes; therefore, these tracks can be used to monitor the relative timing of the eyes. Furthermore, laser shots that divert part of the light into the optical fiber to the Celeste tank produce event triggers in both the FD and the SD [120]. The timing of these shots is set outside of the 300 - 311 μs predetermined veto window so that the data from both detectors will be combined into a single event. The recorded event times can then be used to measure and monitor the relative timing of the two detectors. To maximize the precision of the relative timing measurements, laser shots are fired 2% above the horizontal and directly over one FD eye to synchronize that eye with the SD. The measurement is then repeated

for each of the eyes. To prevent damage to the fluorescence detectors, the 2% attenuator filter is used when taking this nearly-horizontal data.

Geometric Reconstruction both the ground position and the pointing direction of the laser beam are known to high precision. As such, laser shots can be used to tune the software that performs the geometric reconstruction of FD tracks. Laser shots that are fired simultaneously into the sky and the Celeste tank can also be used to compare the angular resolution and the core position resolution of the hybrid data with the FD-only data.

Pixel Pointing the CLF can be used to check the pointing direction of the FD eyes. The direction of each telescope is determined by monitoring the path of stars that are moving across the borders of adjacent pixels. This calibration can then be cross-checked using the laser beam. Additionally, the laser tracks provide a simple means for checking whether the FD cameras have been correctly cabled and configured. Swapped cables in a FD camera will result in a discontinuity in the laser track when viewed through the FD event display.

Trigger Efficiency by using the CLF to generate a steerable test beam, the efficiency of the FD trigger can be evaluated as a function of laser energy, pointing direction and atmospheric quality. The efficiency for a given set of conditions can be determined by taking the ratio of the number of shots recorded by a given FD eye to the number of shots fired by the CLF.

The Central Laser Facility has been functioning as an important component within the Pierre Auger Observatory since September 2003 [121, 122]. Calibration data have been collected regularly since November 2003 whenever the fluorescence detectors are operating. Controlled remotely from the Central Campus, the CLF fires both steered and fixed vertical laser shots providing a wide range of calibration purposes [123].

3.4.2 CLF hardware description

The CLF is an independent system, with no externally wired connections, that is housed within an insulated shipping container (figure 3.7). The facility is powered by a bank of batteries that is charged by an array of photovoltaic solar panels. The thirteen solar panels generate a maximum power of 885W. A propane heater keeps the inside of the container at a temperature above

Figure 3.7: The Central Laser Facility

10° C. The CLF is an unstaffed facility; it is operated remotely via a wireless microwave internet link to the Coihueco FD Eye.

The heart of the system is a frequency tripled Nd::YAG laser, manufactured by Big Sky Laser Technologies, which produces a linearly polarized beam of 355 nm light. A depolarizing element is used to randomize the polarization by introducing a varying phaseshift across the beam spot. After passing through the depolarizer, the net polarization of the laser beam is within 3% of random. The beam is pulsed, with a width of 7 ns, and a maximum energy per pulse of about 7 mJ. The laser head is mounted on an enclosed optical table that also houses most of the other optical components. An electric heater protects the laser head from freezing, in the event that the main propane heater fails. In addition to the 355 nm light, the output from the laser head contains light from the first two harmonics. To remove these unwanted components, the beam optics include two harmonic separator mirrors that reflect only the desired 355 nm component while transmitting residual light at the primary and seconday wavelengths. Downstream of these mirrors, the spectral purity of the beam is better than 99.9%. After this purication, a portion of the beam is diverted into a photo-diode detector ("probe1"), that measures the relative energy of each laser pulse.

The beam optics are congured in two vertical paths, with a computer-

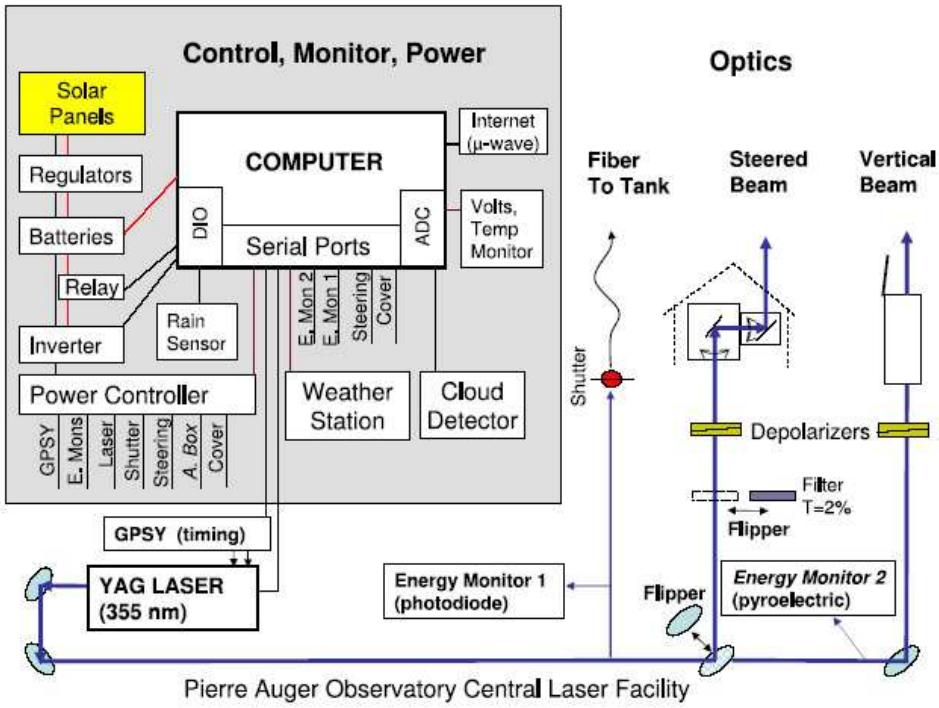

Figure 3.8: Schematic diagram of the CLF hardware.

controlled flipper mirror selecting between them (see fig. 3.8). If this mirror is flipped out of the beamline, the light passes directly to the sky when a simple cover is open. A pyroelectric energy probe ("probe2"), installed in March 2005, makes a second measurement of the relative energy when the beam is sent down this path. Approximately 8% of the beam intensity is diverted into the probe for this measurement. If the flipper mirror is rotated into the beamline, the light is sent to a steering head mounted on the roof of the facility. The steering head consists of two mirrors on rotating orthogonal axes, which can direct the beam towards any direction above the horizon. The steering head is housed within a mechanical cover that protects it from the elements when it is not in use. A second flipper mirror can rotate a 2% filter into the path of the steered beam. This filter is used to make low-energy laser pulses that can be fired almost horizontally towards the FD eyes for precision synchronization of clocks.

An optical fiber runs from the CLF to the nearest SD tank, Celeste (see

Figure 3.9: The Celeste tank near the Central Laser Facility

fig. 3.9). When a shutter, mounted on the optical table, is opened, a small fraction of the laser light is sent through this forty meter fiber and injected into the tank. This procedure provides a simultaneous signal in both the SD and the FD, for the purpose of monitoring the relative timing between the two detectors.

3.4.3 CLF vertical tracks recorded by FD

The Central Laser Facility fires 50 vertical shots every 15 minutes during Fluorescence Detector acquisition. The light scattered out of the CLF laser beam produces tracks that are recorded by the FDs, as the fluorescence light produced in the development of extensive air showers. A specific timing is used to distinguish laser from shower events; the CLF fires at specific times that have a fixed offset from the start of the second as defined by the Global Position System (GPS).

A typical vertical CLF laser track, as seen by bay4 of Los Leones eye, is shown in fig. 3.10 (left). A few additional shaded pixels, outside of the main track, were probably triggered either by multiple photon scattering or an upward statistical fluctuation in the backgrounds and noise. Flash ADC traces for the five dotted pixels are shown in figure 3.10 (right).

The light profile for a vertical CLF laser event is shown in figure 3.11. This figure displays the photon intensity at the telescope aperture as a function of time. Laser light arriving later was scattered higher in the atmosphere; it has travelled a greater distance before reaching the telescope and has been attenuated to a lower intensity.

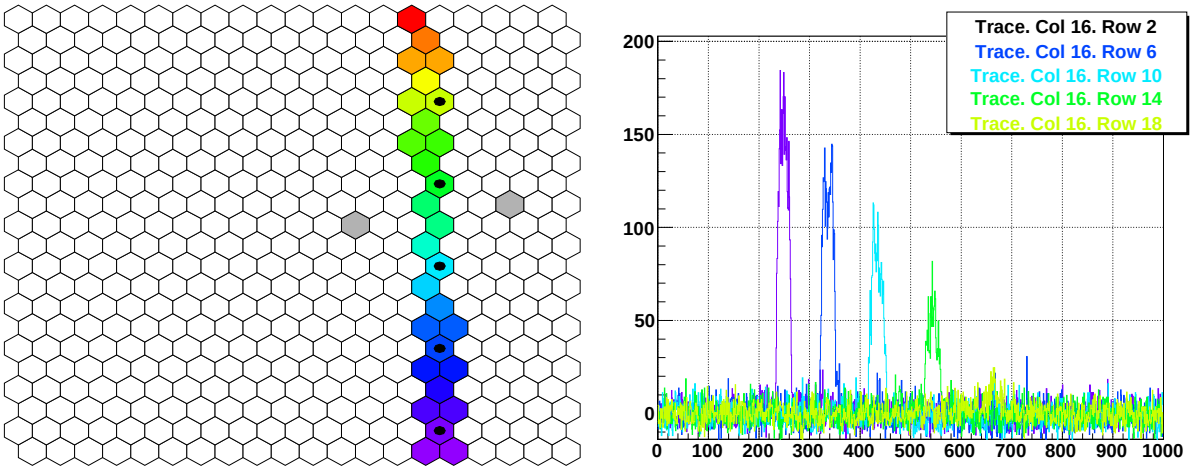

Figure 3.10: Left: A typical vertical CLF track as recorded by Bay4 in Los Leones. Right: the flash ADC traces are shown for the dotted pixels.

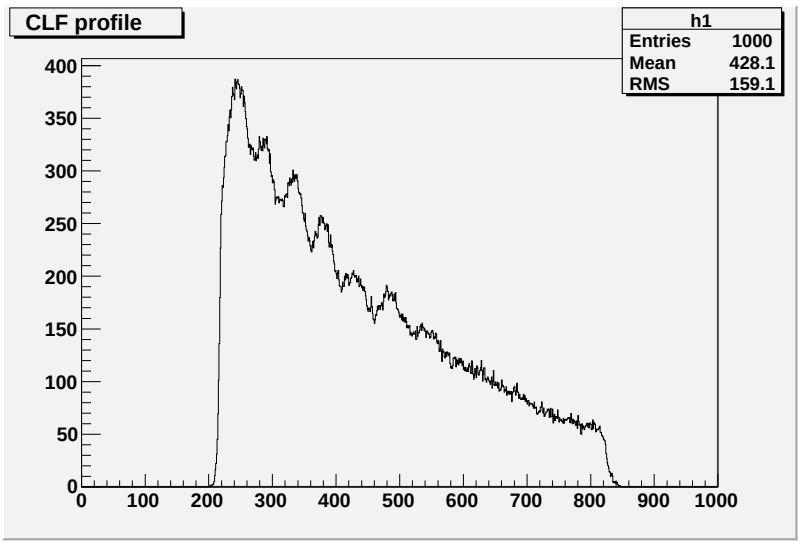

Figure 3.11: CLF profile at the telescope aperture: photon intensity as a function of time.

3.5 CLF-based Aerosol Determination Methods

Among the many measurements provided by the CLF test beams are hourly observations of $\alpha_{aer}(h)$ and VAOD(h). The atmospheric attenuation due to aerosol can be inferred measuring the amount of light collected by the

FD telescopes of CLF vertical laser tracks, whose energy and geometry are known. Two methods based on this idea have been developed in the Auger Experiment: in the following I will briefly describe the procedure developed by the Utah group, known as *"Data Normalized Method"*. This method provides the values for the aerosol attenuation presently in use in the Offline Aerosol Database for data analysis. In the next chapter the method I developed, named *"Laser Simulation Method"*, will be described in details.

Data Normalized Method for the determination of the Aerosol Concentration

As already said, the CLF fires sets of 50 vertical shots every quarter-hour, so the number of photons observed at the telescopes aperture can be averaged to obtain an hourly light profile $N_{obs}(h)$ (i.e. number of photons at the aperture as a function of height).

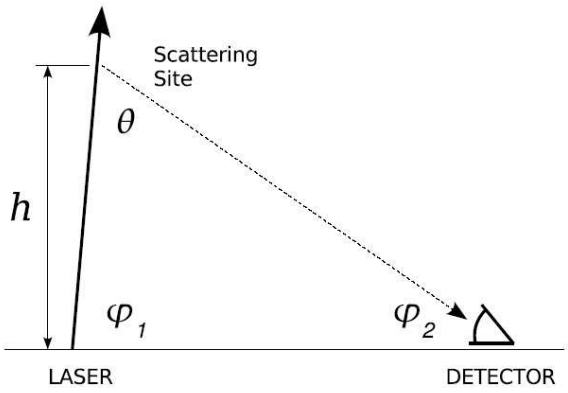

Figure 3.12: Schematization of the CLF - FD geometry.

Assuming that the horizontal uniformity for the atmosphere, it can be shown that the aerosol optical depth is [118]:

$$\mathrm{VAOD(h)} = -\frac{\sin\phi_1 \sin\phi_2}{\sin\phi_1 + \sin\phi_2}\left[\ln\left(\frac{\mathrm{N_{obs}(h)}}{\mathrm{N_{mol}(h)}}\right) - \ln\left(1 + \frac{\mathrm{P_a}(\pi-\theta)}{\mathrm{P_m}(\pi-\theta)}\right)\right] \quad (3.14)$$

where $N_{mol}(h)$ is the number of photons expected on a completely clear night (the so called Rayleigh night, when molecular attenuation only is present) and $P_a(\theta)$ and $P_m(\theta)$ are the fractions of photons scattered by aerosols and molecules, respectively. For nearly all scattering angles except for very forward directions, $P_a(\theta)$ is small compared to $P_m(\theta)$, so the

second term in eq. 3.14 can be neglected. Therefore, for vertical laser shots ($\phi_1 = \pi/2$), eq. 3.14 reduces to:

$$\mathrm{VAOD(h)} = -\left(\ln \mathrm{N_{obs}(h)} - \ln \mathrm{N_{mol}(h)}\right)\left(1 + \frac{\sin\phi_2}{1+\sin\phi_2}\right) \tag{3.15}$$

With these simplifications, the CLF optical depth measurement depends only on the elevation angle of each laser track segment and on the Rayleigh night reference profile $N_{mol}(h)$. Using measurements recorded on Rayleigh nights, the hourly CLF observations can be properly normalized without the need for absolute photometric calibrations of the FD or laser; and the aerosol optical depth may be calculated directly from 3.15.

This analysis returns an average VAOD(h) = 0.03 at the reference altitude of 4.5 km (3 km above the detector), with uncertainties of ± 0.008. The uncertainties in each VAOD(h) measurement are dominated by systematic effects due to the FD and laser relative calibrations and the choice of aerosol-free reference nights, with an additional small contribution from statistical fluctuations in the hourly average light profiles. The CLF can also detect clouds, which appear as sharp steps in the VAOD(h) profile. When a cloud is present, the lowest base height h_{base} is recorded, and $\alpha_{aer}(h)$ and VAOD(h) are considered valid up to h_{base} for air shower analysis.

Chapter 4

Aerosol characterization using the Laser Simulation method

4.1 Introduction

In this chapter I will describe in details the *"Laser Simulation Method"* set up and implemented during my PhD to determine the aerosol concentration at the Pierre Auger Observatory. The light emitted by the Central Laser Facility, randomly polarized and hence isotropically diffused towards each FD building, is scattered and attenuated by the molecular and aerosol components in the atmosphere in the travel towards FD buildings exactly as the fluorescence light emitted by a shower. The analysis of the amount of CLF light that reaches each FD building can be used to infer the aerosol concentration; the *"Laser Simulation Method"* is a procedure based on the comparison of CLF laser light profiles (photons collected at the aperture of the FD building as a function of ADC time bins) with that obtained by a grid of simulated profiles in different parametrized atmospheric conditions.

4.2 Laser Simulation in the Offline

The procedure developed makes use of a set of simulations of laser events, hence a detailed description of the detector and of the atmosphere is needed. At the time of the development of the method the detector simulation was not implemented in the Auger official software (Offline); the FDSim code [119] was the only available source for simulations.

The FDSim code has been used for some time for this analysis, after I made the needed updates with respect to the original version: the old description of the Rayleigh scattering was renewed, taking into account the

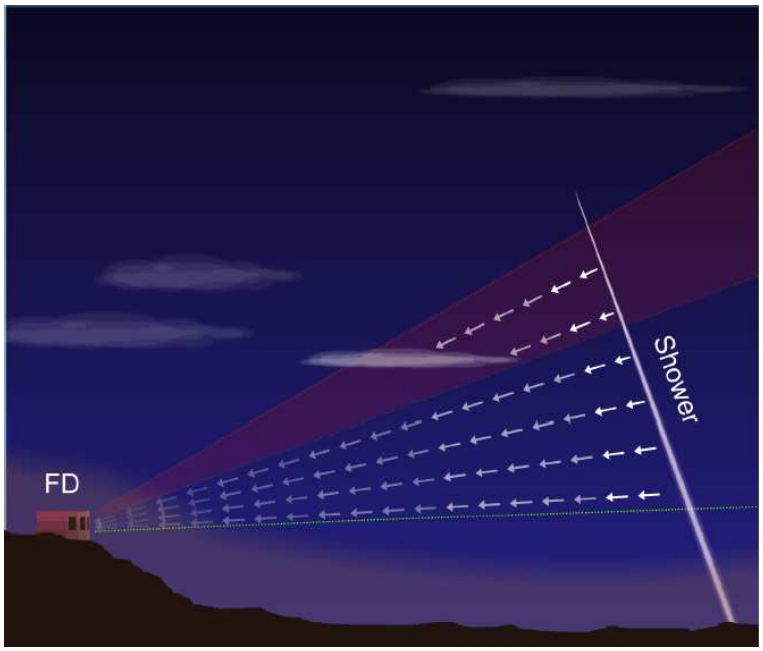

Figure 4.1: Schematic view of the fluorescence light travelling the atmosphere towards an FD building.

depolarization factor $\rho_m = 0.0310$ and changing the Rayleigh Attenuation Length from 2974 g/cm^2 to 2874 g/cm^2 as reported by Bucholtz [109]. Anyway, in the FDSim configuration of the detector the Earth curvature and the difference in height due to hills was not taken into account. In this analysis CLF laser light profiles are simulated at each FD building, and the plane Earth approximation used in FDSim made impossible a proper simulation of CLF profiles as seen from Coihueco, because the Coihueco FD building is located at 1691.9 m a.s.l., ∼250 m higher than the CLF location (1416 m a.s.l.). Only Los Leones (1416.2 m a.s.l.) profiles could be properly generated. Moreover, a great number of variables describing the detector (electronics, optics, etc.), were actually doubled in an analysis chain in which simulation and reconstruction were performed with different codes (FDSim and Offline respectively), leading to a possible source of inconsistencies.

When the migration of simulations from the old FDSim approach to the Offline started, the most obvious solution for this analysis was the development and the implementation of the Laser Simulation code in the Auger Offline software.

The laser simulation sequence I implemented is very similar to the one used for shower simulation; most of the modules are in common, in order to keep as similar as possible the simulation of both kinds of events. Figure 4.2 shows the sequence of modules in use for laser simulation in comparison with the one used for shower simulation.

```
<!-- A sequence for an FD simulation -->
<sequenceFile>

<enableTiming/>

  <moduleControl>

  <loop numTimes="1" save="yes">

    <module> ProfileSimulatorOG           </module>
    <module> EventGeneratorOG             </module>
    <module> ShowerLightSimulatorKG       </module>
    <module> LightAtDiaphragmSimulatorKG  </module>
    <module> TelescopeSimulatorKG         </module>
    <module> FdBackgroundSimulatorOG      </module>
    <module> FdElectronicsSimulatorOG     </module>
    <module> FdTriggerSimulatorOG         </module>
    <module> EventBuilderOG               </module>
    <module> UserModule                   </module>
    <module> EventFileExporterOG          </module>

  </loop>

</moduleControl>

</sequenceFile>
```

```
<!-- A sequence for an FD simulation -->
<sequenceFile>

<enableTiming/>

  <moduleControl>

  <loop numTimes="1" save="yes">

    <module> LaserGeneratorNA             </module>
    <module> EventGeneratorOG             </module>
    <module> LaserLightSimulatorNA        </module>
    <module> LightAtDiaphragmSimulatorKG  </module>
    <module> TelescopeSimulatorKG         </module>
    <module> FdBackgroundSimulatorOG      </module>
    <module> FdElectronicsSimulatorOG     </module>
    <module> FdTriggerSimulatorOG         </module>
    <module> EventBuilderOG               </module>
    <module> UserModule                   </module>
    <module> EventFileExporterOG          </module>

  </loop>

</moduleControl>

</sequenceFile>
```

Figure 4.2: ModuleSequence for shower (left) and laser (right) simulation as in Offline/Documentation/Examples/FSimulation and FLaserSimulation

The full simulation of an event (laser or shower) requires to:

1. set core position and time. The position is set in UTM coordinates, the time of impact at ground (or the time of the laser shot) is given in yy-mm-dd:hour:minutes:seconds format.

2. set energy, wavelength (for laser) and axis direction. In the reference frame centered in the core position, with x-y-z axes oriented respectively towards East, North and the local vertical directions, the axis direction is assigned setting azimuth and zenith angles.

3. follow the shower development, or in the laser case, propagate the light along the axis. Cherenkov and Fluorescence contributes must be calculated in case of shower events.

4. calculate the amount of light scattered in each FD building direction, and propagate it through the atmosphere, taking into account Rayleigh and Mie scattering/attenuation;

5. process the event through the detector.

The Offline configuration of the detector takes into account the Earth curvature. FD buildings and core positions (or laser position) are set in UTM *Universal Transverse Mercator* coordinates (fig. 4.3).

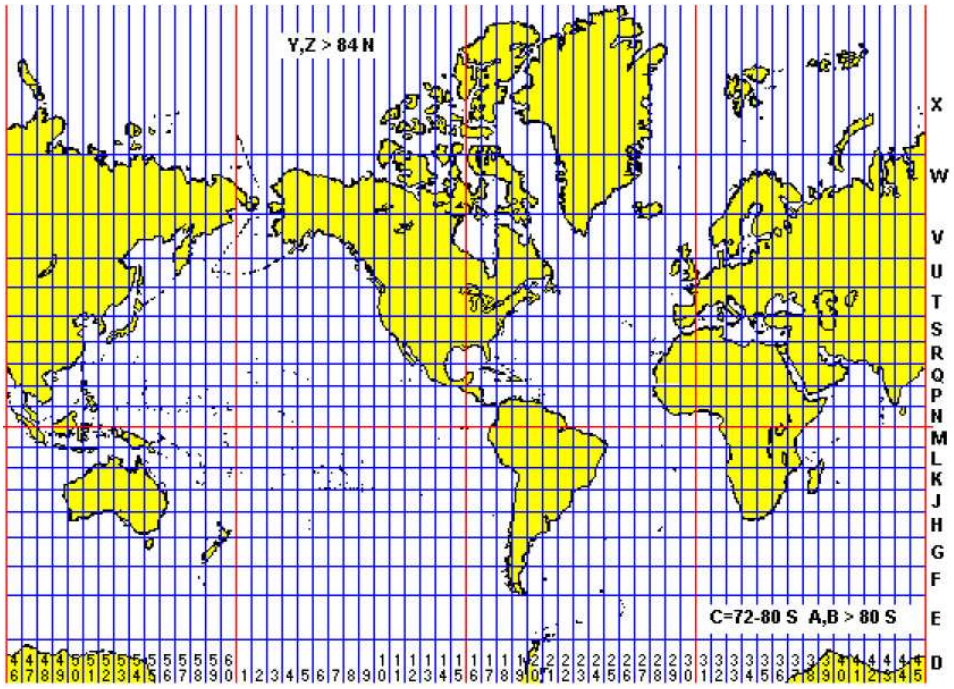

Figure 4.3: UTM projection on the Earth. The Earth is divided into 19 latitude zones and 60 longitude zones. The Auger South zone is the H19.

The Mercator projection is a conformal projection, meaning that angles and small shapes on the globe project as the same angles or shapes on the map; this projection is very accurate in narrow zones. In the Universal Transverse Mercator coordinate system, the globe is divided into narrow longitude zones, which are projected onto a Transverse Mercator projection; then, a grid is constructed on the projection and is used to locate points. With this system, the Earth is divided in 60 longitude zones, each 6° wide, and 19 latitude zones, 8° wide. A square grid is superimposed on each zone, aligned so that vertical grid lines are parallel to the central meridian. UTM grid coordinates are expressed as *"easting"*, a distance in meters to the east, and *"northing"*, a distance in meters to the north. The easting of the central meridian of each zone is arbitrarily assigned to 500000 m. UTM northing coordinates are measured with respect to the equator; for locations on the northern emisphere, the equator northing is assigned to 0; for the southern emisphere, to avoid negative numbers the equator northing is assigned to

10000000 m. With this coordinate system, the Auger South lays in the H19 zone. The UTM coordinates of FD buildings and laser devices used in my analysis are listed in the table below.

Location	Easting	Northing	Heigth
Los Leones (Eye1)	459208.3	6071871.5	1416.2
Los Morados (Eye2)	498901.8	6094569.6	1415.5
Loma Amarilla (Eye3)	484969.0	6136224.0	1400.0
Coihueco (Eye4)	445346.0	6114141.8	1691.9
CLF	469378	6095769	1412

Table 4.1: UTM coordinates of the four FD buildings and the two Laser Facilities (CLF and XLF).

The modules developed in Naples specifically for laser simulation are *LaserGeneratorNA* and *LaserLightSimulatorNA*.

The LaserGenerator module sets direction, energy and wavelength of the laser event; a configuration file (*LaserGeneratorNA.xml*, see fig.4.4) allows the user to set the zenith (theta) and azimuth (phi) angles [degrees], the energy [joule] and the wavelength [nanometer]. A flag to activate the random generation of the initial number of photons is planned but not yet implemented.

Variables theta, phi and energy are stored in the Auger Offline data class (ShowerSimData) already used for showers. Anyway, this class is not structured to store peculiar laser information as the wavelength and the polarization status[1], hence a new data class (LaserData) has been implemented in the Offline to register these data.

The LaserLightSimulatorNA module contains the code for the propagation of the laser light along the beam. The starting number of photons $N0_{\text{photons}}$ is calculated from the energy set in the LaserGenerator.xml configuration file:

$$N0_{\text{photons}} = \frac{\text{Energy[J]}}{hc/\lambda}$$

where h is the Planck's constant ($6.62606876 \times 10^{-34} Js$), c is the speed of light ($299792458\ m/s$) and λ is the laser's wavelength expressed in nanometers.

[1] not yet implemented

Printed by Laura Valore

Oct 02, 07 10:40 **LaserGeneratorNA.xml** Page 1/1

```
<?xml version="1.0" encoding="iso-8859-1"?>

<!-- Configuration of Module LaserGeneratorNA -->

<!-- In the LaserGeneratorNA tag we define the path and name of the schema file
(LaserGeneratorNA.xsd) used to validate this xml file. When make is invoked,
/scratch/work/AOL/Offline/share/auger-offline/config gets replaced by the path t
o the directory in the instal
l area
where configuration files are copied. -->

<LaserGeneratorNA xmlns:xsi="http://www.w3.org/2001/XMLSchema-instance"
    xsi:noNamespaceSchemaLocation='@XMLSCHEMALOCATION@/LaserGeneratorNA.xsd'>


<theta unit="degree"> 180.0 </theta>

<phi unit="degree"> 180.0 </phi>

<Energy unit="joule"> 0.0065 </Energy>

<Wavelength unit="nanometer">  355 </Wavelength>

<generate_photons> 0 </generate_photons>

<alpha> 3.0 </alpha>

<generate_seed> 0 </generate_seed>

</LaserGeneratorNA>
```

Tuesday October 02, 2007 LaserGeneratorNA.xml 1/1

Figure 4.4: The configuration file LaserGenerator.xml; with these settings, a vertical laser event is generated, with wavelength 355 nm and energy 6.5 mJ.

The laser track is divided into segments: the number of photons that propagates between two consecutive points P1, P2 is evaluated multiplying the number of photons in P1 by the transmission factors that account for Rayleigh and Mie attenuation in the segment. The equivalent module for showers (ShowerLightSimulator) contains the calculation of Cherenkov and Fluorescence light that is unsuited to the case of a laser event. The propagation of photons through the atmosphere from the source to the FD telescopes is developed in the LightAtDiaphragmSimulatorKG module, used for any kind of event.

Figures 4.5 and 4.6 show respectively a simulated and a real CLF vertical event as registered by Los Leones Bay4. In both cases the left panel shows the pattern of fired pixels, and the right panel shows the ADC signals corresponding to the selected pixels.

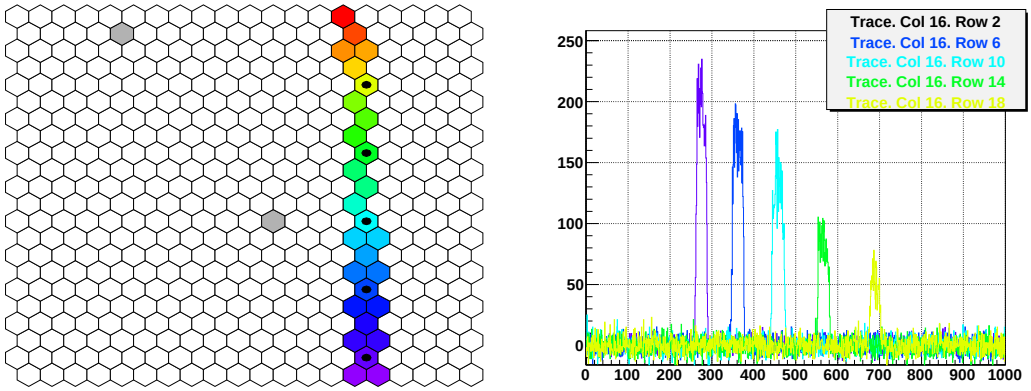

Figure 4.5: Simulated CLF vertical event. Left: track as seen in Eye1, bay4. Right: the ADC signals corresponding to the selected pixels.

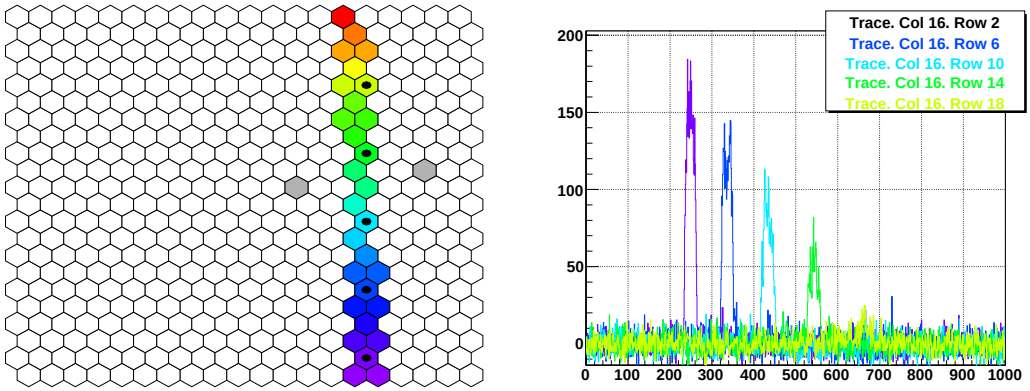

Figure 4.6: Real CLF vertical event. Left: track as seen in Eye1, bay4. Right: the ADC signals corresponding to the selected pixels.

4.3 CLF profile reconstruction

4.3.1 Light collection procedure

Once FADC traces are reconstructed and the geometry[2] is determined, the collection of light is performed.

The standard procedure in the Offline for collecting photons along the event track (implemented in the FdApertureLightOG module) uses a Signal/Noise maximization algorithm for finding the optimal light collection angle from the shower image on the camera (see section 2.10.2). The light is collected in the chosen area and the "profile at diaphragm", i.e. the number of photons at the telescope aperture as a function of time, is derived. This procedure discards sections of the track close to the camera borders, in order to avoid superimposition of near border signals when tracks cross two cameras. This is not needed in this analysis, because it relies on CLF vertical events, whose track is registered by a single camera for each eye. Moreover, the discarded track section changes event by event, and is not possible to take it into account in the simulation.

A different module for light collection has been developed, by collecting charge from the light spot position as a function of time as used in the gnomonic SDP finding approach developed by the Naples group [124]. At each time bin the average light spot position weighted by charge is computed and its charge corresponds to the amount of light at that time.

Figure 4.7 shows the profile of the same event as reconstructed with the standard Offline (left) and with the new approach (right). Part of the signal is clearly missing in the Offline standard reconstruction.

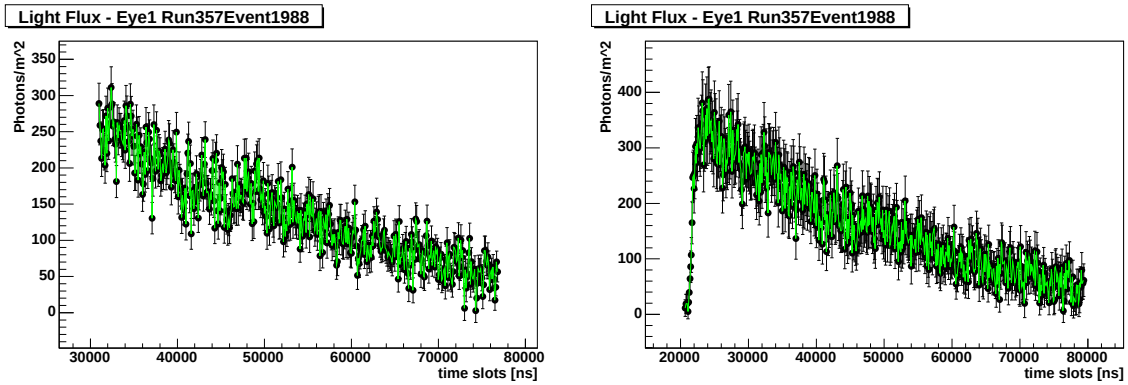

Figure 4.7: LightFlux comparison for a typical CLF vertical event: standard Offline approach is shown on the left, our module on the right.

[2]The geometry is fixed, in order to reduce indeterminations.

Single event profiles are characterized by large fluctuations. The Central Laser Facility fires groups of 50 vertical shots every 15 minutes, so, to avoid large fluctuations, average profiles of 50 events are produced for this analysis. The average profiles reveal very clearly the details of the shape and the structures due to the detector; in figure 4.8 a single CLF event profile (left) and a 50 CLF events average profile (right) are shown for comparison.

As for real events, also simulations are generated in groups of 50 to build average profiles of light at the aperture for the comparison procedure.

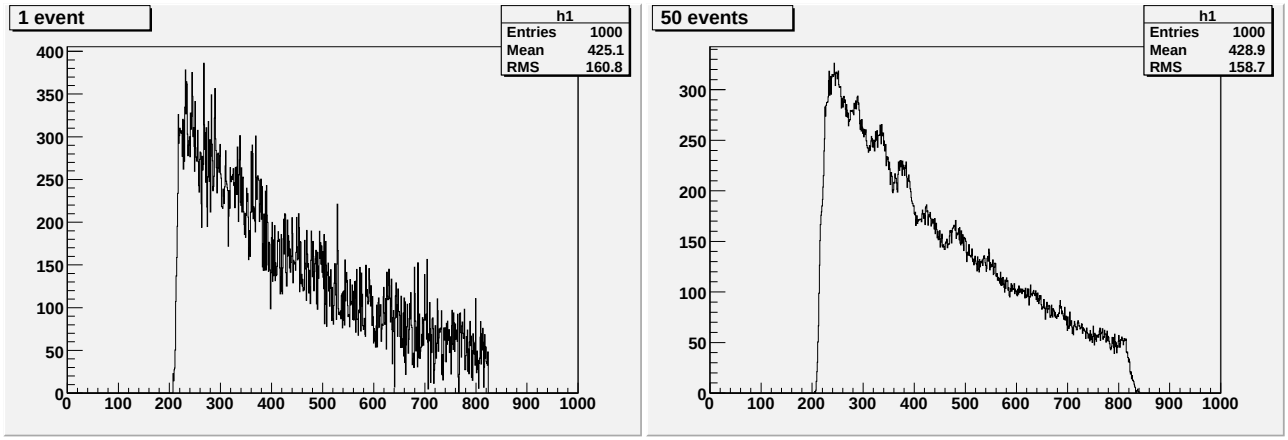

Figure 4.8: Left: a single CLF event profile of light at diaphragm. Right: the average profile computed on 50 events.

4.3.2 Getting laser event information from CLF log files

CLF run informations (zenith/azimuth angles, energy, GPStime) are stored in ascii files named *autologs*[3], which are automatically produced during laser firing. These informations are needed in the reconstruction chain. A procedure has been set up to read autolog files in order to select only vertical events and to identify the group of 50 to which the single event belongs (needed to build the average profile of each group); for each of these events, gpstime and energy probes values are extracted and written in monthly output files ($CLF - data - Y_{year}M_{month}.txt$). Each file contains a "header", with group informations (sequential number, GPS reference time for the group, number of events, zenith, azimuth) followed by rows containing informations of each event belonging to the "header" group (sequential number, GPS time, probe1

[3]autolog files can be found at http://augersw1.physics.utah.edu/clf/data/index.html

energy, probe2 energy, average energy of the 2 probes).

The conversion from CLF probes values to energy [mJ] is performed multiplying each value for a calibration constant, depending on the "CLF epoch". An "epoch" is defined as a period in which no major changes occurred to CLF hardware.

4.3.3 New Offline modules

In the reconstruction chain, CLF run informations are used to skip inclined events and to produce average profiles. For this purpose I developed two Offline modules: *FdCLFSelectEvents.cc* and *FdMeanProfile.cc*. The first reads the monthly CLF-data file corresponding to the event in analysis, skips not vertical events and associates single events to their group; moreover it stores the nominal energy of each laser shot. As suggested from CLF hardware group, probe2 is more accurate and stable than probe1; for this reason, the nominal laser energy is always given by probe2, apart from 2004 and early 2005 in which it was still not available: in this case the module stores probe1 energy.

The module FdMeanProfile.cc extracts the light flux of each event adding the number of photons at diaphragm contained in each time bin, until an event belonging to the following group is processed and the average profile of the group is computed. The nominal energy of each CLF event is used to normalize each real profile to a reference energy (6.5 mJ), to compute an average 6.5 mJ equivalent profile for each group of shots. The choice to normalize real profiles to a reference energy allows to build the grid of simulations fixing once for all the initial number of photons emitted by the simulated laser source. Hence, a grid is generated fixing the energy and the geometry of the laser event and varying the atmospheric conditions.

4.3.4 Real/simulated profile time shift

The absolute timing of CLF events is not reproduced in the simulations; cables and electronics delays (which are different for each eye) are not taken into account in detail. This produces a shift between real and simulated profiles (see figure 4.9).

To take into account this effect, real profiles have to be shifted by 27 time bins forward in Los Leones, and 33 time bins in Coihueco. Another refinement has been adopted, choosing to compare profiles only between time bin 260 and 840 in LosLeones and between time bin 230 and 930 in Coihueco. This choice is due to profile features (as the rising of the profile) that are not well

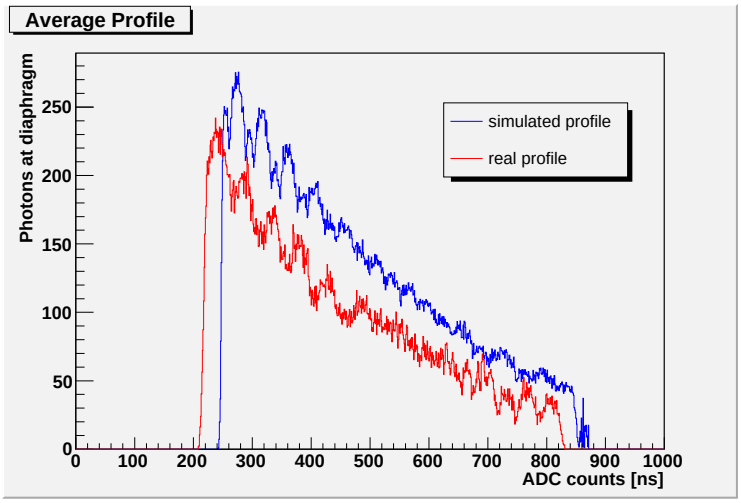

Figure 4.9: Shift between real and simulated CLF vertical profiles.

reproduced in the simulations, because of multiple scattering and/or jitter in the timing of real events not taken into account in the simulations. The effect is visible in simulated profiles, characterized by thin structures not visible in real profiles. This aspect has to be refined; at the moment we choose to cut the rising and the fall of profiles.

4.4 Atmospheric Model Description

Simulated profiles are generated in a variety of aerosol concentrations. The atmospheric model adopted in this analysis is based on the assumption that the aerosol distribution in the atmophere can be reasonably described by two parameters: the Aerosol Horizontal Attenuation Lenght (L_{mie}) and the Aerosol Scale Height (H_{mie}). The first describes the aerosol concentration at ground level, the second accounts for its dependence on the height. Horizontal uniformity is assumed. With this parametrization the expression of the Aerosol Transmission Factor is:

$$T_{aer} = \exp\left(\frac{H_{mie}}{L_{mie}\cos\theta}\left[\exp\left(-\frac{h_2}{H_{mie}}\right) - \exp\left(-\frac{h_1}{H_{mie}}\right)\right]\right)$$

where h1, h2 are the altitudes above sea level of the first and second observation levels respectively, and θ is the zenith angle of the light path. The expression can be compressed using the Aerosol Extinction Coefficient α(z):

$$T_{aer} = \exp\left[-\int_{h_1}^{h_2} \alpha(z)dz\right]$$

In the Pierre Auger Experiment the aerosol concentration is described by means of the aerosol extinction $\alpha(z)$ and the Vertical Aerosol Optical Depth as a function of the height VAOD(z):

$$\alpha(\mathrm{z}) = \frac{1}{L_{mie}}\left[\exp\left(-\frac{z}{H_{mie}}\right)\right] \tag{4.1}$$

$$\mathrm{VAOD}(h_2 - h_1) = \int_{h_1}^{h_2} \alpha(z)dz = -\frac{H_{mie}}{L_{mie}}\left[\exp\left(-\frac{h_2}{H_{mie}}\right) - \exp\left(-\frac{h_1}{H_{mie}}\right)\right] \tag{4.2}$$

In figure 4.10 a schematic view of the aerosol layer that follows the ground profile is shown. In the Auger experiment all values are referred to the sea level.

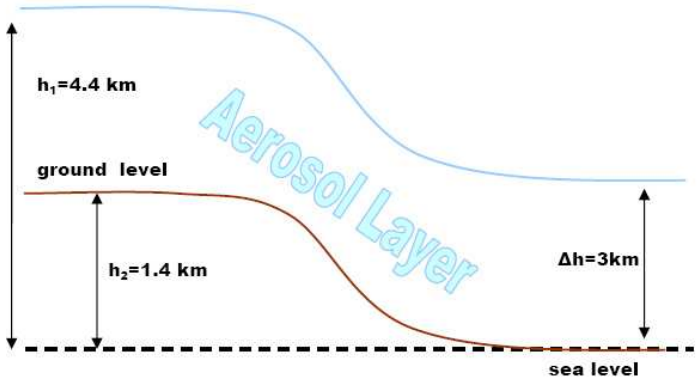

Figure 4.10: Schematization of the aerosol layer

4.5 Method Description

The procedure is based on the comparison of real CLF light profiles with a grid of simulated laser profiles in different aerosol concentration conditions.

The atmospheric conditions are determined once the aerosol and molecular concentrations are defined:

- The aerosol concentration, according to the parametric atmospheric model adopted, is determined setting values for L_{mie} and H_{mie}. A grid

is generated varying L_{mie} from 5 to 150 km in steps of 2.5km and H_{mie} from 0.5km to 5km in steps of 0.25km, obtaining 1121 profiles.

- Temporal variations of molecular profiles are continuously monitored with meteorological radio soundings and ground-based weather stations, and monthly average profiles describing the atmosphere near Malargüe have been developed, as discussed in section 3.3.1. These profiles, named Malargüe Monthly Models, are used in the simulation and reconstruction of real events. To take into account the variation of the molecular concentration over one year, one grid for each month has been produced using Malargüe Monthly Models ("monthly grids"). A total of $\sim 1100 \times 12$ average profiles were simulated.

Each real profile is compared to its whole monthly grid. Figure 4.11 shows a real profile (blue) compared to 4 out of 1121 simulated profiles (red).

The aerosol concentration is determined choosing the simulated profile, identified by the parameters pair L_{mie}^{best}, H_{mie}^{best}, closest to the real one.

4.6 The choice of the comparison algorithm

The quantification of the difference between real and simulated profiles is the crucial point of the Laser Simulation method. Three different algorithms were tested:

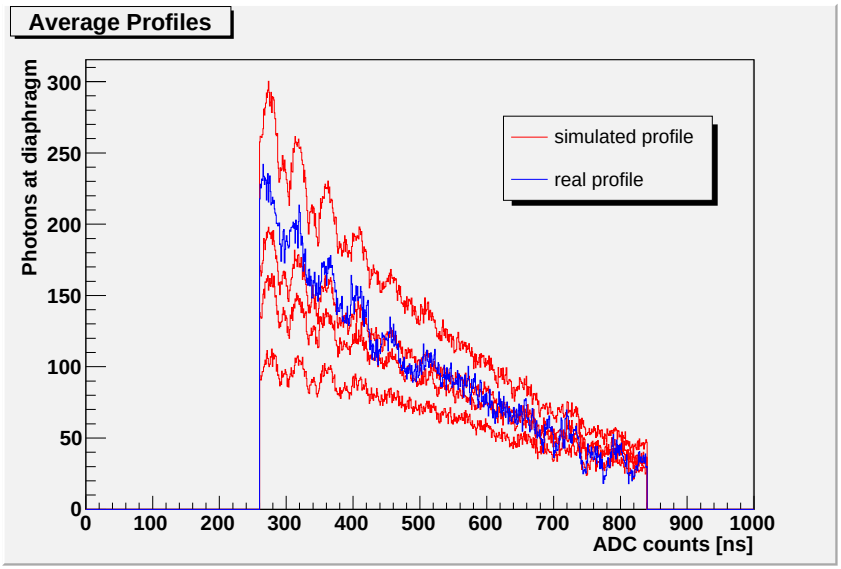

Figure 4.11: example of 4 out of 1121 simulated profiles of a monthly grid (red) superimposed to a real profile (blue)

Square Difference: for each bin it computes the square difference between histograms and sum on all bins: $D^2 = [\sum_i (\Phi_i^{real} - \Phi_i^{sim})^2]$ where Φ_i are reconstructed photons at diaphragm in each time bin. The atmospheric parameters of the simulated profile in the grid that minimizes the distance from the real profile are chosen.

Kolmogorov Test: is a statistical test of compatibility in shape between two histograms. In this case the parameters chosen are those of the simulated profile that maximize the Kolmogorov probability on the shapes.

Mixed Strategy: uses the Kolmogorov probability weighted by the inverse of the square difference: the values of L_{mie} and H_{mie} that maximize the following quantity $Q = P(Kolmo_N) \times (1/D^2)$ are chosen.

Before starting large scale analysis all the methods were tested on simulations to select the most reliable and accurate in extracting the correct aerosol parameters. A set of 50 CLF vertical events was generated in 36 different validation atmospheres with the following characteristics:

- energy = 6.5 mJ;
- L_{mie} = 11.3, 17.8, 20.5, 22.6, 23.5, 30.5, 33.9, 36.5, 43.5, 45.2, 52.5 and 56.5 km;
- H_{mie} = 1.4, 2.8 and 4.2 km.

The analysis was performed with the three methods by comparing the simulated test profile with the whole grid. Figure 4.12 left shows the distribution of distances for the Square Difference method (D^2) on the set of simulated events with L_{mie} 33.9 km, H_{mie} 2.8 km. Each bin identified by a L_{mie}, H_{mie} pair defines an atmosphere in the grid. For each validation atmosphere the differences between generated and reconstructed parameters (ΔL_{mie}, ΔH_{mie}) are computed. The plot on the right shows the D^2 validation test results on the whole set of simulated events. Figures 4.13 and 4.14 show the corresponding plots for the Kolmogorov and Mixed approaches.

Figures 4.12, 4.13 and 4.14 show that the Square Difference method is the most accurate, having mean values and root mean squares of the bidimensional distribution in the right panel of figure 4.12 smaller than those of the other approaches.

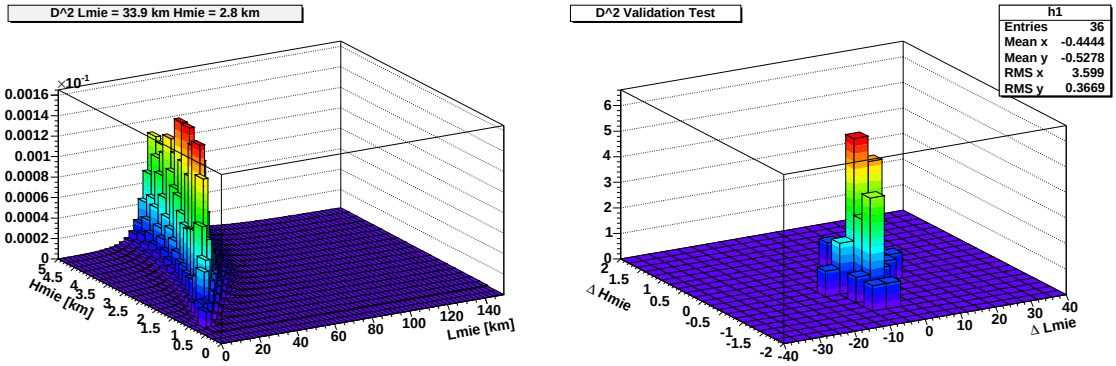

Figure 4.12: Left: distribution of distances for D^2 method (L_{mie} 33.9 km, H_{mie} 2.8 km). Right: corresponding validation test.

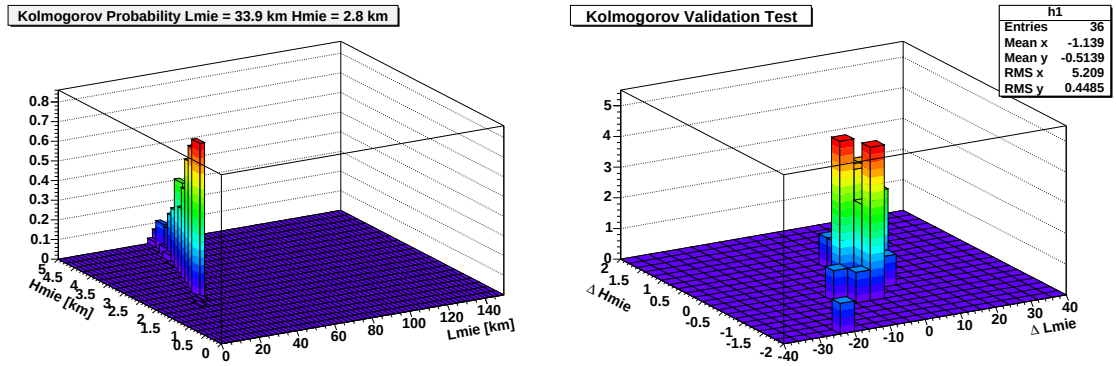

Figure 4.13: Left: distribution of probabilities for Kolmogorov method (L_{mie} 33.9 km, H_{mie} 2.8 km). Right: corresponding validation test.

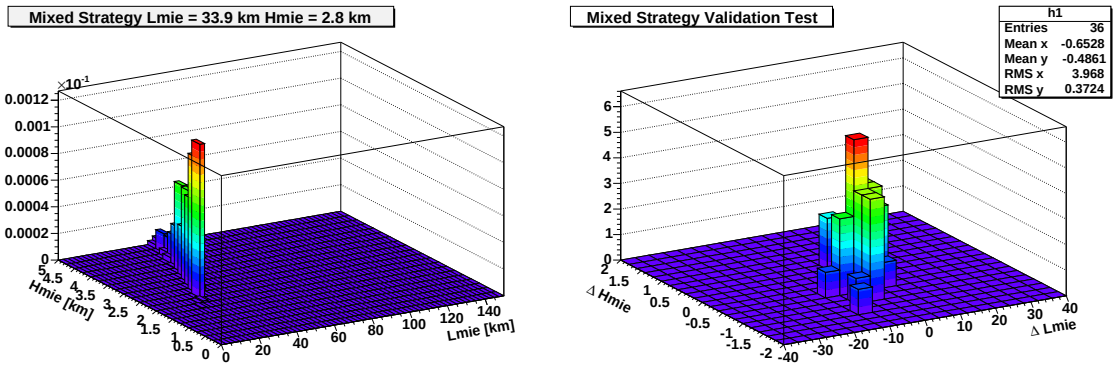

Figure 4.14: Left: results for Mixed Strategy method (L_{mie} 33.9 km, H_{mie} 2.8 km). Right: corresponding validation test.

Figure 4.15 shows the simulated "bestprofile" superimposed to the real one. Once the appropriate aerosol content is chosen, the simulated profile can reproduce real data with extreme accuracy. This supports the validity of the approach and the use of a parametric atmospheric model.

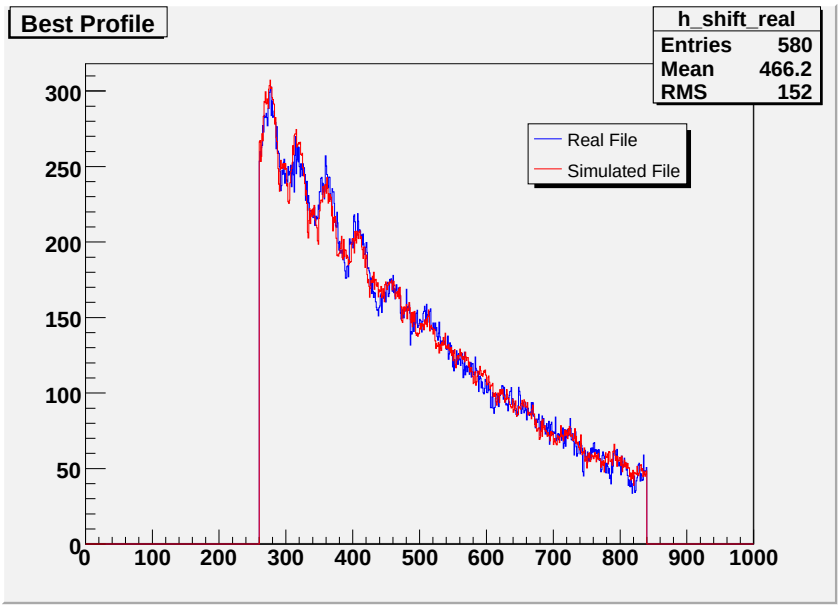

Figure 4.15: Example of the excellent compatibility of the simulated profile chosen (red) to the real profile in analysis (blue).

Clouds scatter a greater amount of laser light into the FD field of view, producing spikes in the light profiles, as shown in figure 4.16.

The final strategy, chosen on the basis of the described study, makes use at first of an algorithm to reject irregular profiles, and then the Square Difference method is applied to measure the aerosol concentration. The procedure is applied to every CLF real event registered by the Fluorescence Detector. Since the laser fires sets of 50 shots every quarter-hour, the aerosol concentration is measured every 15 minutes (as long as FD is operating and registering CLF runs). However, hourly aerosol data are requested by the Auger Collaboration to fill the Aerosol Database, hence results are averaged on the corresponding hour.

4.7 Data Analysis and Errors Determination

Results are expressed as hourly $VAOD(z)$, $\alpha(z)$ as a function of the height (see section 3.3.2), with the associated errors $\mathrm{VAOD_{Err}(z)}$, $\alpha_{\mathrm{Err}}(z)$. Once

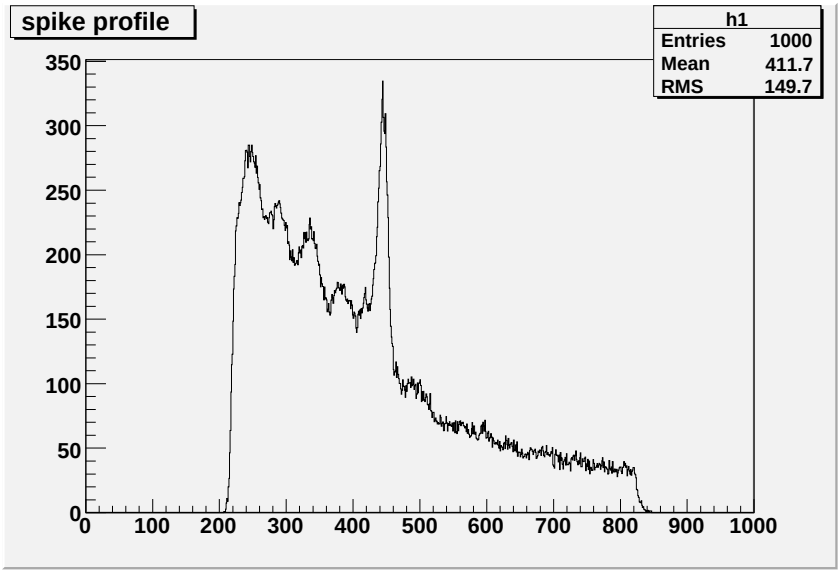

Figure 4.16: Example of irregular profile: the spike is due to a cloud.

L_{mie}^{best}, H_{mie}^{best} are identified, equations 4.1 and 4.2 are applied to calculate $\alpha(z)$ and $VAOD(z)$ respectively. The analysis described does not produce results in presence of clouds; hence results are always produced up to the maximum heigth visible by FD telescopes, depending on the distance between the CLF and the eye in analysis. This means, i.e. for Los Leones Bay4, that results are given from 1416.2 m to 15016.2 m. Heights are referred to the sea level, and the maximum heigth visible by a telescope is given by:

$$H = \mathrm{D} \times \mathrm{tg}(\beta)$$

Where D is the distance between the CLF and the FD building and β is the field of view of a telescope (30°). The track lenght visible from Los Leones is schematized in figure 4.17.

The uncertainty on VAOD(z), $\mathrm{VAOD_{Err}(z)}$, is calculated taking into account both the statistic error $\Delta_{\mathrm{VAOD}}(z)$ and the systematic errors $\mathrm{Err_{Sys}}$ arising from the variables involved in the procedure.

The evaluation of the statistic error $\Delta_{\mathrm{VAOD}}(z)$ associated to the results expressed as VAOD(z) is performed taking into account the indetermination due to the comparison algorithm used to extrapolate the aerosol concentration.

The procedure is the following: after the determination of the couple L_{mie}^{best}, H_{mie}^{best} that maximize the quantity $Q = (1/D^2)$, the test is repeated

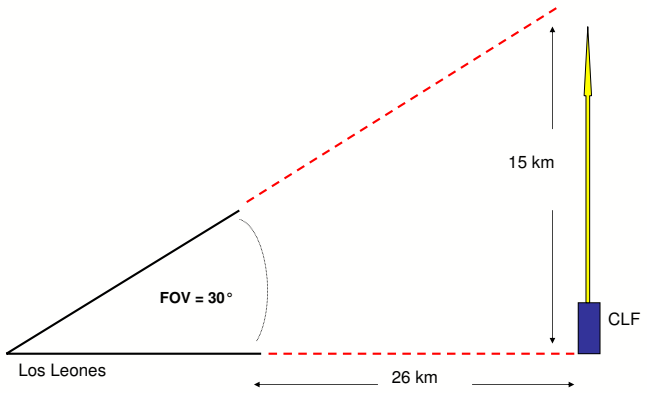

Figure 4.17: Los Leones Bay4 - CLF scheme. At 26 km of distance, with a 30° field of view, the laser track is visible up to 15 km of height.

a second time in order to find the couple $L_{mie}^{\rm err}$, $H_{mie}^{\rm err}$ corresponding to the quantity Q' nearest to Q.

The error associated to VAOD for each height is given by :

$$\Delta_{\rm VAOD}(z) = {\rm VAOD}^{\rm best}({\rm z}) - {\rm VAOD}^{\rm err}({\rm z})$$

Systematic errors should also be taken into account: the main contributions arise from FD and CLF energy calibrations. They will be discussed in details in the next chapter.

Once both $\Delta_{\rm VAOD}(z)$ and systematic errors $\Delta_{\rm Sys}$ are measured, the error ${\rm VAOD_{Err}(z)}$ to be associated to VAOD(z) is:

$${\rm VAOD_{Err}(z)} = \sqrt{(\Delta_{\rm VAOD}({\rm z}))^2 + (\Delta_{\rm Sys})^2} \tag{4.3}$$

There is a weak dependence of our ${\rm VAOD_{Err}(z)}$ from VAOD(z) due to the step used in the grid of simulations, that is divided in equal steps in L_{mie}, H_{mie} and not in VAOD(z). Anyway ${\rm VAOD_{Err}(z)}$ is largely dominated by systematic errors, and this small effect can be neglected.

The total indetermination associated to the aerosol extinction α(z) is calculated propagating the statistic error $\Delta_{\rm VAOD}(z)$:

$$\Delta_\alpha(z) = \sqrt{\frac{1}{(200)^2}\left[\Delta^2_{\rm VAOD}(z) + \Delta^2_{\rm VAOD}(z-1)\right]} \tag{4.4}$$

Chapter 5

Aerosol Determination at the Auger Observatory

5.1 Laser Simulation Analysis

The procedure described in the previous chapter was applied to all CLF available data, from january 2004 to september 2007. In these 3.7 years of data 8 main *"CLF epochs"* are present. For each epoch energy and polarization are calibrated [126] and a CLF calibration constant for probe1 and probe2 are provided, as reported in table 5.1. From january 2004 to march 2005 only one probe (photodiode) was operating; starting from march 28^{th} 2005, a second probe (pyroelectric) has been added. In the following probe 2 is used when available to obtain CLF nominal energy.

CLF Epoch	From	To	Probe1 Cal	Probe2 Cal
1	y2004m01d01	y2004m03d22	2.67×10^{10}	N.A.
2	y2004m03d22	y2004m08d24	2.56×10^{10}	N.A.
3	y2004m08d24	y2004m08d24	2.30×10^{10}	N.A.
4	y2004m08d24	y2004m11d13	2.24×10^{10}	N.A.
5	y2004m11d13	y2004m11d17	3.09×10^{10}	N.A.
6	y2004m11d17	y2005m03d28	3.04×10^{10}	N.A.
7	y2005m03d28	y2006m03d22	1.27×10^{10}	11.0×10^{3}
8	y2006m03d23	y2006m08d11	1.66×10^{10}	12.45×10^{3}
9	y2006m08d12	y2007m05d07	1.60×10^{10}	9.74×10^{3}
10	y2007m05d07		1.60×10^{10}	9.2×10^{3}

Table 5.1: CLF calibration constants to convert probes value in energy[mJ].

In figure 5.1 CLF constants as a function of time are shown.

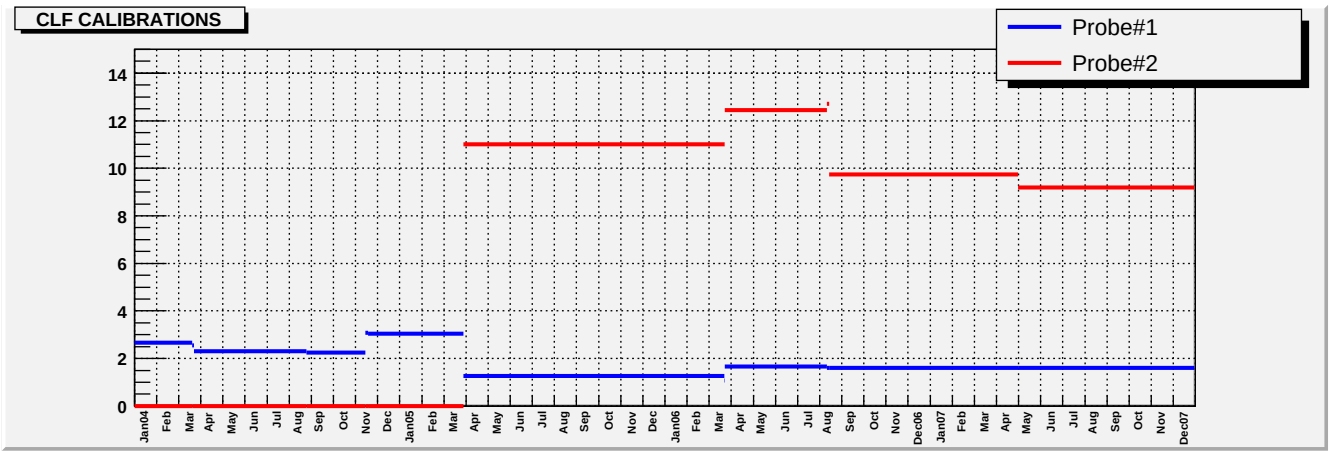

Figure 5.1: CLF calibration constants for probe1/10^{10} (blue line) and probe2/10^3 (red line) as a function of time.

Moreover, in the analyzed period the FD calibration constants have changed. The current set of calibrations in use is taking into account average results for relative calibration "A" over periods of weeks or months. Daily calibrations will be released soon. In figure 5.3 the average value of the calibration constants of the 440 pixels of the camera is shown for bay4 in Los Leones and bay3 in Coihueco (the telescopes having CLF vertical events in their field of view).

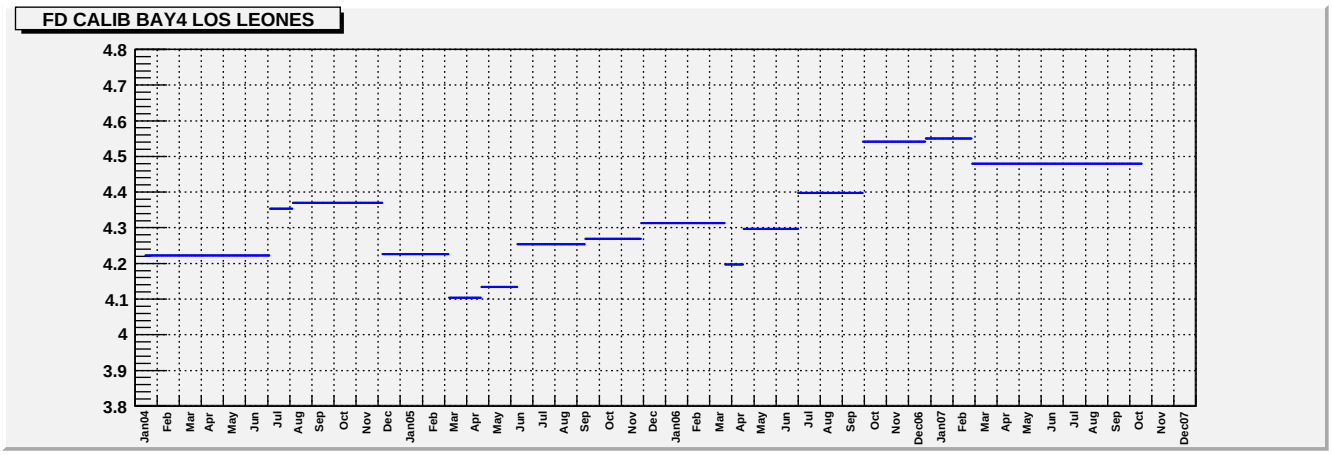

Figure 5.2: FD calibration constants for Eye1, bay4 as a function of time.

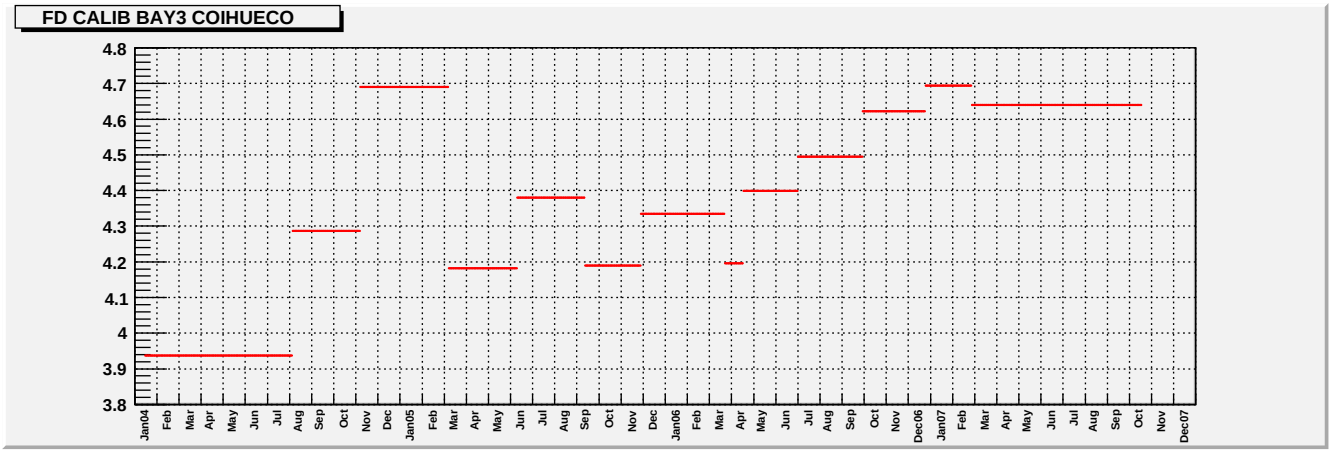

Figure 5.3: FD calibration constants for Eye4, bay3 as a function of time.

The total amount in hours of CLF events registered by the Los Leones eye in the period january 2004 - september 2007 is reported in table (5.2), together with the total numer of hourly results obtained with the Laser Simulation method. The number of hours in which the test do not produce results, mostly for the presence of clouds (see section 4.6), is also indicated. The period september-november 2004 is excluded from the analysis because it was discovered that the laser beam was not randomly polarized[1]. Also the period april - july 2007 is at the moment discarded, because the laser was running out of power (E $<$ 4 mJ, see fig. 5.4). At these low energies the adopted algorithm is not fully efficient and this, if not properly treated, can introduce non linearities in the analysis that can bias the final results. The laser was substituted in august 2006.

	Total N°events	VAOD results	Test Failures
Los Leones (Eye1)	3823	2011	1812

Table 5.2: Total amount of hourly CLF data , VAOD results from Laser Simulation method and failures of the test for the Los Leones eye.

[1]The Nd::YAG laser emits linearly polarized light, hence a depolarizer is used in order to obtain randomly polarized light to reproduce the isotropical distribution of the fluorescence light emitted by a shower.

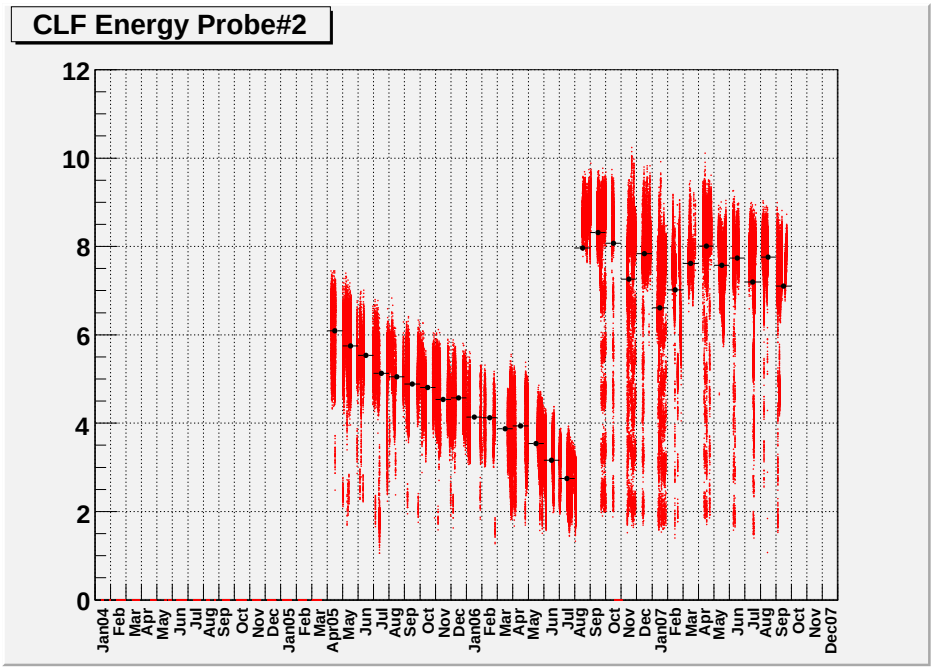

Figure 5.4: Probe2 energy[mJ] as a function of time.

In figure 5.5 the distribution of VAOD@3km for four CLF epochs is shown.

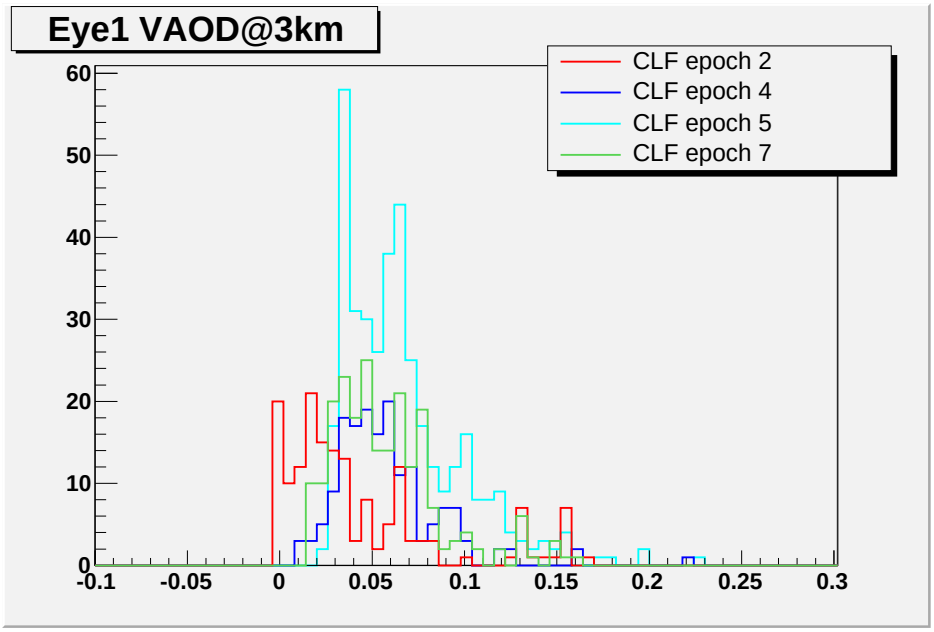

Figure 5.5: Distribution of VAOD@3km results obtained in different CLF epochs.

The distributions corresponding to the selected CLF epochs are slightly different. This can hardly be explained as due to seasonal variations in the aerosol distribution and is most probably a hint of the presence of some systematics.

5.1.1 Systematic errors

In the described analysis the main contributions to systematic errors arise from FD and CLF energy calibrations; both are multiplying factors to the number of photons.

In order to understand if systematics depend on VAOD, 10 real CLF profiles with values of VAOD@3km ranging from 0.01 to 0.1 in steps of ~ 0.01 were selected. For each of the selected profiles the light flux was increased and decreased by 10% to mimic the effect of systematics, obtaining 3 profiles (Prof, Prof$^+$, Prof$^-$). Appling the Laser Simulation method, the correct VAOD@3km, a VAOD$^+$ corresponding to Prof$^+$ and a VAOD$^-$ corresponding to Prof$^-$ were extracted. The variations of VAOD, Δ^+ = VAOD$^+$ - VAOD and Δ^- = VAOD - VAOD$^-$, are very similar and do not depend on VAOD; hence the systematic error can be estimated once for all.

The same approach has been used to evaluate the systematic errors associated to CLF ($\mathrm{CLF_{Sys}}$) and to FD calibration constants ($\mathrm{FD_{Sys}}$). The average value $(\Delta^+ + \Delta^-)/2$ is the estimate of the systematic error.

Presently quoted systematic errors $\mathrm{FD_{Sys}}$ [125] and $\mathrm{CLF_{Sys}}$ [126], and the corresponding VAOD systematics $\Delta^{\mathrm{Sys}}_{\mathrm{FD}}$ and $\Delta^{\mathrm{Sys}}_{\mathrm{CLF}}$ are reported in table 5.5:

	$\mathrm{FD_{Sys}}$	$\mathrm{CLF_{Sys}}$	$\Delta^{\mathrm{Sys}}_{\mathrm{FD}}$	$\Delta^{\mathrm{Sys}}_{\mathrm{CLF}}$
before 12-08-06	9.5%	12%	0.012	0.016
after 12-08-06	9.5%	7%	0.012	0.009

Table 5.3: VAOD systematic errors associated to CLF and FD calibration constants systematics.

The final error is computed according to equation 4.3.

5.2 Comparison with Data Normalized Method

A comparison between the analysis just described and the results presently in the Aerosol Database, obtained with the Utah group Data Normalized

analysis, was performed. The parameter chosen for the comparison is the Vertical Aerosol Optical Depth at 3km above the FD site[2]. The comparison is performed in the period from january 1^{st} 2004 to january 31^{st} 2007, since there are no data in the Aerosol Database after january 2007, excluding the months characterized by linear polarization and low laser energy. The comparison is shown in figure 5.6.

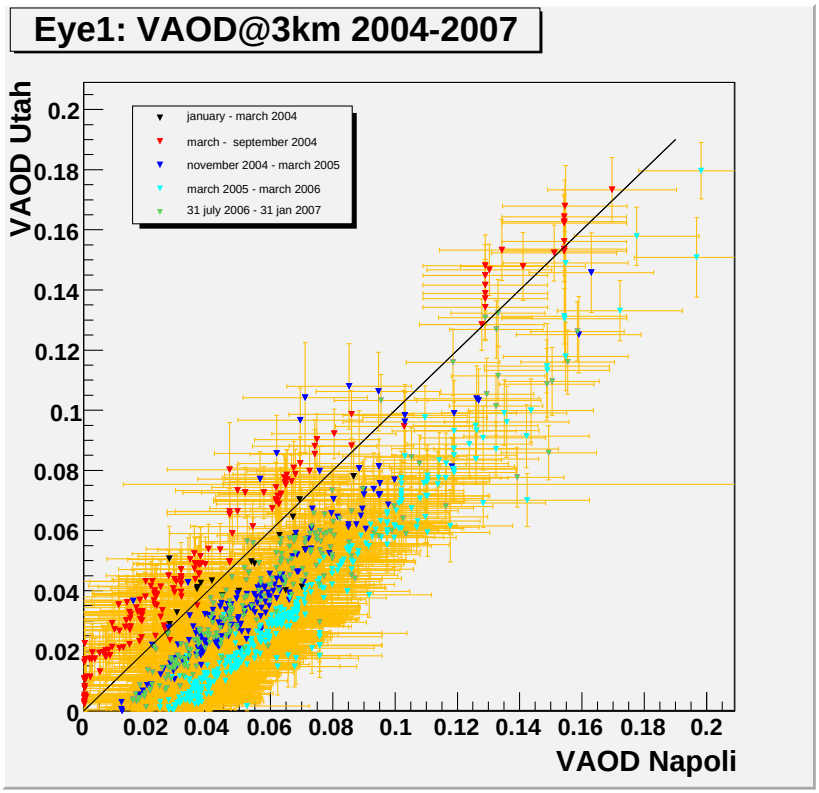

Figure 5.6: Correlation between Laser Simulation (Napoli) and Data Normalized (Utah) methods. Different colors identify different CLF epochs.

Data agree within the errors, but a clear shift in the correlation is observed between epochs, again suggesting the presence of a systematic effect due to CLF and/or FD calibration constants. In fact this analysis, that compares real profiles to simulated ones, is more heavily affected by FD and CLF calibration issues than Utah analysis, in which profiles are compared to those of nearby clean nights.

[2]Los Leones, 4416.2m a.s.l., Coihueco 1691 m a.s.l.

5.3 CLF energy reconstruction

FD and CLF calibation systematics, if at the origin of the observed discrepancy between epochs shown in figures 5.5 and 5.6, should also affect the energy reconstruction of CLF events. To check if this is the case, a systematic study of CLF energy reconstruction was performed.

The standard procedure used in the Offline for energy reconstruction of shower events is based on the Gaisser-Hillas fit performed on the longitudinal profile **??**, and cleary it is not appropriate for laser events. For this reason a specific procedure was developed, based on the idea that laser energy is proportional to the number of photons emitted by the laser source (*photons@track*) in the FD field of view.

5.3.1 The algorithm for the energy reconstruction of laser events

A specific Offline module has been developed (*CLFEnergyFinder*) for laser energy reconstruction. For each CLF event the total number of photons in the field of view of the laser track is reconstructed as a function of the atmospheric depth; then, the total number of photons (N^{γ}_{rec}) is computed integrating the laser light at track profile.

N^{γ}_{rec} is finally converted to laser energy by comparison of simulated CLF events of known energy as explained in section 5.3.2. Since the conversion from (N^{γ}_{rec}) to energy is dependent from the aerosol concentration, a parametrized function has been searched for the conversion. Once the function is defined, each CLF real event is processed and its energy reconstructed.

5.3.2 Photons to energy conversion

As anticipated, the conversion from collected photons at track to laser energy is performed with the aid of simulated events in order to estimate the expected number of photons in the FD field of view as a function of energy.

Atmospheric transparency affects laser light propagation in three ways:

1. vertical propagation of the laser beam
2. light scattering towards the detector
3. attenuation of scattered light towards the FD buildings

Corrections for light attenuation in the reconstruction only account for the third point. In order to take into account the first two contributions,

N sets of 200 CLF vertical laser events were simulated, fixing the energy (E = 6.5 mJ) and varying the atmospheric aerosol concentration. Each set was reconstructed coherently with the simulated atmosphere and the average number of reconstructed photons at track N^{γ}_{exp} was extracted. The expected number of photons N^{γ}_{exp} can be easily parametrized as a function of Vertical Aerosol Optical Depth at 3 km above the detector (VAOD@3km). Figure 5.7 shows $N^{\gamma}_{exp}/10^{15}$ vs VAOD@3km for Los Leones. Data where interpolated by a third degree polinomial; the same was done for Coihueco. Parametrization results are reportes in table 5.4:

	p0	p1	p2	p3
LL	3.88	0.92	0.67	-2.99
CO	2.47	1.06	0.06	-13.17

Table 5.4: Parametrization results for Los Leones and Coihueco.

For each CLF shot the VAOD@3km is extrapolated from the aerosol database and N^{γ}_{exp} is computed from the parametrization:

$$N^{\gamma}_{exp} = 10^{15} \times (p0 + p1 \cdot \tau + p2 \cdot \tau^2 + p3 \cdot \tau^3)$$

Where τ is VAOD@3km.

Finally the energy is estimated as:

$$E = N^{\gamma}_{rec} \times (6.5mJ/N^{\gamma}_{exp})$$

5.3.3 CLF data selection

The energy was reconstructed on the whole set of CLF vertical data from january 2004 to september 2007 appling the aerosol correction.

Events were selected according to the following criteria:

1. availability of aerosol data in the database;
2. aerosol database maximum height above 10 km;
3. the reconstructed track must cover the whole camera.

The first request is to make sure that events can be corrected for atmospheric aerosol transparency. The last two points are needed to reject events in case of presence of clouds above CLF and to ensure a good reconstruction.

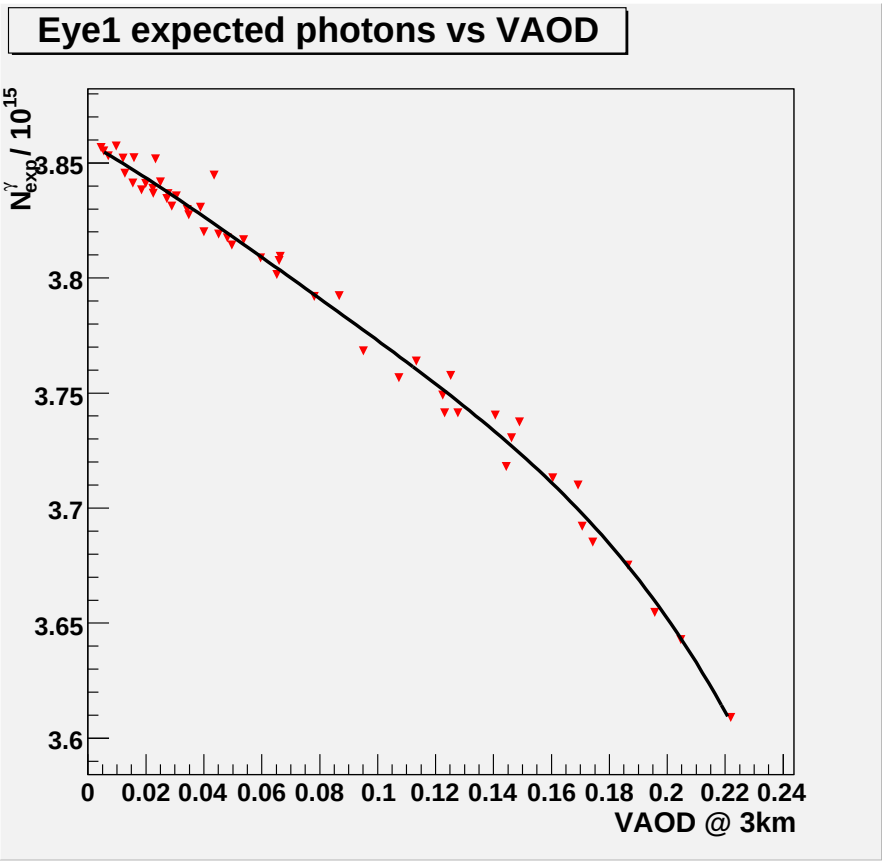

Figure 5.7: Average number of reconstructed photons at track from the simulations vs VAOD@3km for Los Leones

The nominal CLF energy is given by the value registered by the probes multiplied by the CLF calibration constant of that epoch.

Figures 5.8 and 5.9 show the ratio reconstructed/nominal energy for Los Leones and Coihueco respectively. Different colors are used to identify different CLF epochs. Epoch 3 (green) and epoch 6 (purple) are discarded for the reasons already explained. Epochs 1 and 2 are characterized by old FD calibration constants and may be affected by higher systematics.

A clear energy deficit is visible from both eyes. In particular epoch 4, 6 and 7 show the same average deficit; epoch 5 shows a greater energy deficit and a barely visible decreasing trend with time ($\sim$ 2 % in 6 months).

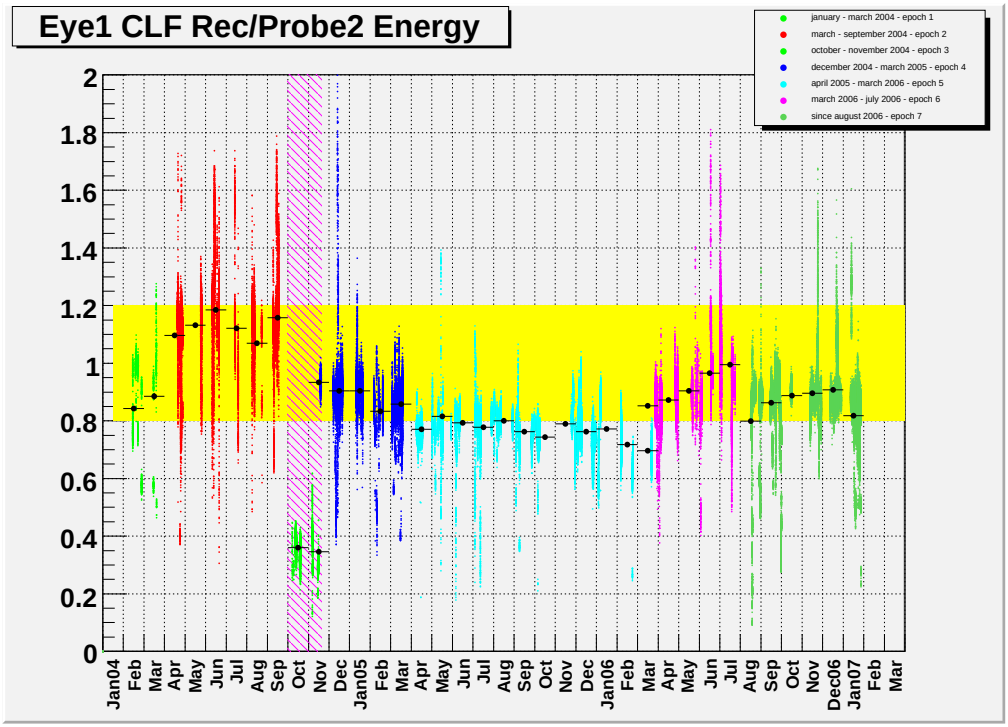

Figure 5.8: Los Leones reconstructed energy divided by probe 2 energy, since April 2005. From January 2004 to March 2005 energy/probe 1 is shown.

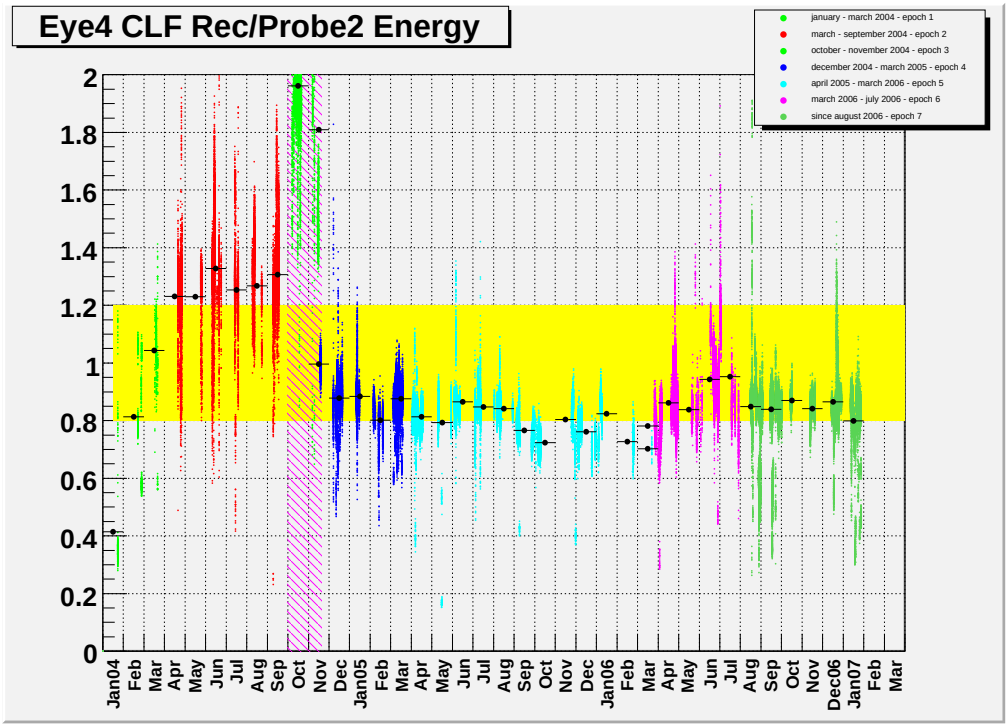

Figure 5.9: Coihueco reconstructed energy divided by probe 2 energy, since April 2005. From January 2004 to March 2005 energy/probe 1 is shown.

The same features are seen from Los Leones and Coihueco.

The data representation used in figures 5.8 and 5.9 is very useful to visualize time behaviour, but hides the true density of data points. Tails in the distribution appear much larger than they should since the density of points in the central region is saturated by graphycs. Actually the reconstructed/nominal CLF energy distributions are nicely gaussian, as shown in the next section.

In conclusion,

1. energy analysis confirms epoch related features (possibly due to CLF calibration constants systematics and/or to the choice of the Rayleigh Night in the Utah analysis);

2. puts in evidence an excess in energy up to september 2004 data (roughly corresponds to epoch 1 and 2) and a deficit starting from december 2004 data (possibly due to FD calibration constants systematics or to the simulation/reconstruction chain).

5.3.4 Energy resolution

Regardless of the systematics affecting the reconstructed laser energy, an excellent energy resolution is achieved. In figure 5.10 the energy distribution in 4 epochs is shown. Distributions are gaussian and their root mean square is always below 0.07.

Fitting the distributions with a gaussian, the following averages and RMS are obtained:

CLF Epoch	Average	RMS
2	1.14	0.07
4	0.88	0.05
5	0.77	0.05
7	0.89	0.04

Table 5.5: VAOD systematic errors associated to CLF and FD calibration constants systematics.

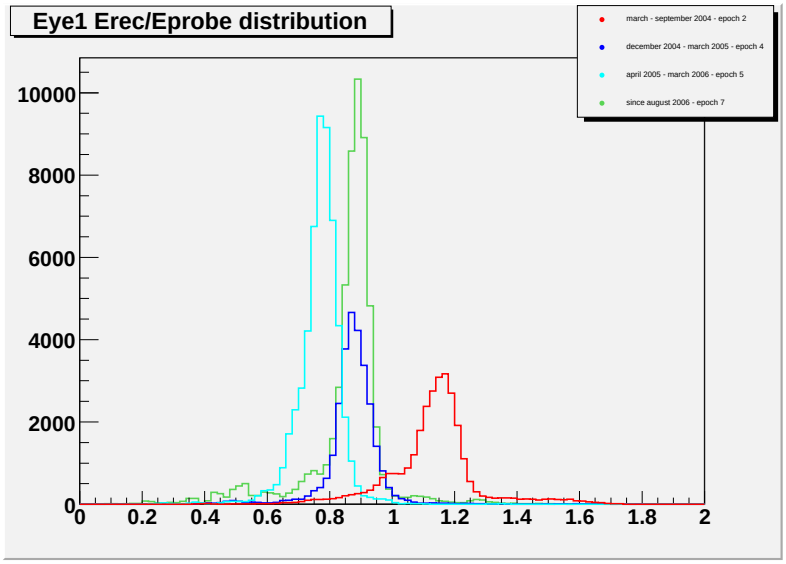

Figure 5.10: Reconstructed/nominal CLF energy distributions for Los Leones

5.4 Possible explanations for the observed energy deficit

Key ingredients in the CLF energy reconstruction that might affect both the absolute normalization and time variations are:

1. the accuracy of CLF energy probes and calibration constants;
2. the accuracy of data in the aerosol database;
3. some systematics hidden in the simulation/reconstruction chain.
4. the FD absolute and relative calibration constants;

In the following we briefly discuss the possible contributions of these factors to the observed energy decrease.

1. CLF energy probes

In figure 5.11 the ratio of CLF energy measurement of E_{probe2}/E_{probe1} versus time is shown. The ratio is rather stable and very close to 1. Probe 2 appears to be more stable: in some cases the energy returned by probe 1 is too low.

The bulk of the E_{probe2}/E_{probe1} distribution is well fitted by a gaussian distribution of mean value very close to 1. A tail due to the low energy values returned by probe 1 is also present.

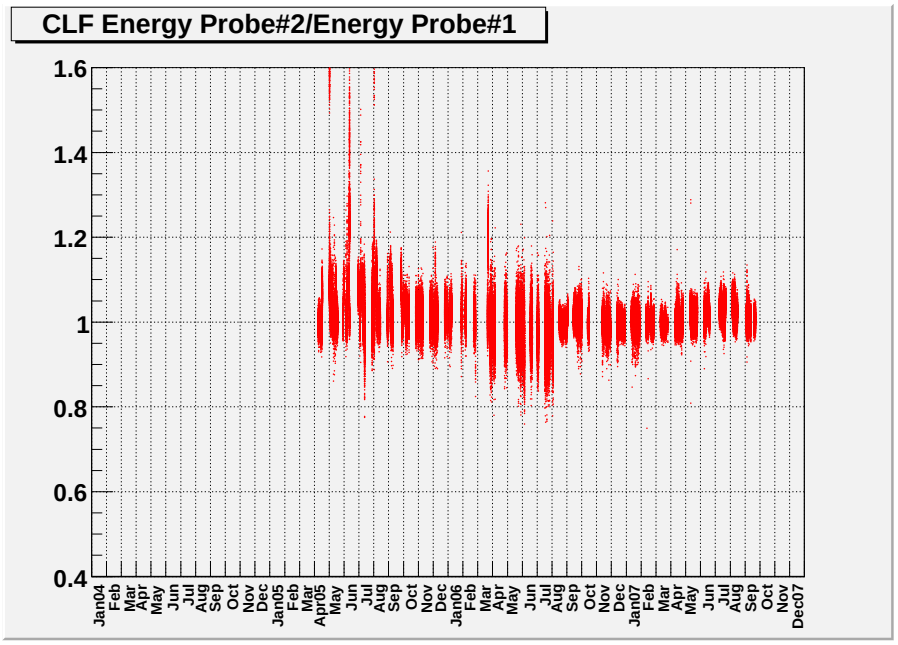

Figure 5.11: Ratio between nominal energy of Probe 2 and Probe 1.

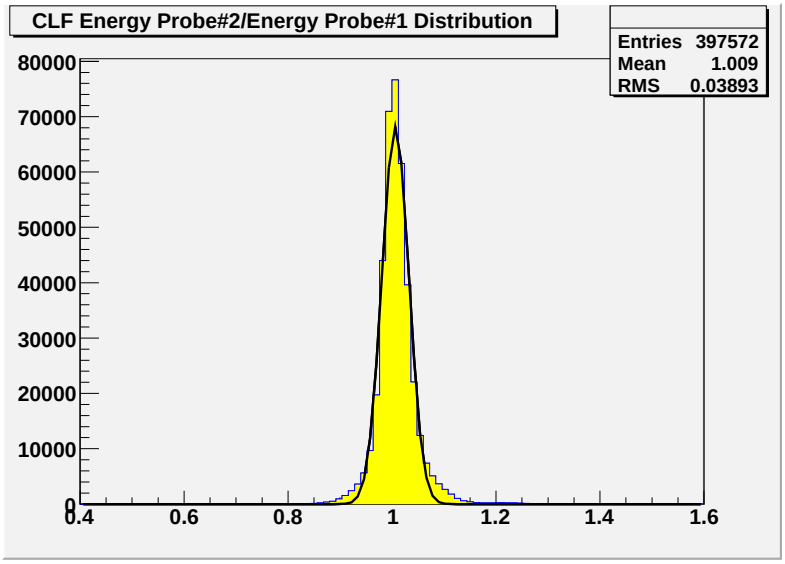

Figure 5.12: Distribution of ratio between nominal energy of Probe 2 and Probe 1.

Even if fluctuations are not negligible, the average difference between the energy returned by the two CLF energy probes is very small with the exception of limited periods.

2. Roving Laser

The *Roving Laser* is a portable, steerable, unpolarized 337 nm nitrogen laser. The laser itself, energy probe, timing/triggering system, alignment system and batteries are attached to a mechanical mount, placed on a 4x4 truck, using a partially inflated tire tube for cushion. Picture 5.13 shows the truck and the Roving Laser mounted on the back. Two measurement campaignes, in May 2005 and August 2006, were performed. The energy was around 100μJ per pulse in the 2005 campaign and around 40μJ per pulse in the 2006 campaign; the laser produces short pulses of few nanoseconds. The laser probe is located in the laser beam before and after each run. The energy stability is tipically $< 4\%$, so the laser run energy is assigned as the average of the values measured immediately before and after the run [127].

Figure 5.13: The Roving Laser device.

In the following tables the summary of the two campaignes is reported.

The laser was placed at distances D $<$ 4 km from FD buildings, hence the atmospheric aerosol attenuation is negligible. Moreover, the laser probe is different from CLF probes, so that two out of the four possible sources of the observed energy deficit can be investigated.

The energy recostruction of Roving laser events was performed in the same way as for CLF events; ad hoc simulations were performed, using the informations reported in tables 5.6 and 5.7 and using the appropriate monthly

Run	Eye	Bay	GPS start	GPS stop	Northing	Easting	Altitude[m]	Energy[μJ]
863	1	6	799387928	799389500	6074374	456708	1360	105
868	1	3	799466260	799466465	6074237	461548	1365	107.05
869	1	3	799468258	799468464	6074273	462145	1365	107.2
870	1	4	799471492	799471698	6074564	460354	1361	108.8
871	1	6	799473974	799474176	6074376	456713	1367	109.65
995	4	3	799640620	799640825	6111766	447301	1540	102.8
996	4	3	799642560	799642760	6111834	448365	1531	102.85
997	4	2	799644880	799645085	6110645	446054	1527	104.4
1003	4	3	799808539	799808737	6111833	448353	1529	96.8
1004	4	2	799811430	799811628	6110652	446060	1523	98.8

Table 5.6: Roving laser summary, May 2005 campaign.

Run	Eye	Bay	GPS start	GPS stop	Northing	Easting	Altitude[m]	Energy[μJ]
1499	1	6	839642568	839643006	6074378	456711	1369	33
1502	1	6	839644083	839644481	6074378	456711	1369	34.3
1503	1	6	839645202	839645600	6074378	456711	1369	35.5
1505	1	6	839724163	839724561	6074378	456711	1369	34.7
1506	1	6	839725117	839725515	6074378	456711	1369	35.3
1509	1	4	839730375	839730773	6074566	460346	1356	36.3
1510	1	4	839731354	839731777	6074566	460346	1356	35.9
1511	1	3	839734499	839735397	6074276	462145	1360	38.5
1512	1	3	839735934	839736332	6074276	462145	1360	38.4
1764	4	3	839900825	839901025	6111766	447277	1530	57.3

Table 5.7: Roving laser summary, August 2006 campaign.

atmosphere. A conversion constant from N^{γ}_{rec} to energy was estimated for each position.

Each group of Roving events has been reconstructed, fixing the position and calculating the number of photons at track then converted in energy by means of its specific simulation. The ratio between reconstructed and nominal energy as seen from bay4 in LosLeones and bay3 in Coihueco in 2005 and 2006 are reported in table 5.8 and compared with what observed with CLF.

The may 2005 Roving campaign took place during CLF epoch 5 (cyan), when a major energy deficit is observed with CLF both from Los Leones and from Coihueco. Most probably it is due to a miscalibration of CLF probes; for this reason the reported energy deficit for CLF in 2005 is the average of the previous (4, 12% deficit) and following (6, 15% deficit) epochs.

The analysis of Roving laser events reveals the same energy deficit as observed with CLF. The implication is that the lack of energy cannot be due to the aerosol concentration or to laser probes. Hence, FD calibration constants and the simulation/reconstruction chain used must be further investigated as the only possible reasons for the energy deficit observed. The result further supports the hypostesis of a miscalibration of CLF probes in epoch 5.

Los Leones (Eye1)	CLF	Rovings
2005	-13 %	-14 %
2006	-12.5 %	-13.5 %
Coihueco (Eye4)	CLF	Rovings
2005	-13.5%	-14 %
2006	-15 %	-10 %

Table 5.8: Energy deficit percentages for bay4 in Los Leones and bay3 in Coihueco.

3. Light Collection

The light collection approach used to reconstruct the laser energy differs from the standard offline as explained in 4.3.1. April 2004 CLF data have been reconstructed using both approaches. In figure 5.14 the distribution of the percentual difference between the two approaches is shown.

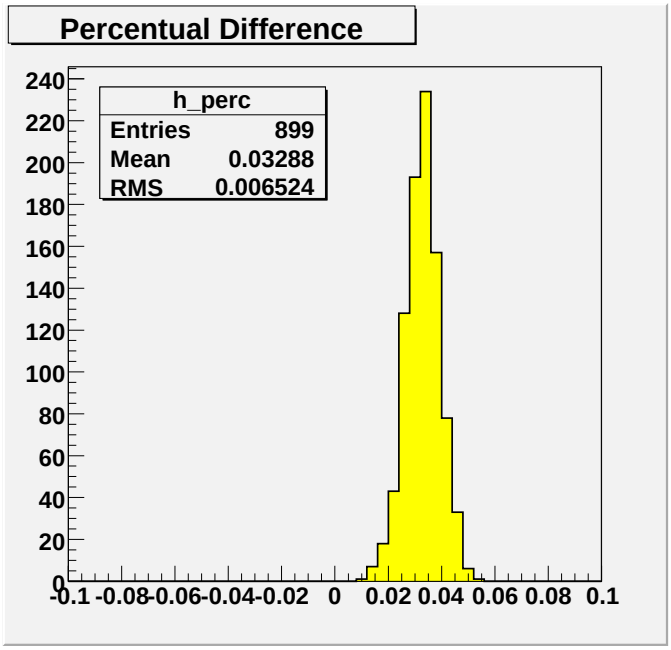

Figure 5.14: Distribution of percentual difference between the two light collection approaches.

The two approaches differ by ~ 3 %; the difference is small, and however the use of the standard light collection would even enhance the observed energy deficit. In conclusion, the origin of the lack of energy cannot be explained as due to the use of the different light collection module.

5.5 Estimating the energy deficit and validation of the parametric approach

In order to quantify the energy deficit, a gaussian fit for each CLF epoch was applied to the reconstructed/nominal energy distribution and the mean value computed. Results for Eye1 and Eye4 are reported in table 5.9.

	epoch 1	epoch 2	epoch 3	epoch 4	epoch 5	epoch 6	epoch 7	epoch 8
Los Leones (Eye1)	0.85	1.14	N.A.	0.88	0.77	0.90	0.89	N.A.
Coihueco (Eye4)	0.86	1.28	N.A.	0.87	0.81	0.89	0.85	N.A.

Table 5.9: Results of the constant fit applied to the plot of the reconstructed vs nominal CLF energy from Eye1 and Eye4, as in figures 5.8, 5.9. No results are reported for epoch 8 since the aersol database is not yet available for the last epoch.

As already explained, old calibration constants are used in epoch 1; the same deficit ($\sim 13\%$) is observed in epochs 4, 6 and 7. A greater lack of energy is observed in epoch 5. The same features are also visible from Coihueco, as seen in figure 5.9. The extra observed deficit in epoch 5 is most probably due to an incorrect CLF calibration (still within quoted systematics) in that epoch. Regardless of this interpretation, the energy loss estimates can be used to rescale all reconstructed profiles. Rescaled profiles can be used to compare the performances of the two approaches.

Once the fit result ψ has been evaluated for each epoch, a correction can be applied to the amount of photons of real profiles:

$$N^{\gamma}_{corrected} = N^{\gamma} \times \psi$$

The Laser Simulation method was applied to the "corrected" profiles. In figure 5.15 the correlation between Utah and this analysis is shown.

The excellent correlation between the two analyses indicates that the parametric model adopted for the description of the aerosol concentration can very accurately describe the Malargüe atmosphere. If a proper normalization is found, VAODs obtained by this analysis can be safely incorporated in the Aerosol Database and used for physics analysis.

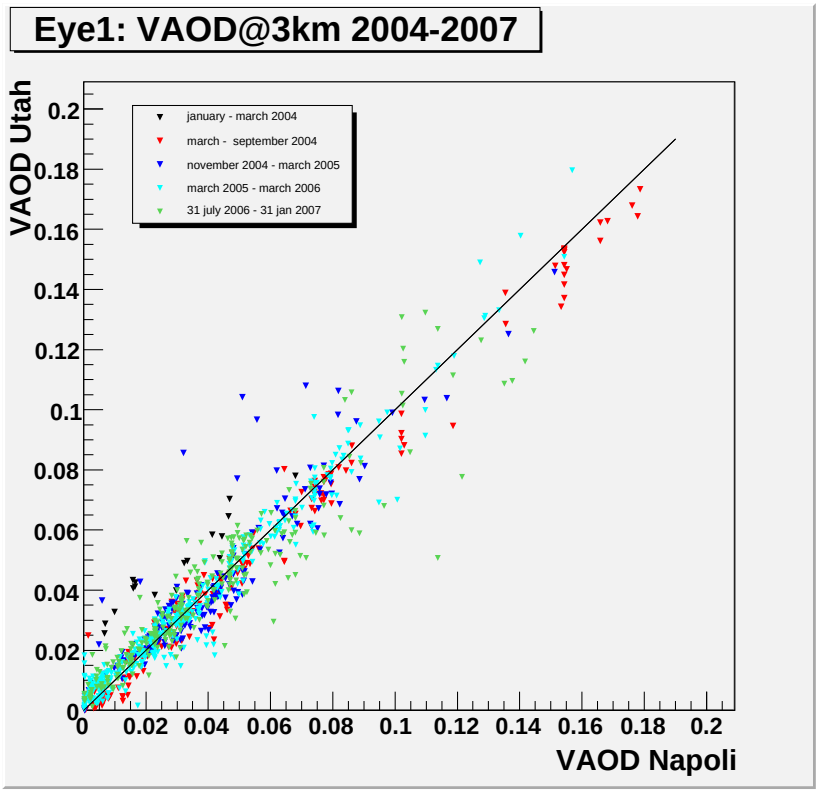

Figure 5.15: Correlation between Laser Simulation (Napoli) and Data Normalized (Utah) methods. Real CLF profiles are corrected by the energy deficit estimated for each epoch.

5.6 Normalization to a Rayleigh night

The observed energy deficit independently from its origin (FD calibrations or simulation systematics) affects the determination of the aerosol concentration. The only solution is to find a normalization point for each epoch that fixes the correct energy scale.

The idea is to normalize data to a reference clear night in which the aerosol concentration can be neglected (i.e., a *"Rayleigh night"*). In a non Rayleigh night the number of reconstructed photons depends both on the aerosol attenuation and on FD and CLF calibrations, so it is not possible to distinguish the contribution from each factor. On the other hand, in a Rayleigh night, since the aerosol absorption can be neglected, the ratio between reconstructed and nominal energy returns the normalization constant that fixes the energy scale. This procedure is repeated for each CLF epoch.

Real average profiles (groups of 50 shots in 15 minutes) are then scaled by dividing the number of photons in each bin by the normalization constant of the corresponding epoch. The Laser Simulation method is finally applied to the normalized profiles.

5.6.1 Rayleigh Night Search

The identification of a Rayleigh night is mainly based on the analysis of clean profiles shape. In principle the identification can be done purely on the shape, independently from the normalization; in the real application, since the cleanest is the atmosphere, the closest are the profiles, and since event to event fluctuations are always present, this search is not at all easy and the number of photons (i.e. the profile integral) may help. The shape of the Rayleigh night is returned by a simulation.

A 50 shots average Rayleigh profile is generated fixing the aerosol parameters and the energy E = 6.5 mJ. The procedure is repeated 12 times using the appropriate monthly density profiles to take into account seasonal variations of density, temperature and pressure.

All real average profiles normalized at 6.5mJ are compared to the appropriate simulated Rayleigh profile. The method chosen for the comparison is the unnormalized Kolmogorov test as available in the ROOT package, that returns the probability that the analyzed profile is compatible to the Rayleigh one (*KolmoProbability*) on the basis of shapes only, without taking into account the normalization.

For each profile the *KolmoProbability* and the ratio between the total number of photons of the real profile with respect to that of the Rayleigh one (*IntegralsRatio*) are returned.

In each CLF epoch, the search for the Rayleigh night is performed among profiles having high values of both parameters. A search region was defined, whose lower bounds *MinIntegralRatio* and *MinKolmoProbability* are evaluated extracting the mean value and the RMS of the distribution of the two parameters:

$$MinIntegralRatio = < \text{Integral} > + \sigma(\text{Integral})$$

$$MinKolmoProbability = < \text{KolmoProbability} > + \sigma(\text{KolmoProbability})$$

Profiles belonging to the search region are grouped by day. Nightly averages for *Night-KolmoProbability* and *Night-IntegralsRatio* are computed.

A list of candidate clean nights with associated probability and number of profiles is produced.

There is not a unique criterium to identify the reference night in the selected sample: it is not even guaranteed that a Rayleigh night is present in each epoch. Several combinations of cuts on the available parameters were tested. The final choice was to select the night with the highest *Night-KolmoProbability* and at least 4 profiles, when available, to avoid fluctuations.

In table 5.10 an example of list of candidate clean nights with the chosen one highlighted is shown.

	Night-KolmoProbability	Night-IntegralsRatio	Nprofiles
1	0.0803373	0.942184	8
2	0.00138787	0.828468	5
3	0.0809879	0.862189	14
4	**0.0856664**	**0.904196**	**22**
5	6.13683e-05	0.917536	1
6	0.000206988	0.84464	2

Table 5.10: Example list of clean nights. The chosen reference night is highlighted.

The *Night-IntegralsRatio* of the reference night is used to rescale the number of photons of real profiles before measuring the aerosol concentration. In figure 5.16 the Eye1 simulated Rayleigh profile of december together with the selected reference real profile before and after the normalization is shown. The different normalization between uncorrected (green) and corrected (red) profiles is due to the energy loss.

The lists of Rayleigh reference nights for each epoch as obtained by this analysis are summarized in the following tables for Eye 1 and Eye4:

EYE1	Rayleigh Night	Normalization
Epoch 1	-	0.85
Epoch 2	april 21 2004	1.14
Epoch 4	december 18 2004	0.90
Epoch 5	july 5 2005	0.77
Epoch 7	april 10 2007	0.82
Epoch 8	june 17 2007	0.84

Table 5.11: Eye1 list of Rayleigh nights obtained by this analysis.

In epoch 1 no Rayleigh nights were found. The result for the cleanest night is reported.

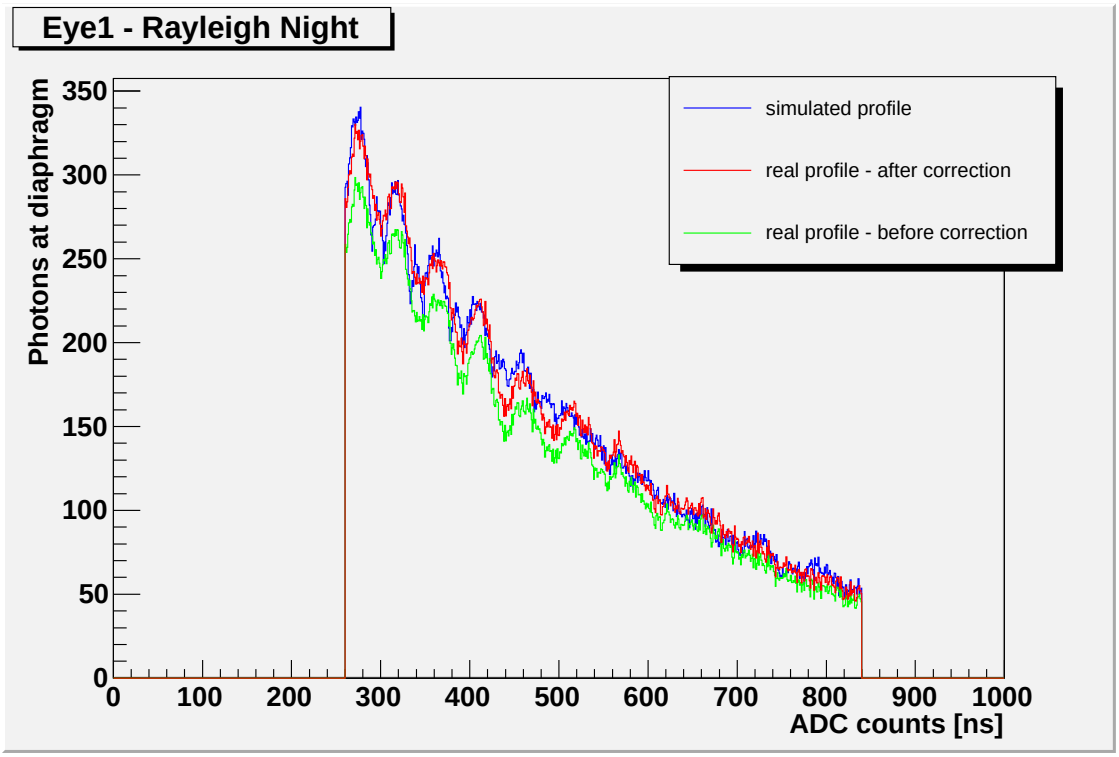

Figure 5.16: Simulated Rayleigh profile from Eye1 (blue profile) together with the chosen Rayleigh night before (green) and after (blue) the normalization.

EYE4	Rayleigh Night	Normalization
Epoch 1	-	0.86
Epoch 2	august 09 2004	1.21
Epoch 4	december 12 2004	0.94
Epoch 5	august 02 2005	0.83
Epoch 7	october 14 2006	0.81
Epoch 8	july 11 2007	0.82

Table 5.12: Eye4 list of Rayleigh nights obtained by this analysis.

5.6.2 VAOD(z) systematic errors

The normalization makes the whole procedure independent from CLF/FD calibration systematics, that in case of a purely MonteCarlo normalized analysis are dominating. Systematic errors are basically due to the indetermination in the choice of the Rayleigh night ($\text{RaylNight}_{\text{Sys}}$). As already said, several combinations of cuts were tested: the variation of the *NightIntegralsRatio* returned by the different combinations is always below 5%.

Basically the same energy variation is found when comparing Rayleigh nights from this approach with the one selected by Utah group. To get an estimate of this effect, the VAOD versus height curves obtained by the two analyses were compared. Typically the two approaches agree within 4% up to several km in height. This indetermination must be combined with the uncertainty due to the parametric model adopted in this analysis to describe the aerosol profile ($\mathrm{ParModel_{Sys}}$).

Figure 5.17 shows a typical situation.

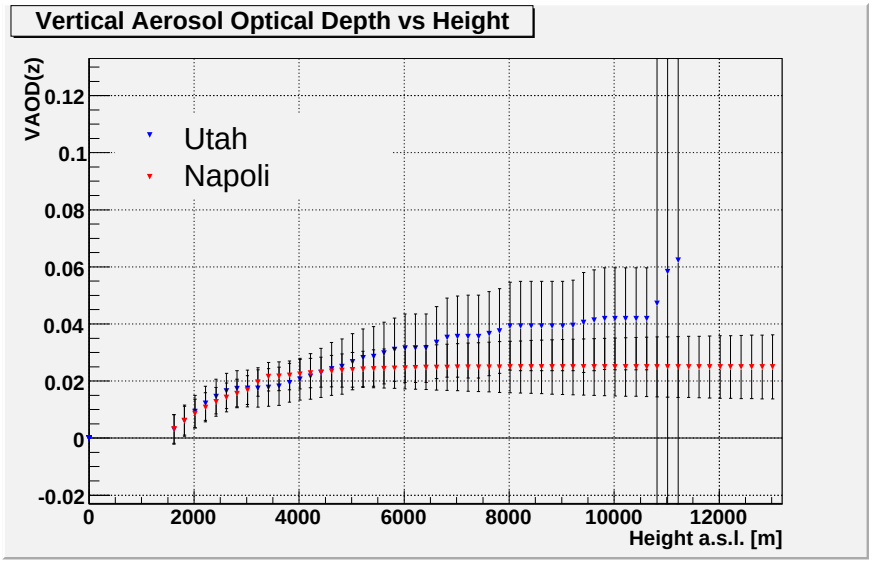

Figure 5.17: Comparison of the same VAOD profile with height as obtained with Naples (red) and Utah (blue) analyses. Error bars at 4% are shown for the Laser Simulation method.

The two profiles are compatible within $\sim 4\%$; an increasin discrepancy is observed. This seems to be connected to an unphysical behaviour of the Utah analysis, happening in a few cases: above a few km the aerosol concentration should drop to zero and consequently the VAOD(z) should tend to a constant value. In some cases Utah analysis doesn't seem to follow this expected trend with height. If the compatibility test is performed only in the first part of the two profiles, the conclusion is that the systematics introduced by the use of a parametric model is within 4%.

The total systematic error associated to VAOD(z) is:

$$\Delta^{\mathrm{Sys}}_{\mathrm{VAOD}} = \sqrt{(\mathrm{RaylNight_{Sys}})^2 + (\mathrm{ParModel_{Sys}})^2}$$

According to the procedure explained in section 5.1.1, the combination

of a 5% indetermination on the choice of the Rayleigh Night with a 4% indetermination due to the aerosol parametric model adopted corresponds to a total systematic error on VAOD@3km of 0.009.

5.7 Results

Utah - Naples comparison

The correlation of the VAOD results of Utah analysis with the results of this procedure, obtained appling normalizing data to the Rayleigh night chosen for each epoch, is shown in figure 5.18.

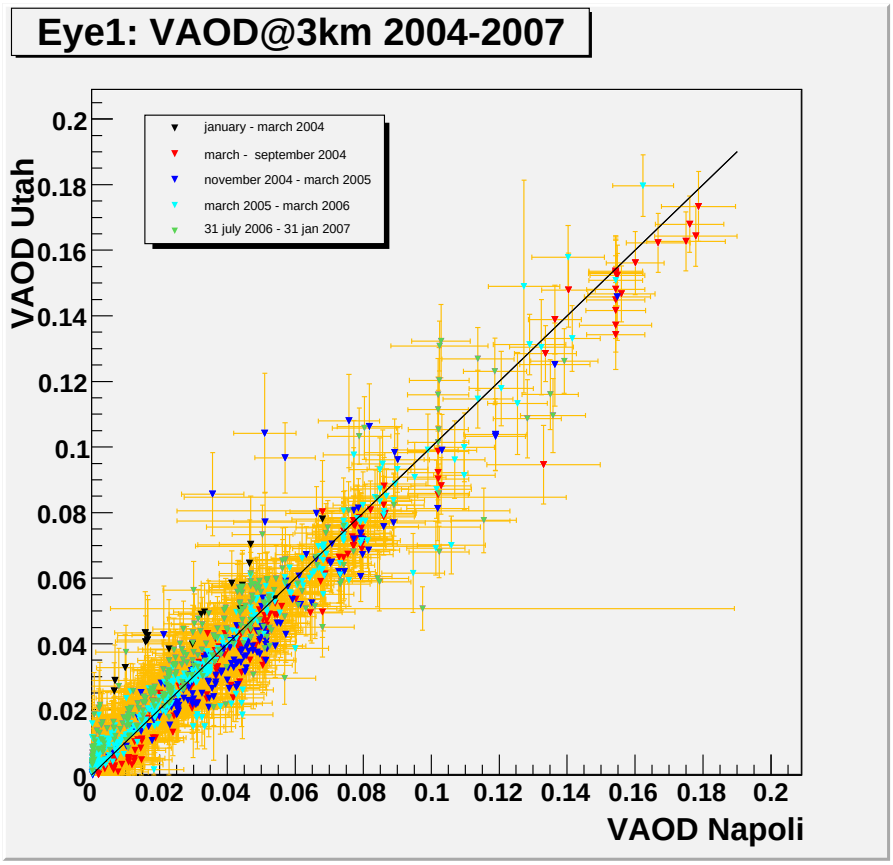

Figure 5.18: Correlation between Laser Simulation (Napoli) and Data Normalized (Utah) methods. The Rayleigh Night normalization is applied.

Taking into account that the two analyses are completely independent, the correlation shown is striking. It proves the reliability of the parametric aerosol model adopted and the validity of the method used.

In figure 5.19 the VAOD@3km distribution resulting from this analysis compared to the VAOD@3km distribution obtained by Utah analysis is shown. The comparison is performed on the same data sample of figure 5.18.

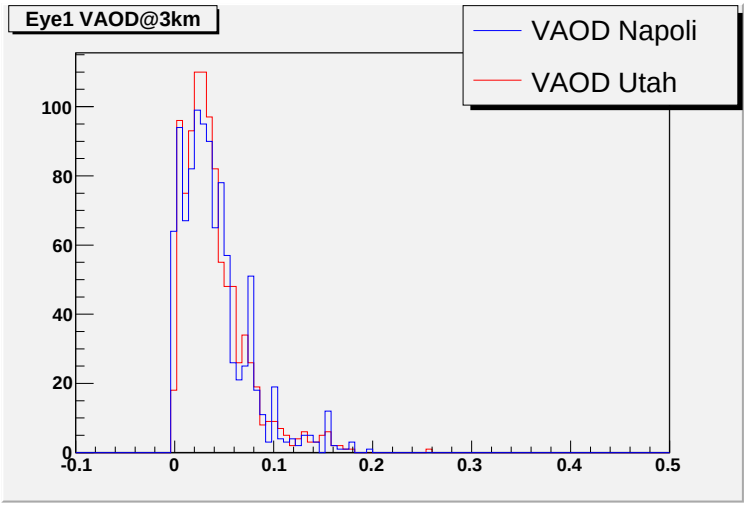

Figure 5.19: Distribution of VAOD@3km on 3 years of data as obtained with the Naples analysis (red) and Utah analysis (blue).

In figure 5.20 the result for the aerosol extinction α@3km as resulting from equation 4.1 is shown.

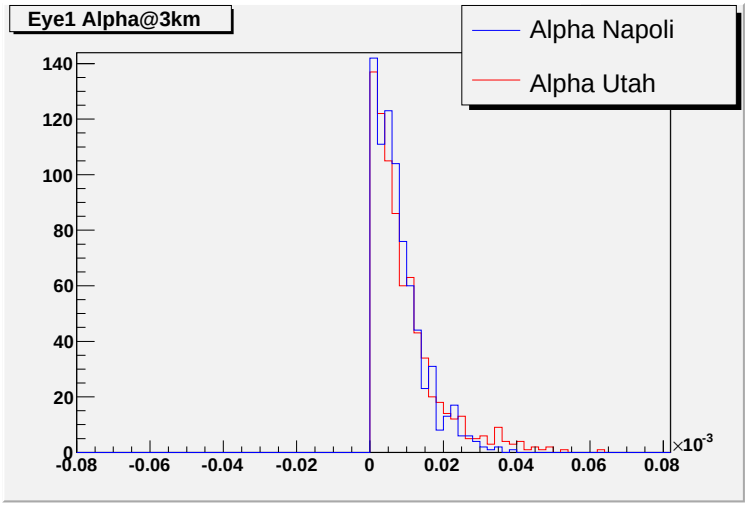

Figure 5.20: Distribution of α@3km on 3 years of data as obtained with the Naples analysis (red) and Utah analysis (blue).

Both VAOD@3km and α@3km distributions are perfectly compatible with those obtained by Utah analysis.

VAOD vs height

In the following, the results as a function of the height are presented. In figure 5.21, an example of a typical VAOD(z) profile is shown.

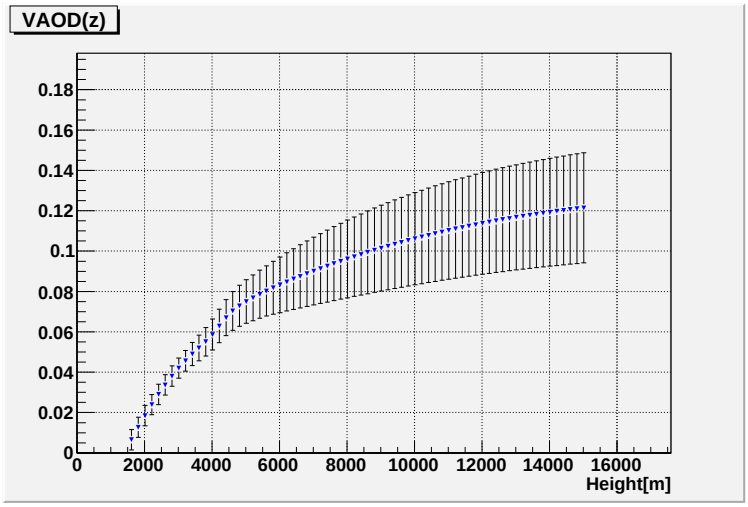

Figure 5.21: Example of VAOD profile with height.

The profile is obtained by the composition of all the quarter-hour profiles available in the hour. This explaines the not perfectly exponential shape in some hourly VAOD profiles. As an example, the profile shown in figure 5.21 is obtained by the composition of the three profiles shown in figure 5.22:

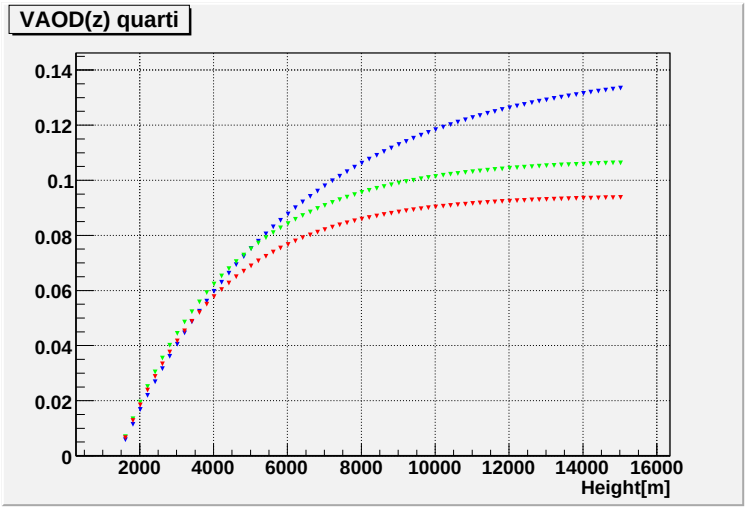

Figure 5.22: Three quarter-hour profiles composing the profile of figure 5.21.

LIDAR - Naples comparison

The correlation with another independent analysis is presented: the preliminary results obtained by Torino group for the Los Leones LIDAR are compared to the results of this analysis. In figure 5.23 results for eye1 from january 2007 to august 2007 are shown. The parameter chosen for the comparison is as usual the VAOD@3km (4.5 km a.s.l.).

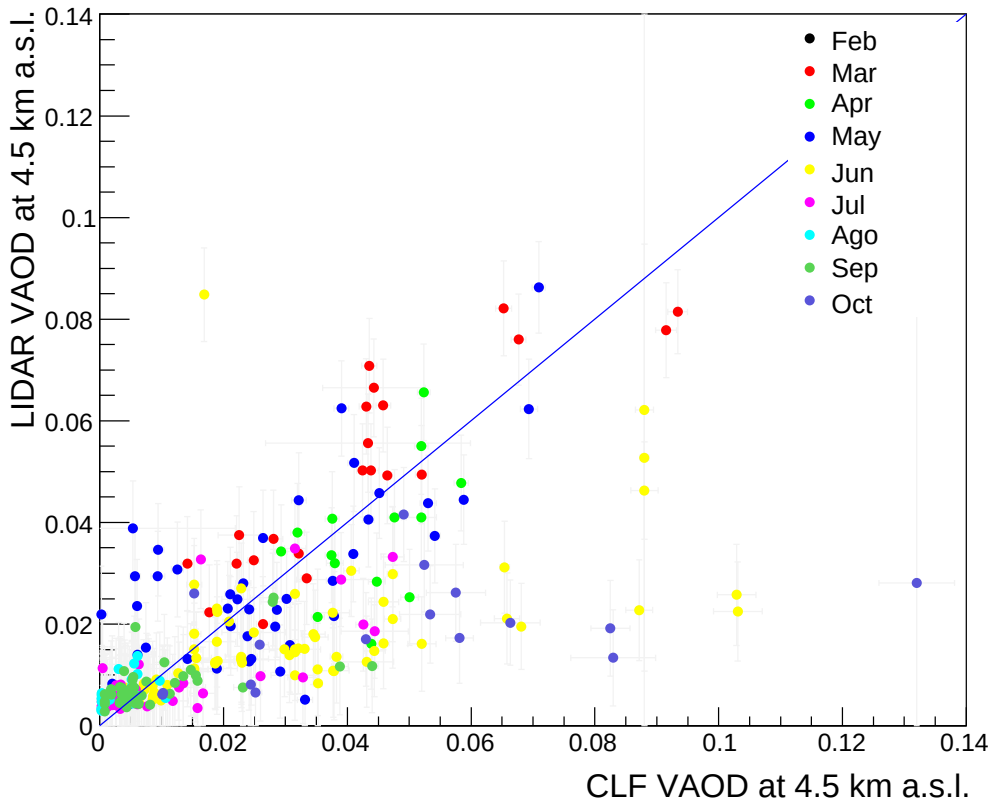

Figure 5.23: The correlation between 2007 VAOD@3km obtained with the analysis of Los Leones LIDAR data by Torino group and this analyis.

The larger spread of the points in this comparison is probably due to the fact that the two devices sample different atmospheric sections. In fact, this analysis is looking at the portion of atmosphere between the CLF and FD buildings, while the LIDARs look at the sky in different regions. In case of horizontal uniformity, the two analyses should return the same aerosol concentration.

In figure 5.24 the distribution of VAOD@3km for the two analyses is shown.

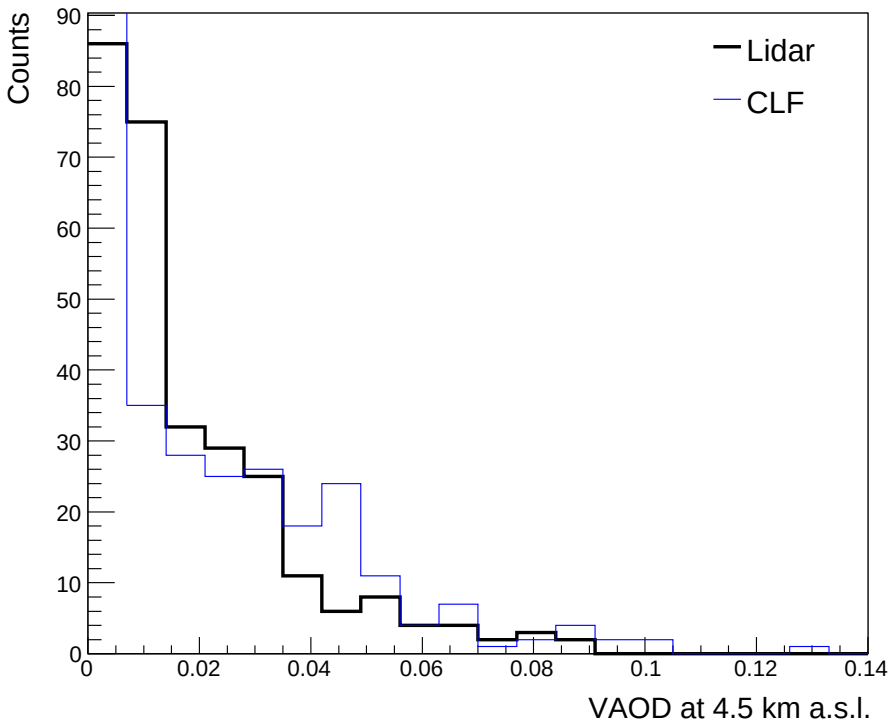

Figure 5.24: The distribution of 2007 VAOD@3km obtained with the analysis of Los Leones LIDAR data by Torino group and this analyis.

5.8 Conclusions

In figures 5.25 and 5.26 Eye1 and Eye4 VAOD@3km as a function of time as obtained with Utah and Naples analyses are shown: the most striking feature is the observable seasonal variation, in particular the decrease in the june-august period of each year, proving that the cleanest season is winter. In the plot are also reported the total number of only-Naples hourly results (1000, blue dots), of only-Utah hourly results (872, red dots) and finally of coincidence hourly results (1011, green dots). Only-Utah results are mainly due to the presence of clouds, because this analysis rejects data in cloudy nights.

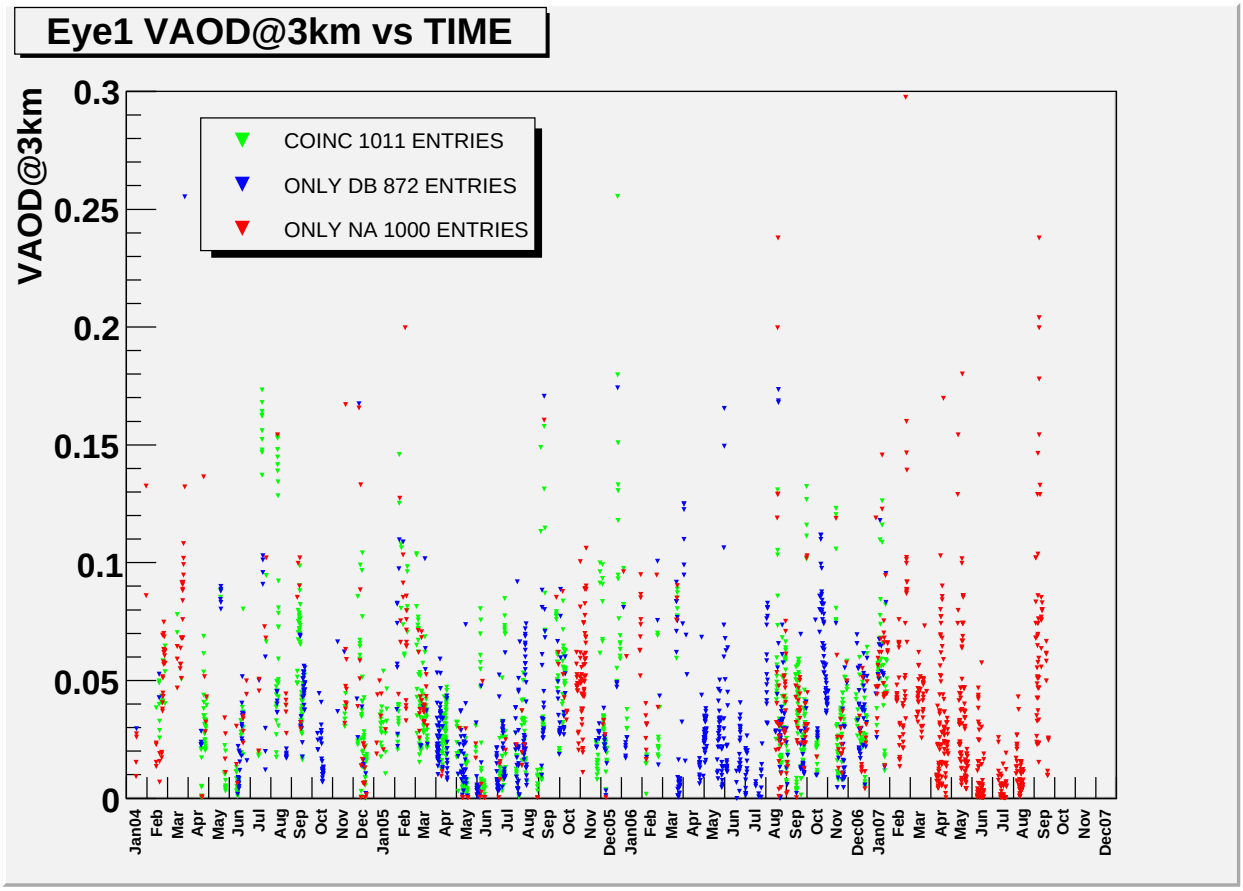

Figure 5.25: Eye1 VAOD@3km vs time. Seasonal variations are observed. Blue dots are for only-Utah results; red dots are for only-Naples results; green dots are for coincidence results.

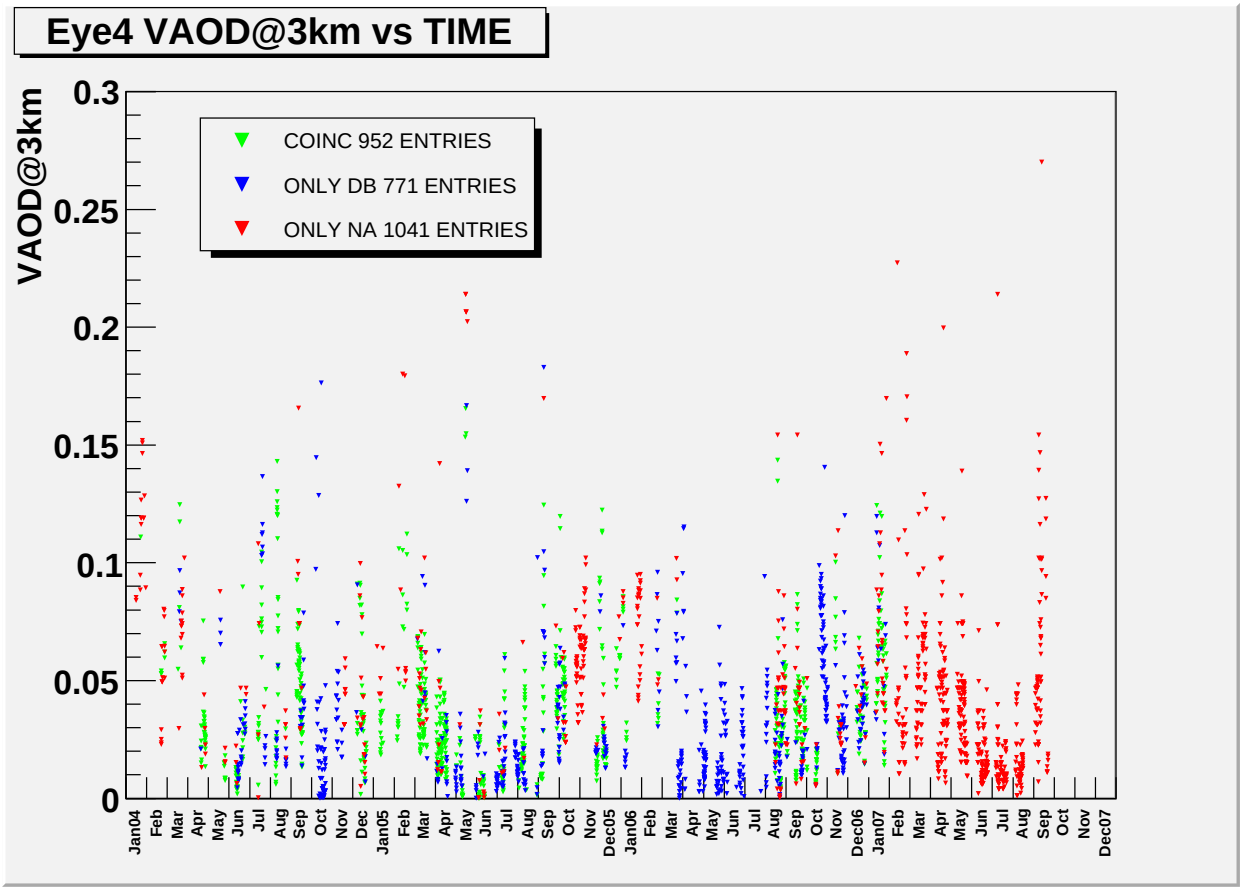

Figure 5.26: Eye4 VAOD@3km vs time.Seasonal variations are observed. Blue dots are for only-Utah results; red dots are for only-Naples results; green dots are for coincidence results.

Hourly results are recorded in DB-like files organized as follows: the first line is the GPS time, the second is the maximum height of the analysis, the other rows are: $\alpha(z)$, $\alpha_{\min}(z)$, $\alpha_{\max}(z)$, VAOD(z), $\text{VAOD}_{\min}$(z),$\text{VAOD}_{\max}$(z).

848196013						
15016.2	15016.2					
1616.2	2.39125e-05	1.64125e-05	3.14125e-05	0.00519957	0.000179941	0.0102192
1816.2	2.03641e-05	9.75753e-06	3.09707e-05	0.00960762	0.00400948	0.0152058
2016.2	1.76845e-05	7.07793e-06	2.82911e-05	0.0133547	0.00609283	0.0206167
2216.2	1.42531e-05	3.64646e-06	2.48597e-05	0.0165568	0.00818769	0.0249258
2416.2	1.17971e-05	1.1905e-06	2.24037e-05	0.0193207	0.0102861	0.0283553
2616.2	9.9617e-06	0	2.05683e-05	0.0217515	0.0124	0.0311029
2816.2	8.40141e-06	0	1.9008e-05	0.0239509	0.014538	0.0333639
3016.2	7.08163e-06	0	1.76882e-05	0.0259506	0.0166069	0.0352944
3216.2	5.96548e-06	0	1.65721e-05	0.0274424	0.0181604	0.0367244
3416.2	5.02283e-06	0	1.56294e-05	0.0279896	0.0186741	0.0373051
3616.2	4.22753e-06	0	1.48341e-05	0.0281844	0.0188393	0.0375295
3816.2	3.55705e-06	0	1.41636e-05	0.0285343	0.019224	0.0378446
4016.2	2.99214e-06	0	1.35987e-05	0.0289843	0.0197558	0.0382128
4216.2	2.51642e-06	0	1.3123e-05	0.0294371	0.0203234	0.0385509
4416.2	2.11598e-06	0	1.27226e-05	0.0298515	0.0208756	0.0388274
4616.2	1.77903e-06	0	1.23856e-05	0.0302168	0.0213945	0.0390391
4816.2	1.49558e-06	0	1.21022e-05	0.0305356	0.0218771	0.039194
5016.2	1.25721e-06	0	1.18638e-05	0.030816	0.0223273	0.0393047
5216.2	1.05679e-06	0	1.16634e-05	0.0310686	0.0227521	0.0393851
.....						
14016.2	6.10109e-10	0	1.06072e-05	0.0327497	0.0210062	0.0444932
14216.2	5.17647e-10	0	1.06071e-05	0.0327498	0.0209387	0.044561
14416.2	4.39272e-10	0	1.0607e-05	0.03275	0.0208745	0.0446254
14616.2	3.72823e-10	0	1.0607e-05	0.03275	0.0208132	0.0446869
14816.2	3.16476e-10	0	1.06069e-05	0.0327501	0.0207548	0.0447454
15016.2	2.68685e-10	0	1.06069e-05	0.0327502	0.0206992	0.0448011

Table 5.13: Example of VAOD database file.

This analysis have produced results for 3.7 years of data taking; hourly database-like files have been produced, that will be incorporated in the present aerosol database, in order to integrate data in the common Utah-Naples period (from january 1^{st} 2004 to january 31^{st} 2007) and to add data from february 1^{st} 2007 to september 30^{th} 2007, when there are presently no data in the database and this analysis provides the only available results.

Conclusions

The Fluorescence Detector of the Auger experiment provides a very datailed picture of the development of Extensive Air Showers in the atmosphere. This is fundamental to extract the average composition of the primaries through the measurement of the atmospheric depth of the maximum of the shower development, and to measure the energy in a calorimetric, model independent way. Moreover FD energy is used to calibrate the energy scale of the Surface Detector. The measurement of the aerosol attenuation of the fluorescence light produced by a shower in atmosphere during its travel from the emission point to the detector is fundamental to obtain a reliable FD estimation of the shower energy.

During my PhD activity, I set up an analysis strategy to determine the aerosol attenuation in the atmosphere. The procedure, based on a parametric model of the aerosol stratification, makes use of vertical laser tracks provided by the Central Laser Facility of the Auger Experiment. The procedure is named "Laser Simulation Method", since the aerosol attenuation is evaluated by means of a comparison between real and simulated profiles of light collected at the aperture of the Fluorescence Telescopes as a function of the height.

A first application of the method showed a difference in the average Vertical Aerosol Optical Depth at 3 km produced in different CLF epochs; this suggested the presence of hidden systematics, that could also affect the energy reconstruction of CLF events. To check if this were the case, a systematic study of CLF energy reconstruction was performed. Energy analysis confirms epoch related features and puts in evidence an energy deficit starting from december 2004 data. The conclusion is that the aerosol concentration estimated with the Laser Simulation method is at the moment affected by systematics that must be still understood. To measure the aerosol concentration with this procedure, a normalization is needed for each epoch. I normalized data by means of a reference extremely clear night in which the aerosol concentration can be set to zero (i.e. *"Rayleigh night"*): the ratio between reconstructed and nominal energy returns the normalization constant

needed to fix the energy scale.

The analysis was performed on january 2004 - september 2007 data from 2 out of 4 eyes (Los Leones and Coihueco), providing hourly values of the fluorescence light attenuation due to atmospheric aerosols. The VAOD@3km time behaviour presents clear features of seasonal variations, both from Los Leones and from Coihueco.

The comparison of my results with those obtained by Utah group, presently providing values for the Aerosol Database of the Auger Observatory, is extremely good. Both the correlation and the distributions of VAOD@3km and of the Aerosol Extincion α@3km are in perfect agreement, proving also the reliability of the parametric model adopted to describe the atmosphere above the Auger Observatory site. Also the comparison with the preliminary results by Torino group on Los Leones LIDAR data is good.

Since february 2007 my analysis provides the only available results for the aerosol attenuation: the aerosol database of the Auger Observatory will be soon integrated with these values; moreover, the leaks in the database due to failures in the Utah analysis will be completed with my results.

Further improvements to this analysis will be soon performed. An algorithm will be implemented in order to analyze profiles in presence of clouds, providing results up to the height of the observed cloud. This analysis strategy will be also applied to Los Morados and Loma Amarilla CLF data. As soon as XLF2 will be operative, the measurement of the aerosol attenuation will be performed with this independent device, allowing a cross check of the results obtained by the same FD eyes with different laser facilities. Moreover, the systematic study of XLF2 energy reconstruction will help in understanding the origin of the hidden systematics. As soon as systematics will be properly understood, and hopefully the origin of the deficit solved, the Laser Simulation Method will be performed without the normalization to the Rayleigh Night.

A proper understanding of the energy systematics is needed not only for my analysis, since it is crucial to determine the energy scale, and changing the energy scale would imply a change in the maximum distance of expected sources. This “horizon of events” should be closer in case of an underestimation of the energy.

Bibliography

[1] V. Hess, *Phys. Zeit*, **13**, (1912) 1084.

[2] P. Auger, R. Maze and T. Grivet-Meyer, *Comptes rendus de l'Academie des Science*, **206**,(1962) 1721.

[3] D.J. Bird et al., *Phys. Rev. Lett.*, **71** 3401-3404 (1993)

[4] R. U. Abbasi, *Phys. Lett.*, **B619** 271-280 (2005)

[5] J.R. Hörandel, *Astropart. Phys.*, **21**, 241 (2004); G. Sigl, *arXiv:astro-ph/0404074v1.*

[6] P. Sokolsky (1989): "Introduction to Ultrahigh Energy Cosmic Ray Physics", Addison-Wesley Publishing

[7] A.A. Penzias & R.W. Wilson, *Ap. J.*, **142**, (1965) 419.

[8] K. Greisen, *Phys. Rev. Lrtters*, **16**, (1966) 748.

[9] G.T. Zatsepin & V.A. Kuz'min, *JETP Letters*, **4**, (1966) 78.

[10] R. Aloisio, V. Berezinsky, P. Blasi and S. Ostapchenko, *ArXiv astro-ph* 0706.2834.

[11] R.J. Protheroe and P. Johnson, *Astropart. Phys.*, **4**, 253 (1996).

[12] F.W. Stecker and M. Salamon, *ApJ*, **512**, 521 (1999).

[13] R.J. Protheroe and R.W. Clay, *arXiv:astro-ph/0311466v1.*

[14] S. Karakula and W. Tkaczyk, *Astropart. Phys.*, **1**, 229 (1993).

[15] V.S. Berezinsky and S.I. Grigor'eva, *Astron. Astrophys.*, **199**, 1 (1988).

[16] O.E. Kalashev, V.A. Kuzmin, D.V. Semikoz, I.I. Tkachev, *arXiv:astro-ph/0107130.*

[17] S. Yoshida, *Astropart. Phys.*, **2**, 187 (1994).

[18] T. Weiler, *Phys. Rev. Lett.*, **49**, 234 (1982).

[19] T. Weiler, *Astrophys. J.*, **285**, 495 (1984).

[20] E. Fermi, *Phys. Rev.*, **75**, (1949) 1169.

[21] P. Blasi, E. Amato, arXiv: 0706.1714

[22] A.M. Hillas, *Ann. Rev. Astron. Astrophys.*, **22**, 425 (1984).

[23] C.T. Hill, *Nucl. Phys. B*, **224**, 469 (1983).

[24] C.T. Hill, D.N. Schramm and T.P. Walker, *Phys. Rev. D*, **36**, 1007 (1987).

[25] P. Bhattacharjee, *Phys. Rev. D*, **40**, 3968 (1989).

[26] P. Bhattacharjee and N.C. Rana, *Phys. Lett. B*, **246**, 365 (1990).

[27] P. Bhattacharjee, C.T. Hill and D.N. Schramm, *Phys. Rev. Lett.*, **69**, 567 (1992).

[28] P. Bhattacharjee and G. Sigl, *Phys. Rev. D*, **51**, 4079 (1995), *arXiv:astro-ph/9412053*.

[29] P. Gondolo, G. Gelmini and S. Sarkar, *Nucl. Phys. B*, **392**, 111 (1993), *arXiv:hep-ph/9209236*.

[30] V. Berezinsky, M. Kachelriess and A. Vilenkin, *Phys. Rev. Lett.*, **79**, 4302 (1997), *arXiv:astro-ph/9708217*.

[31] V.A. Kuzmin and V.A. Rubakov, *Phys. Atom. Nucl.*, **61**, 1028 (1998), *Yad. Fiz.*, **61**, 1122 (1998), *arXiv:astro-ph/9709187*.

[32] V.A. Kuzmin and I. Tkachev, *JETP Lett.*, **68**, 271 (1998), *arXiv:hep-ph/9802304*.

[33] T.W. Kephart and T.J. Weiler, *Astropart. Phys.*, **4**, 271 (1996), *arXiv:astro-ph/9505134*.

[34] S. Bonazzola and P. Peter, *Astropart. Phys.*, **7**, 161 (1997), *arXiv:hep-ph/9701246*.

[35] P. Bhattacharjee and G. Sigl, *Phys. Rep.*, **327**, 109 (2000), *arXiv:astro-ph/9811011*.

[36] P. Bhattacharjee, *arXiv:astro-ph/9803029*.

[37] V.A. Kuzmin and I. Tkachev, *Phys. Rept.*, **320**, 199 (1999), *arXiv:hep-ph/9903542*.

[38] V. Berezinsky, *Nucl. Phys. Proc. Suppl.*, **81**, 311 (2000).

[39] A.V. Olinto, *Phys. Rept.*, **333**, 329 (2000), *arXiv:astro-ph/0002006*.

[40] P. Bhattacharjee and G. Sigl, *Lect. Notes Phys.*, **576**, 275 (2001).

[41] W. Heitler, *The Quantum Theory of Radiation*, Oxford University Press, London, (1944).

[42] A.N. Bunner, PhD Thesis, Cornell University, Ithaca, NY, USA (1967).

[43] R.W. Nicholls, E.M. Reeves and D.A. Bromley, *Proc. Phys. Soc.*, **74**, 87 (1959).

[44] R.H. Hughes et al., *Phys. Rev.*, **123**, 2084 (1961).

[45] E.C. Flowers & R.A. McCormick & K.R. Kurfis,

[46] L. Elterman & R.B Toolin,

[47] F.I. Boley, *Rev. Mod. Phys.*, **36**, 792 (1964).

[48] K. Greisen, *Ann. Rev. Nucl. Sci.*, **10**, 63 (1960).

[49] W. Galbraith and J.V. Jelley, *Nature*, **171**,

[50] R.M. Baltrusaitis et al.,*Nucl. Inst. Methods* **A240**, 410 (1985).

[51] http://www.mpi-hd.mpg.de/hfm/HESS/HESS.html

[52] M. Takeda et al., *Phys. Rev. Lett.*, **81**, 1163 (1998).

[53] M. Takeda et al., *Astrophys. J.*, **522**, 225 (1999).

[54] M. Takeda et al., *Astropart. Phys.*, **19**, 447 (2003).

[55] D.J. Bird et al., *Phys. Rev. Lett.*, **71**, 3401 (1993).

[56] D.R. Bergman, HiRes Collaboration: Proc. 30^{th} ICRC (Mérida, México) 2007.

[57] A.A. Watson, *arXiv:astro-ph/0112474*.

[58] The P.AUGER Collaboration, *Nucl. Phys. B (Proc. Suppl.)*, **85**, 324 (2000).

[59] K. Green, J.L. Rosner, D.A. Suprun, and J.F. Wilkerson, *Nuclear Instruments and Methods in Physics Research*, **A498**, (2003) 256-288; H. Falcke et al. [LOPES Collaboration], *Nature*, **435**, (2005) 313-316; D. Ardouin et al. [CODALEMA Collaboration], *Nuclear Instruments and Methods in Physics Research*, **A555**, (2005) 148-163.

[60] Nagano et al., *Astropart. Phys.* **22**, 235 (2004)

[61] M. Roth, Pierre Auger Collaboration: Proc. 30$^{\text{th}}$ ICRC (Mérida, México) 2007.

[62] P. Facal, Pierre Auger Collaboration: Proc. 30$^{\text{th}}$ ICRC (Mérida, México) 2007.

[63] L. Perrone, Pierre Auger Collaboration: Proc. 30$^{\text{th}}$ ICRC (Mérida, México) 2007.

[64] N. Hayashida et al. [AGASA Collaboration], *Phys. Rev. Lett.*, **77**, (1996) 1000; M. Teshima at al. [AGASA Collaboration], *Proc. 27th International Conference on Cosmic Rays*, **1**, 337 (2001).

[65] U. Abbasi et al.[The Hires Collaboration], *Astrophys. J.*, **610**, (2004) L73.

[66] T. Stanev, P.L. Biermann, J. Lloyd-Evans, J.P. Rachen and A.A. Watson, *Phys. Rev. Lett.*, **75**, (1995) 3056; Y. Ulchihori, M. Nagano, M. Takeda, M. Teshima, J. Lloyd-Evans and A.A. Watson, *Astropart. Phys.*, **13**, (2000) 151; A. Cuoco, G. Miele and P.D. Serpico, astro-ph-07062864v1.

[67] The Pierre Auger Collaboration, *Science*, **318**, (5852) 938.

[68] M.-P. Véron-Cetty and P. Véron *Astron. & Astrophys.*, **455**, (2006) 773.

[69] M. Unger, Pierre Auger Collaboration: Proc. 30$^{\text{th}}$ ICRC (Mérida, México) 2007

[70] N. Hayashida et al. [AGASA Collaboration], *Astropart. Phys.*, **10**, (1999) 303.

[71] J. Abraham et al. [P.AUGER Collaboration], *Astropart. Phys.*, **27**, (2007) 155.

[72] M. Healy, Pierre Auger Collaboration: Proc. 30$^{\text{th}}$ ICRC (Mérida, México) 2007.

[73] G. Gelmini, O.E. Kalashev, D.V. Semikoz, *ArXiv astro-ph* 0506.128; J. Ellis, V. Mayes, D.V. Nanopoulos, *Physical Review D*, **74**, (2006) 115003.

[74] k. Shinozaki et al. [AGASA Collaboration], *Astrophysical Journal*, **571**, (2002) L117.

[75] M. Risse et al., *Physical Review Letters*, **95**, (2005) 171102.

[76] M. Ave et al., *Physical Review Letters*, **85**, (2000) 2244.

[77] A.V. Glushkov et al., *ArXiv astro-ph* 0701.245.

[78] J. Alvarez-Muñiz, Pierre Auger Collaboration: Proc. 30$^{\text{th}}$ ICRC (Mérida, México) 2007.

[79] O. Blanch Bigas, Pierre Auger Collaboration: Proc. 30$^{\text{th}}$ ICRC (Mérida, México) 2007.

[80] A.A. Watson, *Elsevier Science*, **13**, (1912) 1084.

[81] radio detection aaaa

[82] M.A. Laurence & R.J.O. Reid & A.A. Watson, *J. Phys. G*, **17**, (1991) 773.

[83] R.M. Baltrusaitis et al.,*Nucl. Inst. Methods* **A240**, 410 (1985).

[84] K. Greisen, *Prog. Cosmic Ray Physics*, **3**, (1956) 1.

[85] J. Nishimura & K. Kamata, *Prog. Theor. Phys.*, **5**, (1950) 899.

[86] J. Nishimura & K. Kamata, *Prog. Theor. Phys.*, **6**, (1951) 628.

[87] M. Ave et al.,*Proc. of* 30th *ICRC, Mérida*, **astro-ph:0709.2125v1**, (2007).

[88] J. Abraham et al. [Pierre Auger Collaboration], *Nucl. Instrum. Meth.*, **A523** (2004).

[89] R. Cester et al. [Pierre Auger Collaboration], *Proc. of* 27th *ICRC, Hamburg*, 71 (2005).

[90] G. Matthiae, P. Privitera, "Study of the Philips Hexagonal $PMTXP3062$ for the FD Camera", *Pierre Auger Project Technical Note*, **GAP-99-011** (1999).

[91] John A.J. Matthews, *Pierre Auger Tecnical Note*, **GAP-2002-029** (2002).

[92] M. Aglietta et al., *Proc. 29th International Conference on Cosmic Rays Pune (2005).*

[93] D. Veberic and M. Roth, *Auger Note (GAP-2005-035).*

[94] Pierre Auger Collaboration, *Tecnical Design Report*, 2001.

[95] S. Argiro, S.L.C. Barroso, J. Gonzales, L. Nellen, T. Paul, T.A. Porter, L. Prado Jr., M. Roth, R. Ulrich and D. Veberic, Subm. to *Com. Phys. Comm.* (2007)

[96] http://xml.apache.org/xerces-c

[97] http://www.w3.org/XML

[98] http://dev.mysql.com

[99] B. Keilhauer et al., *Proc. of* 29^{th} *ICRC, Pune*, **HE 1.5**, 123 - 127 (2005).

[100] S. BenZvi et al, *The LIDAR system at the Pierre Auger Observaory*, Nucl. Instr. Meth. A574 (2007) 171-184.

[101] R.W. Clay et al., *Pub. Astron. Soc. Aust.*, **15**, 334 (1998).

[102] star monitor aaaa

[103] J.A.J Matthews and M.A. Mostafa, *Proc. 28th International Conference on Cosmic Rays*, vol. 1 pp. 873-876 (2003)

[104] H.M.J. Barbosa et al., Astropart. Phys. 22 (2004) 159-166

[105] J. Hersil et al., *Phys. Rev. Lett.*, **6**, (1961) 22.

[106] B. Dawson et al., *Proc. of* 30^{th} *ICRC, Merida*, arXiv:0706.1105v1 (2007)

[107] F. Arciprete et al, *Nucl.Phys.Proc.Suppl* **150**, 186-189 (2006)

[108] M. Mostafa, *Pierre Auger Tecnical Note*, **GAP-2007-066** (2007)

[109] Bucholtz, A. *Rayleigh scattering calculations for the terrestrial atmosphere*, Appl. Optics, 34, 2765-2773, 1995.

[110] A. Angstrom, Geographical Analysis 12 (1929) 130-159.

[111] S. Y. BenZvi, et al., arXiv:0704.0303 [astro-ph].

[112] E. Andrews, et al., J. Geophys. Res. 111 (D10) (2006) D05S04.

[113] P. Travnicek et al., *Proc. of* 30^{th} *ICRC, Merida, Mexico*, (2007)

[114] M. Jelinek, et al., *Astron. Astrophys.* 454 (2006) L119-L122.

[115] T. F. Eck et al., *J. Geophys. Res.* 104 (1999) 1333 - 31350.

[116] A. Filipcic, M. Horvat, D. Veberic, D. Zavrtanik, M. Zavrtanik, *Astropart. Phys.*, 18 (2003) 501.

[117] M. Unger, R. Engel, F. Schüssler, R. Ulrich: Proc. 30^{th} ICRC (Mérida, México) 2007.

[118] M. Roberts, *Pierre Auger Tecnical Note*, **GAP-2006-067** (2006)

[119] Luis Prado Jr *GAP-NOTE 2003-084*, **FDSim User's Manual Pre-Prod v2r0**.

[120] R. Cester et al. *Proc. of* 29^{th} *ICRC, Pune*, **HE 1.5**, 347 (2005).

[121] J. Bluemer et al. *Proc. of* 28^{th} *ICRC, Tsukuba*, **HE 1.5**, 445 (2003).

[122] M. Mostafà et al. *Proc. of* 28^{th} *ICRC, Tsukuba*, **HE 1.5**, 465 (2003).

[123] F. Arqueros et al. *Proc. of* 29^{th} *ICRC, Pune*, **HE 1.5**, 335 (2005).

[124] M. Ambrosio et al., *Pierre Auger Tecnical Note*, **GAP-2004-065** (2004)

[125] R. Knapik et al. *Proc. of* 30^{th} *ICRC, Mérida*, arXiv:0708.1924v1 (2007)

[126] B. Fick et al., *The Central Laser Facility at the Pierre Auger Observatory*, **JINST** 1 (2006) P11003.

[127] P. Bauleo et al., *Pierre Auger Tecnical Note*, **GAP-2007-064** (2007)